Relativistic Matter Accretion Onto a Class of Black Holes

By

Allah Ditta

PhD Thesis

SESSION 2017-2020

Supervised By

Dr. Ghulam Abbas

DEPARTMENT OF MATHEMATICS
The Islamia University of Bahawalpur
Bahawalpur, Pakistan
2021

Relativistic Matter Accretion Onto a Class of Black Holes

By

Allah Ditta

A dissertation submitted in the partial fulfillment
of the requirements for the degree of
Doctor of Philosophy
in
Mathematics

Supervised By
Dr. Ghulam Abbas

Session 2017-2020
Department of Mathematics
The Islamia University of Bahawalpur
Bahawalpur, Pakistan
2021

Declaration of Originality

I, Allah Ditta son of Malik Allah Diwaya, Ph.D scholar, Department of Mathematics, The Islamia University of Bahawalpur, hereby declare that the research work entitled*"Relativistic Matter Accretion Onto a Class of Black Holes"*is done by me. I also certify that nothing has been incorporated in this research work without acknowledgement and that to the best of my knowledge and belief, it does not contain any material previously published or written by any other person or any material previously submitted for a degree in any university where due reference is made in the text.

Allah Ditta **S/O** Malik Allah Diwaya

Supervisor's Declaration

It is hereby certified that work presented by Allah Ditta in the thesis titled*"Relativistic Matter Accretion Onto a Class of Black Holes"*is based on the results of research study conducted by candidate under my supervision. No portion of this work has been formerly offered for higher degree in this university or any other institute of learning and to the best of the author's knowledge, no material has been used in this thesis which is not his own work, except where due acknowledgement has been made. He has fulfilled for the requirements and is qualified to submit this dissertation in the partial fulfillment for the degree of Doctor of Philosophy in Mathematics in the Faculty of Science, The Islamia University of Bahawalpur.

Dr. Ghulam Abbas
Supervisor
Associate Professor of Mathematics,
The Islamia University of Bahawalpur
Email: `ghulamabbas@iub.edu.pk`
Cell: 03027862183

List of Publications

The results of this thesis are based on the following research articles, which are given below

1. Abbas, G. and **Ditta, A**. (2020) **Matter Accretion onto a Conformal Gravity black hole** *Eur. Phys. J. C* 80:1212.
2. **Ditta, A.** and Abbas, G. (2020) **Circular orbits and accretion process near a regular phantom black hole** *Gen. Relativ. Gravit.* 52:77.
3. **Ditta, A.** and Abbas, G. (2020) **Relativistic accretion mechanism for some black holes** *Chin. J. Phys.* 65:325.
4. Abbas, G. and **Ditta, A**. (2021) **Michel accretion onto a non-commutative black hole** *New Astronomy* 84:101508.
5. **Ditta, A.** and Abbas, G. (2020) **Astrophysical accretion near Hayward regular black holes** *New Astronomy* 81:101437.

Also, the following papers related to this thesis have been published

1. Abbas, G. and **Ditta, A**. (2018) **Accretion onto a charged Kiselev black hole** *Mod. Phys. Lett. A* 33:1850070.
2. Abbas, G. and **Ditta, A**. (2019) **Matter accretion onto Einstein-power-Maxwell black hole** *Gen. Relativ. Gravit.* 51:43.
3. Abbas, G., **Ditta, A**., Jawad, A. and Umair, S. (2019) **Matter accretion onto a brane-world black hole via Hamiltonian approach** *Gen. Relativ. Gravit.* 51:136.
4. Abbas, G. Azam, M. **Ditta, A.** (2021) **Accretion onto a Born-Infeld black hole** *Chin. J. Phys.* 69:143.

Abstract

In this thesis, the matter accretion onto a conformal gravity black hole (BH), regular phantom BH, Einstein-power-Maxwell (EPM) BH, noncommutative BH and Hayward BH is investigated. We have analyzed the general solutions of matter accretion onto these BHs by employing the isothermal equations of state. The Hamiltonian and Michal approaches have been used to study the matter accretion onto these BHs. We have considered the steady state and spherically symmetric accretion of different test fluids, when they fall onto these BHs. Particularly, the flow parameters such as critical velocity $u(r)$, energy density $\varrho(r)$, sonic speed c_s^2 and mass accretion rate $\dot{M}$ have been discussed for these BHs by using the isothermal fluid. We have discussed the physical behavior of family of BHs, when the fluid radial velocity and energy density are positive. The mass accretion rate increases for the cases of dust, stiff fluid and quintessence fluid while it decreases for phantom fluid. Further, we have classified the fluid on the basis of flow as ultra-stiff fluid, ultra-relativistic fluid, radiation-fluid and sub-relativistic fluid by using the Hamiltonian approach. Additionally, the maximum mass accretion rate occurs near the universal and Killing horizons and minimum accretion rate occurs in their annular region. Finally, the results are compared with different cases of BHs available in literature. The physical validity of our results shows that the parameters of the BHs play an important role for the maximum accretion rate.

Acknowledgement

Praise to Almighty ALLAH, The most Beneficent and The most Gracious, to whom I attribute all my success. Peace and countless blessings to the Last Prophet Hazrat MUHAMMAD (Peace Be Upon Him), the only source of knowledge and guidance for the humanity.

I am not finding words to express my gratitude and compliments towards my affectionate supervisor Dr. Ghulam Abbas, due to his devotion, guidance and sincerity made enabled me to complete my research work. No doubt, he possesses true professionalism, broad understanding and wealth of innovative knowledge.

The worthy chairman of the department of mathematics, The Islamia University of Bahawalpur, Prof. Dr. Ghulam Mustafa, richly deserves all the appreciations, admirations and regards for his ideal leadership, devoted support and maintenance of best academic and research atmosphere in the department.

I never forget the encouragement and moral support of my sincere friends at the time of distress and thankful to my respectable colleagues for their cooperation to complete this thesis. Finally, I would like to pay my heartiest gratitude to my family for their **love** and **patience**.

Allah Ditta

Dedication

This thesis is dedicated to my beloved parents, family and my teachers.

Contents

List of Figures

Chapter 1

Introduction

Einstein theory of gravity was suggested in 1915 and is still the standard framework for the account of chrono-geometrical structure and the gravitational fields of the spacetime. Even with its certain success to account for a comprehensive experimental data (Will 2014), the theory is troubled by some major issues that surely identify the entity of present physics. One of these issues is the existence of spacetime singularity in the physically applicable solutions of Einstein field equations. At a singularity, capability of prediction is lost and the new physics breaks down. It has been suggested that the issue of spacetime singularities in the Einstein theory of gravity can be resolved by the quantum gravity theory. Since, the present understanding of physical laws cannot assume a singularity and there are various efforts to solve the singularity issue (Hayward 2006, Fan and Wang 2016, Toshmatov et al. 2014, Mannheim 2012, Bambi et al. 2018, Horava 2009). One of the efforts to solve the singularity issue has been proposed by Bambi et al. (2018), where, singularity free BH solutions have been proposed in conformal theory of gravity.

Latter on, conformal (Weyl) gravity characterized by a pure Weyl squared action has taken a large amount of curiosity as an alternate theory of Einstein gravity. Every conformal class of the Einstein field solutions occur genuinely as a solution of the conformal gravity by the equation of motion and the correspondence of conformal gravity. Mainly, in case of the Neumann boundary condition, conformal gravity can single out Einstein solution was confirmed by Anastasiou and Olea (2016). Further, Mannheim (2011) has investigated that unlike Einstein gravity, conformal gravity is perturbatively renormalizable in four dimensions, on the basis of this aspect conformal gravity is more attractive alternative to quantum gravity (Stelle 1977). The effects of electromagnetic fields around compact stars in conformal gravity have been explored by Turimov et al. (2018). The observational test of conformal gravity has been done by Zhou et al. (2018) using X-ray observations of supermassive BHs. Also, Toshmatov et al. (2017) have discussed explicitly, the energy conditions and scalar perturbations around BHs in conformal gravity. Recently, Haydarov et al. (2020) have studied the motion of magnetized particle around BHs in conformal gravity near the external magnetic fields.

Latest astronomical observations point out that our universe is expanding and its confirmations are supernova type Ia studied by Perlmutter et al. (1999) and the large scale structure (Eisenstein et al. 2002). By current approximations this universe consists of dark matter 22%, dark energy 74% and an ordinary matter 4%. In astronomical observations, there are two main components in our Universe, dark energy and dark matter. Johri (2004) and Lobo (2005) have studied the related work and analyzed that the dark energy produces the gravitational effects and also interrupts the week and null energy conditions. In astrophysics, dark energy is the most inspiring problem and the number of ideas have been suggested to tackle this problem such as phantom energy, scalar fields, quintessence and cosmological constant.

The phantom field is an effective field of our universe and it is natural phenomena to seek its clear appearance in many fields of new physics. In this view, the phantom solutions of regular BH and wormhole with spherical symmetry were found by Bronnikov (2006). The influence of phantom fields continues to attain supports from the observational data (Komatsu et al. 2011, Perlmutter et al. 1999, Blakeslee et al. 2003) and theoretical models (Carroll et al. 2003, Singh 2003). All these observations have pointed out the accelerated expansion of the Universe with an exotic fluid with negative pressure. In this respect, an interest in phantom fields has been developed and resulted in various phantom BH solutions (Gibbons and Rasheed 1996, Gao and Zhang 2009, Clement 2009, Ainou al. 2011). In recent years, various problems pertaining to phantom BHs have been investigated with thermodynamics stability (Rodrigues and Oporto (2012)) and light paths (Azreg-Anou 2013, Gyulchev and Stefanov 2013).

The initiative research of accretion onto compact objects was carried out by Hoyle and Lyttleton (1939). Later on, the study of Hoyle and Lyttleton was extended by Bondi and Hoyle (1944) for a pressureless gas falling onto a compact object. The spherically symmetric accretion onto a gravitating body is the simplest case, which was first studied by Bondi (1952) and is called Bondi accretion. It was shown that the solution describing such a process is unique and flow becomes transonic crossing the critical (sonic) radius. It is currently accepted that Bondi-type of accretion occurs in the Universe because all sources of accreting matter (e.g., gas clouds or stars) have non-zero angular momentum. Michel (1972) derived the general relativistic model of spherically symmetric flow of a test particle onto Schwarzschild BH and then this study has been extended by (Begelman 1978, Thorne et al. 1981 and Pandey 1987) in different papers. Abbas and Ditta (2021) have discussed the Michel accretion near a non-commutative BH. In this work, they have analyzed the critical velocity, speed of sound and the mass accretion rate.

Martnez et al. (2014) and Karkoski et al. (2006) have stated that accretion is the process in which BH attain fluid from its locality. Jamil et al. (2008) have shown that the BH mass does not increase permanently but it could decrease as in the case of accretion of phantom-like matter. In 2020, Ditta and Abbas have studied the accretion mechanism for a class of BHs. They have found that the mass rate must be increases in the stiff-fluid, dust-fluid and quintessence-fluid but it could decrease for phantom fluid. A few initiatives in higher dimensional BHs have been taken by John et al. (2013). From these BHs, it was demonstrated that the matter accretion rate decreases by increasing the dimension of spacetime. Ganguly et al. (2014) have studied the accretion onto string cloud background model. This model shows that the accretion rate increases by increasing the string cloud parameter. Abbas et al.(2020) have discussed the accretion onto Born-Infled BH. They have analyzed that the mass accretion rate increases for the stiff-fluid, dust-fluid and quintessence-fluid but it decreases for phantom fluid.

In modern cosmology, the dark energy is an expressive debate with negative pressure analyzed by Harko and Mak (2005). Both authors Harko and Mak (2005) have observed that the theory of GR faces the huge number of challenges that may need the introduction of the dark matter and dark energy with the ordinary matter. Accretion of dark energy onto Schwarzschild BH was formulated by Babichev et al (2005). Latter on, Debnath (2015) has studied the Babichev idea and proposed a study of spherically symmetrically accretion onto BHs. As spherically symmetrically flows show that the accreting fluid passes through the number of phases, one of them is the presence of an event horizon at which accreting fluid disappears. In this respect, Abbas and Ditta (2019) have analyzed the accretion process for isothermal flow when different test fluids fall onto Einstein-power-Maxwell BH.

Alternative approaches to dark energy are K-essence, phantom and quintessence as studied by Karkoski et al. (2013). Kiselev formulated the Schwarzschild-like solution for quintessence model (2003). Jiao and Yang (2017) have examined the accretion onto a Kiselev BH. Abbas and Ditta (2018) have extended this work to charged Kiselev BH (which is the Reissner-Nordstrom like BH surrounded by quintessence field). They have showed that the results for the Kiselev BH can be recovered by vanishing the charged parameter.

Sharif and his collaborators (2011, 2012, 2016, 2017) have investigated the phantom accretion near a class of BHs. Sharif and Abbas (2011) have studied the phantom energy accretion onto a $5D$ BH and found that CCH is valid for phantom accretion onto a stringy charged BH. The study of circular orbits and accretion disks in a class of Horndeski/Galileon BHs was done by Salahshoor and Nozari (2018). Very recently, Ditta and Abbas (2020) have extended this work for a regular phantom BH. The geodesic study of regular Hayward BH was discussed by Abbas and Sabiullah (2014). Ditta and Abbas (2020) have proposed the astrophysical accretion model near a regular Hayward BH. They have analyzed the properties of accretion such as radial velocity, speed of sound and mass accretion rate.

Furthermore, many other researchers (Karkowski and Malec 2013, Mach et al. 2013, Guzman et al. 2011 and Ananda et al. 2015) have been analyzed the radial flows of perfect fluid and the dark energy onto BHs in modified theories of gravities. The accretion of cyclic and heteroclinic fluid flows near $f(R)$ and $f(T)$ BHs was discussed by Ahmad et al. (2016). Jawad and Shahzad (2017) have discussed the accretion flows near some regular BHs. Using the Hamiltonian approach, the maximum accretion flows with perfect fluids have been explored by Abbas et al. (2019). Further, Abbas and Ditta (2020) have analyzed the accretion process for isothermal flow when different test fluids are falling onto a conformal gravity BH. This thesis has been organized as follows:

- **Chapter two** incorporates some vital concepts and basic terminologies which are related to this thesis.
- **The chapter three** deals with the accretion of test fluids falling onto a BH. Particularly, by adopting a dynamical Hamiltonian approach, we have found the critical points for various cases of BHs in conformal gravity. In these cases, we have analyzed the general solutions of accretion employing the isothermal equations of state. The accretion of different test fluids onto the conformal gravity BH has been considered. The research presented in this chapter has been published in the impact factor journal **European Physical Journal C** (Abbas and Ditta 2020).

- **In chapter four**, we investigate the geodesics motion and accretion process near a regular phantom BH by taking an isothermal fluid with spherically symmetric BH spacetime. The geodesic motion around the BH during accretion provide the disc like structure. The results of this chapter has been published in the impact factor journal **General Relativity and Gravitation** (Ditta and Abbas 2020).

- **Chapter five** includes the general BH spacetime with isotropic fluid for the generalized expressions of the radial velocity $u(r)$, energy density $\varrho(r)$, speed of sound ${c^2}_s$ and mass accretion rate $\dot{M}$. The results of this chapter has been published in the impact factor journal **Chinese Journal of Physics** (Ditta and Abbas 2020).

- **Chapter six** addresses the matter accretion onto a NC inspired Schwarzschild and Hayward BHs for a polytropic fluid and results are compared with Schwarzschild BH. This research work has been published in the impact factor journal **New Astronomy** (Abbas and Ditta 2021, Ditta and Abbas 2020).

- **Chapter Seven** deals with the conclusion of the thesis and some future research directions.

Chapter 2

Basic Concepts

This chapter includes some vital concepts and terminologies which are necessary to understand this thesis.

2.1 General Relativity

Albert Einstein proposed the theory of gravitation in 1915 known as General Relativity (GR). This theory tells that gravitational effects between the masses come from the deformation of objects. In beginning of the 20th century, Newton's law of universal gravitation had been recognized for more than two hundred years as a well description of the gravitational force between masses. The Newton's theory says that gravity is an outcomes of an attractive force between the compact objects.

Observations and experiments represent that Einstein description of gravitation accounts for various effects that are undetermined by Newton law, like anomalies in the orbits of Mercury and some other planets. Einstein GR also predicts the new effects of gravity, such as gravitational lensing, gravitational waves and gravitational time dilation. General Relativity has become an important tool in modern physics. It provides the foundation for the understanding of BHs, the region of spacetime where the gravitational effects are so strong that nothing even light can not escape.

The important predictions of GR are as follows:

- It generalizes the special theory of relativity and Newton law of gravitation in four dimensional spacetime.
- It implies the existence of BHs gravitational waves which have been directly observed.
- Also it implies the existence of gravitational waves which have been directly observed by the physics cooperation.
- In addition, it explains the cosmological models.

In order to study the BH solutions in GR, it is essential to begin with Einstein field equations, which are given by

$$G_{\mu\nu} = R_{\mu\nu} - \frac{1}{2}Rg_{\mu\nu} \equiv \frac{8\pi G}{c^4}T_{\mu\nu}, \tag{2.1}$$

where R is the Ricci scaler, $R_{\mu\nu}$ is the Ricci tensor, $T_{\mu\nu}$ represents the stress energy tensor, which describes the energy density and momentum in a given spacetime, G is Newton gravitational constant and c is the speed of light. For the vacuum, Eq. (2.1) reduces to

$$G_{\mu\nu} = 0. \tag{2.2}$$

Widely accepted as a theory of extraordinary beauty, GR has been described as the most remarkable than the other physical theories.

2.2 The Static Spacetime

As our intention is to research for relativistic stellar objects it seems moderate, on physical grounds, to adopt that spacetime is static and spherically symmetric. It is surely consistent with models applied to investigation physical processes in stellar objects. The general line element for static spherically symmetric spacetimes is given by

$$ds^2 = -A(r)dt^2 + \frac{1}{B(r)}dr^2 + C(r)(d\theta^2 + \sin^2\theta d\phi^2), \tag{2.3}$$

in Schwarzschild coordinates.

2.3 The Spacetime Singularity

The research on BHs in GR (Regge 1961) is done applying a variety of coordinate systems. Several coordinate systems have singularities (point where the spacetime curvature is mathematically ill-defined). Singularities occurs due to an artefact of the coordinates system being used. One of the old and most important coordinates system that was used to study BH was the Schwarzschild coordinates system specified earlier. This system is authentic in a vacuum region surrounding a spherically symmetric distribution of mass and can be obtained from the Einstein field equations (Carroll 2013).

2.4 The Black Holes

The existence of BHs is one of the most surprising phenomena in our Universe. Black hole is an object of a classical theory. The Einstein theory of gravity which defines the coupling of matter and geometry of spacetime. Here, one natural question to ask is how does the Einstein's theory of gravity describe spacetime around a massive object like a star? Schwarzschild found the answer of this question and it is valid for all static round objects which only depends on its mass. However, the strange things can happen, when all the mass is closed within a particular radius named as Schwarzschild radius. Then an event horizon forms at the Schwarzschild radius. The BH is defined as

The place in spacetime where gravitational pull is so powerful that even light cannot escape from it, is called BH, which is formed when a massive star endures to gravitational collapse. Due to dense state of matter, it is steady and external sources can not destroyed it. Only these sources may cause to change its mass, charge and angular momentum. A BH can be characterized by only three quantities:

- Mass (when it has no electric charge and no angular momentum, it is called Schwarzschild BH).

- Electric Charge (charged BH is called the Reissner-Nordstrom BH).
- Angular Momentum (when it has no charge then it is called the Kerr BH and a BH with charge and angular momentum is Kerr Newman BH).

There are different types of BHs, depending on their mass.

2.4.1 Conformal Gravity Black Hole

The general action of conformal theory can be developed on the basis of following four points:

- It is a completely covariant advancement theory of GR.
- It is an additional symmetry principle or local conformal invariance and the existence of the symmetry principle prevents the Einstein Hilbert action and cosmological term in the action.
- The conformal transformation of the theory is $g_{\mu\nu} \rightarrow \Omega^2(x) g_{\mu\nu}$.
- The conformal gravity action is defined in terms of Weyl tensor $C_{\eta\lambda\mu\nu}$ and a coupling constant α_g, which is a dimensionless constant and this allows the conformal gravity theory is a quantum theory of gravity. The action of conformal gravity contributes to fourth order of equation of motion. The fourth order equations of motion involve more constants of integration and also solutions contain more parameters.

The action and the field equations are given by

$$\begin{aligned} S_{CG} &= -\alpha_g \int d^4x (-g)^{1/2} C_{\eta\lambda\mu\nu} C^{\eta\lambda\mu\nu}, && (2.4) \\ C_{\eta\lambda\mu\nu} &= R_{\eta\lambda\mu\nu} - \frac{1}{2}(g_{\eta\mu}R_{\lambda\nu} - g_{\eta\nu}R_{\lambda\mu} + g_{\lambda\nu}R_{\eta\mu} - g_{\lambda\mu}R_{\eta\nu}) && (2.5) \\ &\quad + \frac{R}{6}(g_{\eta\mu}g_{\lambda\nu} - g_{\eta\nu}g_{\lambda\mu}), \end{aligned}$$

The following gravitational field equations are achieved by varying the action (2.4) with respect to $W_{\mu\nu}$ and the energy momentum tensor $T_{\mu\nu}$, which are

$$\begin{aligned} 2\alpha_g W_{\mu\nu} = & \frac{1}{2}T_{\mu\nu}. && (2.6)\\ W_{\mu\nu} = & \frac{1}{3}\nabla_\mu\nabla_\nu R - \nabla_\lambda\nabla^\lambda R_{\mu\nu} + \frac{1}{6}(R^2 + \nabla_\lambda\nabla^\lambda R && (2.7)\\ & -3R_{\eta\lambda}R^{\eta\lambda})g_{\mu\nu} + 2R^{\eta\lambda}R_{\mu\eta\nu\lambda} - \frac{2}{3}RR_{\mu\nu}. \end{aligned}$$

Therefore, the exact vacuum solution is given by the metric (2.3) with

$$\begin{aligned} A(r) &= B(r) = 1 - \frac{\beta(2-3\beta\gamma)}{r} - 3\beta\gamma + \gamma r - kr^2,\\ C(r) &= r^2, \end{aligned} \tag{2.8}$$

where β, γ and k are constants of integration.

2.4.2 The Phantom Black Hole

The phantom solutions of regular BH and wormhole with spherical symmetry were found by Bronnikov and Fabris (2006). There is no singularity inside the event horizon of a phantom BH as compared to the instance of regular BHs with nonlinear electrodynamics sources as discussed by Flachi and Lemos (2013). The properties of a phantom BH are alike to those of a Schwarzschild BH in case of outside the event horizon. Phantom regular BH solution has attracted much attention of the researchers because of absence of the singularity.

The widely accepted and consistent alternative to the GR is the scalar-tensor gravity proposed by Babichev et al. (2016). The action of this theory was proposed by Bronnikov and Fabris (2006), as

$$S = \int \sqrt{-g}d^4x \left[R - \frac{1}{2}g^{\mu\nu}\partial_\mu\phi\partial_\nu\phi + V\right], \tag{2.9}$$

where R is a scalar curvature and $\phi = \sqrt{2}\psi = \sqrt{2}\arctan\frac{r}{b}$, $V = \frac{3M}{b^3}[(\frac{\pi}{2} - \psi)(3 - 2\cos^2\psi) - 3\sin\psi\cos\psi]$.

Therefore, the exact vacuum solution is given by the metric (2.3) with

$$\begin{aligned} A(r) &= B(r) = 1-\frac{3M}{b}\left[\Big(\frac{\pi}{2}-\arctan\frac{r}{b}\Big)\left(1+\frac{r^2}{b^2}\right)-\frac{r}{b}\right], \\ C(r) &= r^2+b^2, \end{aligned} \tag{2.10}$$

where, b is the scalar charge of phantom field which is positive constant, also called phantom hair and the mass of BH is denoted by M. The theory of scalar-tensor gravity plays a dominant role at astrophysical scale and also deals with static and the spherically symmetric solutions.

2.4.3 Einstein Power-Maxwell $3D$ Black Hole

The authors Hassaine and Martinez (2008) have studied the higher-dimensional BHs with a conformally invariant Maxwell source. They proposed the action for an abelian gauge field for which the density is given by the power of the Maxwell Lagrangian. The action with non-vanishing cosmological constant for the Einstein power-Maxwell (EPM) theory of gravity in $3D$, is given by (Gurtug, et al. (2012))

$$S=\int dx^3\sqrt{-g}\Big(\frac{1}{16\pi}(R-\frac{2}{3}\Lambda)-b_kF^k\Big), \tag{2.11}$$

where $b_k=(-1)^{1-k}$ is coupling constant. Hassaine and Martinez (2008) have taken $b_k=\alpha$, where α is an arbitrary constant for nonlinear electromagnetic field in which k is an arbitrary rational number and $F=F_{\mu\nu}F^{\mu\nu}$ is the Maxwell invariant. The EPM BH solution is given by the metric (2.3) with

$$\begin{aligned} A(r) &= B(r) = -M+\frac{r^2}{l^2}+\frac{4\pi Q^{\frac{4}{3}}}{3r^2}, \quad l^2=\frac{-1}{\Lambda}>0,\ \Lambda<0, \\ C(r) &= r^2, \end{aligned} \tag{2.12}$$

where M is gravitational mass, Q is charge and Λ is the cosmological constant.

2.4.4 Einstein Power-Maxwell $4D$ Black Hole

The EPM $4D$ BH was proposed by Hassaine and Martinez (2008). They proved that in d dimensions the action (2.11), obeys the conformal invariance if the power is chosen as $d/4$. Therefore EPM $4D$ BH action is given by

$$S = \int dx^4 \sqrt{-g}\Big(\frac{1}{16\pi}(R - \frac{2}{3}\Lambda) - b_k F^k\Big), \tag{2.13}$$

using the action, one can find the EPM $4D$ BH solution, given by the metric (2.3) with

$$\begin{aligned} A(r) &= B(r) = 1 - \frac{\mu}{r} + \frac{q}{r^3}, \\ C(r) &= r^2, \end{aligned} \tag{2.14}$$

here, the metric parameters μ and q represent the mass and an electric charge of the metric functions, respectively.

2.4.5 The Hayward Black Hole

It is well known that the singularity at the center in BHs designates collapse of GR. Since a regular black hole (RBH) solution is obtained from the gravitational field equations without a singularity inside the event horizon of BH. Therefore, it is probable to create BHs, which are regular and do not have a singularity at the center. It has been believed that this singularity can be disconnected in quantum theory of gravity. However, a BH without singularity was first considered by Bardeen (1968) known as regular BH (nonsingular). The Hayward BH (Hayward, 2006) is kind of such a regular BH, which do not have a singularity at the center (Halilsoy et al. 2014). Ayn-Beato and Garca (2000) verified that the Bardeen BH ia an exact solution in a spacetime with nonlinear electrodynamics. Therefore, the action of nonlinear electrodynamics in curve spacetime is given by

$$S = \int dx^4 \sqrt{-g}\Big(\frac{1}{16\pi}(R - \mathtt{L}(F))\Big), \tag{2.15}$$

where R is the scalar curvature, and the $\mathtt{L}$ depends on the $F = F_{\mu\nu}F^{\mu\nu}/4$. The Hayward regular BH is by the metric (2.3) with

$$
\begin{aligned}
A(r) &= B(r) = 1 - \frac{2mr^2}{r^3 + 2l^2 m}, \\
C(r) &= r^2.
\end{aligned} \tag{2.16}
$$

2.4.6 The Non-Commutative Black Hole

Noncommutative background is much important in the specific framework of BH thermodynamics. Haldar et al. (2018) have studied the Generalized Uncertainty Principle (GUP) correction of non-thermal radiation spectrum in the background of NC geometry using the framework of tunneling mechanism. Banerjee and Majhi, (2009) have discussed the area law and quantum tunneling for the NC BHs. It has been extensively approved that quantum gravity essential involve an uncertainty principle which intercepts the area lower than the Planck scale (Snyder, 1947).

The NC geometry is very effective area of research due to its direct significance in Planck scale physics (Connes, 1994). Besides, the NC geometry has no curvature singularity. Here, we infer to use the spherically symmetric mass distribution (Nicolini et al., 2006) with Gaussian distribution with minimal width $\sqrt{\theta}$, so we have

$$
\varrho_\theta(r) = \frac{M e^{-r^2/4\theta}}{(4\pi\theta)^{3/2}}. \tag{2.17}
$$

The NC formulation of GR, can be done by replacing Dirac delta function by the specially growing distribution of the mass density $\varrho_\theta(r)$ (Nicolini et al., 2006).

Therefore, the exact vacuum solution is given by the metric (2.3)

$$
\begin{aligned}
A(r) &= B(r) = 1 - \frac{m(r)}{r}, \\
C(r) &= r^2, \\
m(r) &= \frac{2M}{\sqrt{\pi}} \gamma(3/2, r_H^2/4\theta),
\end{aligned} \tag{2.18}
$$

where $\gamma(3/2, r^2/4\theta)$, is the lower incomplete gamma function defined by

$$
\gamma(3/2, r^2/4\theta) = \int_0^x p^{3/2-1} e^{-p} dp. \tag{2.19}
$$

2.5 The Event Horizon

The BH region in a spacetime is a boundary from which no light ray can escape (Hawking 1972). This boundary is called an event horizon. In other words, the boundary of a region in spacetime that cannot be observed by a far away observer is called event horizon. According to Hawking and Ellis (1979), event horizon is a null surface, which can completely describe the causal structure of spacetime. In case of Schwarzschild BH, event horizon is at $r = 2m$.

2.6 Accretion Process

A very latest image of a BH established by the Event Horizon Telescope proves that the accretion onto BHs is a significant issue in today science as observed by Akiyama et al. (2019). Accretion is the process by which massive astronomical objects apprehend the surroundings matter given in the interstellar medium that shows an increase in mass (Martnez (2014)). In astrophysics, accretion process is one of the global processes, in which fluid fall onto massive objects, it is feasible cause for the formation of active galactic nuclei, quasar and energy of X-rays. During accretion, the kinetic energy of falling matter raises on the entity of gravitational energy. Accretion is important because

- It is the way for the objects to grow.
- It is the way for gravitational energy to be released.

2.6.1 The Energy-Momentum Tensor

The energy-momentum tensor is the agent of gravitational field like mass density. $T^{\mu\nu}$ is flow of the μ component of the four-momentum parallel to the ν direction. The energy-momentum tensor for the arbitrary manifold is defined by

$$T^{\mu\nu} = \varrho u^{\mu} u^{\nu} + \xi^{\alpha\beta} \delta^{\mu}_{\alpha} \delta^{\nu}_{\beta} \tag{2.20}$$

where ϱ is energy density, u^{μ} is four velocity and $\xi^{\alpha\beta}$ is shear tensor. It is a symmetric tensor of second rank, i.e., $T^{\mu\nu} = T^{\nu\mu}$. The components of energy momentum have the following key points:

- T^{00} represents energy density of matter.
- $T^{0\omega}$ is the flow of energy per unit area along ω direction.
- $T^{\omega\omega}$ is the flow of ω component of momentum in the ω direction.
- $T^{\omega l}$ is the flow of ω component of momentum in the l direction.
- $T^{\omega 0}$ represents the density of ω component of momentum.

The value of energy-momentum tensor is zero for vacuum.

2.6.2 Perfect Fluid Energy-Momentum Tensor

Perfect fluid is a medium in which heat transport and shear stresses are not present and pressure remains isotropic in the rest-frame for each fluid element. The energy momentum tensor for such fluid is given by

$$T^{\mu\nu} = (\varrho + p)u^{\mu}u^{\eta} + pg^{\mu\nu}, \tag{2.21}$$

For pressure equal to zero, above equation becomes

$$T^{\mu\nu} = \varrho u^{\mu}u^{\nu}. \tag{2.22}$$

which is the energy-momentum for dust fluid

2.7 General Formalism of Spherical Accretion

We study the curved spacetime corresponding to a general static and spherically symmetric object which is given by the metric (2.3), where all the coefficients $A(r) > 0$, $B(r) > 0$, $C(r) > 0$ are the functions of radial distance r. Debnath (2015) used this spacetime with $C(r) = r^2$. Now, we are going to extend this procedure for general formulism of accretion process. We define the four-velocity in the following form

$$u^\mu = \frac{dx^\mu}{d\tau} = (u^t, u^r, 0, 0), \tag{2.23}$$

where τ is the proper time. The four velocity must satisfying the normalization condition $u^\mu u_\mu = -1$, this gives

$$u^t = \sqrt{\frac{A(r) + (u^r)^2}{B(r)A(r)}}. \tag{2.24}$$

For inward flow or accretion, the velocity of flow must be negative, so $u^r < 0$. The following conservation laws are necessary for the accretion process. The energy conservation is derived as follows

$$T^{\mu\nu}_{;\mu} = 0 \Rightarrow T^{\mu\nu}_{;\mu} = \frac{1}{\sqrt{-g}}(\sqrt{-g}T^{\mu\nu})_{,\mu} + \Gamma^\nu_{\alpha\mu}T^{\alpha\mu} = 0, \tag{2.25}$$

which simplifies to

$$u^r C(r)(\varrho + p)\frac{A(r)}{B(r)}\sqrt{A(r) + (u^r)^2} = N_0, \tag{2.26}$$

where N_0 is an integration constant. The relation between energy conservation and four velocity $u_\mu T^{\mu\nu}_{;\nu} = 0$, leads to

$$(\varrho + p)_{;\nu}u_\mu u^\mu u^\nu + (\varrho + p)u^\mu_{;\nu}u_\mu u^\nu + (\varrho + p)u_\mu u^\mu u^\nu_{;\nu} + p_{,\nu}g^{\mu\nu}u_\mu + pu_\mu g^{\mu\nu}_{;\nu} = 0. \tag{2.27}$$

Using $u^\mu u_\mu = -1$ and $g^{\mu\nu}_{;\nu} = 0$, the above relation reduces to

$$(\varrho + p)u^\nu_{;\nu} + u^\nu \varrho_\nu = 0. \tag{2.28}$$

After the manipulations of non-zero components, we get

$$\frac{\varrho'}{\varrho + p} + \frac{u'}{u} + \frac{A'}{2A} + \frac{B'}{2B} + \frac{C'}{C} = 0, \tag{2.29}$$

after integrating the above equation, we get

$$u^r C(r)\sqrt{\frac{A(r)}{B(r)}}\exp\int\frac{d\varrho}{\varrho + p} = -N_1, \tag{2.30}$$

where N_1 is the integration constant. As $u^r < 0$, the minus sign should be in the right hand side. Now, we combine the Eqs. (2.26) and (2.30), to get

$$(\varrho + p)\sqrt{(u^r)^2 + B(r)}\sqrt{\frac{A(r)}{B(r)}}\exp\left(-\int\frac{d\varrho}{\varrho + p}\right) = N_2, \tag{2.31}$$

where N_2 represents the integration constant. The mass flux is given by

$$(\varrho u^\mu)_{;\mu} \equiv \frac{1}{\sqrt{-g}}(\sqrt{-g}\varrho u^\mu)_{,\mu} = 0. \tag{2.32}$$

The above equation simplifies to

$$\sqrt{\frac{A(r)}{B(r)}}C(r)\varrho u^r = N_3, \tag{2.33}$$

where N_3 is the integration constant. Combining Eqs. (2.26) and (2.33), we get

$$\left(\frac{\varrho + p}{\varrho}\right)\sqrt{(u^r)^2 + B(r)}\sqrt{\frac{A(r)}{B(r)}} = N_4, \tag{2.34}$$

where N_4 represents another arbitrary constant. Now differentiation of Eqs. (2.33) and (2.34), lead to

$$\left(V^2 - \frac{u^2}{u^2 + B}\right)\frac{du}{u} + \left((V^2 - 1)\left(\frac{A'}{A} - \frac{B'}{B}\right) + \frac{C'}{C}V^2 - \frac{B'}{2(u^2 + B)}\right)dr = 0. \tag{2.35}$$

Now we define

$$V^2 = \frac{dln(p + \varrho)}{dln\varrho} - 1. \tag{2.36}$$

For the critical accretion the radial distance will be $r = r_c$, Eq. (2.35) can be written into two parts and both must would be equal to zero. Hence, we get

$$\begin{aligned} V_c^2 &= \frac{u_c^2}{u_c^2 + B(r_c)}, && (2.37)\\ (V_c^2 - 1)\left(\frac{A'(r_c)}{A(r_c)} - \frac{B'(r_c)}{B(r_c)}\right) + \frac{C'(r_c)}{C(r_c)}V_c^2 &= \frac{B'(r_c)}{2(u_c^2 + B(r_c))}. && (2.38)\end{aligned}$$

Here u_c is the critical velocity of the flow, we decouple the variables u_c^2, V_c^2 and get

$$\begin{aligned} u_c^2 &= \frac{B(r)A'(r)C(r)}{2A(r)C'(r)}, && (2.39)\\ V_c^2 &= \frac{C(r)A'(r)}{C(r)A'(r) + 2A(r)C'(r)}. && (2.40)\end{aligned}$$

The sound speed is obtained from the relation (2.34), which is given by

$$c_s^2 = \frac{dp}{d\varrho}|_{r=r_c} = N_4\sqrt{\frac{B(r_c)}{A(r_c)(u_c^2 + B(r_c))}} - 1. \tag{2.41}$$

For the result of u_c^2 and V_c^2, we have

$$\frac{A'(r)}{C'(r)} > 0. \tag{2.42}$$

Using this relation, one can get the dimensionless critical radius in the proposed metric.

2.8 Equation of State

Equation of state (EoS) is helpful in describing the properties of fluid, solids and interior of stars. The EoS for perfect fluid is $p = \omega\varrho$, where ω is the state parameter with $\omega = -1$, a cosmological constant, $-1 < \omega < -1/3$, for quintessence and $\omega < -1$, for phantom models (Nojiri and Odintsov (2011)). The following fluids are characterized from the equation of state:

- If $\omega = 1$, the stiff fluid.
- If $\omega = 1/2$, the relativistic fluid.
- If $\omega = 1/3$, the radiation fluid.
- If $\omega = 1/4$, the sub-relativistic fluid.

2.9 Hamiltonian Approach

Since, at the constant pressure, the enthalpy is the ratio of density of fluid and the total energy of the system. So, in fluid dynamics, we may define the enthalpy as $h(\varrho, p, n) = \frac{\varrho+p}{n}$. By this definition, we rewrite the fundamental Eqs. (2.33) and

(2.34) as

$$\begin{aligned} r^2 nu &= N_3, && (2.43) \\ h\sqrt{A(r)+(u)^2} &= N_4, && (2.44) \end{aligned}$$

Now, we derive the dynamical Hamiltonian system by adopting these fundamental equations. We take H be the square of the L.H.S. of Eq. (2.44), so

$$H = h^2\Big(A(r)+(u)^2\Big), \tag{2.45}$$

also, we can write

$$H = h^2\Big(A(r)+(u)^2\Big), \tag{2.46}$$

where $v \equiv \frac{dr}{A(r)dt}$, is three-dimensional speed with radial motion of a particle in equatorial plan. Thus, we have

$$v^2 = \left(\frac{u}{A(r)u^0}\right)^2 = \frac{u^2}{u_0^2} = \frac{u^2}{A(r)+u^2}, \tag{2.47}$$

which simplifies to

$$u^2 = \frac{A(r)v^2}{1-v^2}. \tag{2.48}$$

Using Eq. (2.48) into Eq. (2.46), we get

$$H = \frac{h^2 A(r)}{1-v^2}. \tag{2.49}$$

From Eqs. (2.43) and (2.48), we get

$$N_3^2 = \frac{r^4 n^2 A(r) v^2}{1-v^2} \tag{2.50}$$

As from the sonic points and isothermal test fluids, we have $v_c^2 = a_c^2$ and $r_c(1-v_c^2)A'(r) = 4A(r)_c a_c^2$. If we write Eq. (2.50) as

$$N_3^2 = \frac{r_c^4 n_c^2 A(r)_c v_c^2}{1-v_c^2}, \tag{2.51}$$

which simplifies to

$$N_3^2 = \frac{r_c^5 n_c^2 A'(r)_c}{4}. \tag{2.52}$$

Using Eq. (2.50) and Eq. (2.52), we get

$$\frac{r^4 n^2 A(r) v^2}{1-v^2} = \frac{r_c^5 n_c^2 A'(r)_c}{4}, \tag{2.53}$$

which simplifies to

$$\Big(\frac{n}{n_c}\Big)^2 = \frac{r_c^5 A'(r)_c}{4} \frac{1-v^2}{r^4 A(r) v^2}. \tag{2.54}$$

Now, using enthalpy $\frac{\varrho+p}{n} = h$, equation of state $p = \omega\varrho$ and by second fundamental equation, we have

$$h = \frac{(\omega+1)\varrho_c}{n_c}\left(\frac{n}{n_c}\right)^{\omega}, \tag{2.55}$$

using (2.54) and (2.55), we have

$$h^2 = \Big(\frac{(\omega+1)\varrho_c}{n_c}\Big)^2 \Big(\frac{r_c^5 A'(r)}{4}\Big)^{\omega} \Big(\frac{1-v^2}{r^4 A(r) v^2}\Big)^{\omega}, \tag{2.56}$$

which simplifies to

$$h^2 \propto \Big(\frac{1-v^2}{r^4 A(r) v^2}\Big)^{\omega}. \tag{2.57}$$

Finally, using above relation in Eq. (2.46), we obtain

$$H = \frac{A^{1-\omega}}{(1-v^2)^{1-\omega} v^{2\omega} r^{4\omega}}. \tag{2.58}$$

2.9.1 Sonic points

Sonic point (critical point) is a point, where the velocity of the moving gas must be equal to the local sound speed. By this definition, the maximum accretion rate occurs, if the flow passes through the critical point. Our aim is to calculate the critical points of the flow and the sound speed at these points, for this, we assume the barotropic fluid at constant enthalpy that is $h = h(n)$. Therefore, the equation of state for this flow becomes (Ficek, 2015),

$$\frac{dh}{h} = a^2 \frac{dn}{n}, \tag{2.59}$$

where a represents the local sound speed. Also, from above equation we get $\ln h = a^2 \ln n$. Using (2.24), (2.34) and (2.59), we acquire

$$\left[\left(\frac{u}{u_0}\right)^2 - a^2\right](\ln u)_{,r} = \frac{1}{r(u_0)^2}\left[2a^2(u_0)^2 - \frac{1}{2}rA'(r)\right]. \tag{2.60}$$

Now, for critical points, both sides of above relation (2.60) should be equal to zero. So, the sound speed at the critical point becomes

$$a_c^2 = \left(\frac{u_c}{u_{0c}}\right)^2, \tag{2.61}$$

where the quantities, a_c , r_c and u_c designate the sound speed, distance and velocity of the fluid from the BH at the critical point, respectively. Therefore, another result of Eq. (2.60) at critical point is given by

$$2a_c^2(u_{0c})^2 - \frac{1}{2}r_cA'_{r_c} = 0. \tag{2.62}$$

From Eqs. (2.61) and (2.62), one can get the radial velocity at the critical points, which is given by

$$(u_c)^2 = \frac{1}{4}r_cA'_{r_c}. \tag{2.63}$$

Using Eqs. (2.25), (2.62) and (2.63), we obtain

$$r_cA'_{r_c} = 4a_c^2[A(r_c) + (u_c)^2]. \tag{2.64}$$

Thus, we have

$$a_c^2 = \frac{r_cA'_{rc}}{r_cA'_{r_c} + 4A(r_c)}. \tag{2.65}$$

Therefore, someone can obtain the critical points as $(r_c, \pm u_c)$ using Eqs. (2.63) and (2.65), if one has the value of sound speed.

2.9.2 Isothermal Test Fluids

After combining $p = \omega\varrho$ with $a^2 = \frac{dp}{d\varrho}$, consequently, $a^2 = \omega$ is obtained. Applying the first law of thermodynamics, we get

$$\frac{d\varrho}{dn} = \frac{\varrho + p}{n} = h. \tag{2.66}$$

Integrating the above Eq. (2.66) from the critical point to any point inside fluid, we get

$$n = n_c \exp\left(\int_{\varrho_c}^{\varrho} \frac{d\varrho'}{\varrho' + p(\varrho')}\right). \tag{2.67}$$

With the help of $p = \omega\varrho$, the above Eq. (2.67) gives

$$n = n_c \left(\frac{\varrho}{\varrho_c}\right)^{\frac{1}{\omega+1}}. \tag{2.68}$$

Using $h(\varrho, p, n) = \frac{\varrho+p}{n}$ and the above relation, we obtain

$$h = \frac{(\omega+1)\varrho_c}{n_c}\left(\frac{n}{n_c}\right)^{\omega}. \tag{2.69}$$

By using Eq. (2.63) and (2.64), we get

$$(u_c)^2 = \frac{1}{4} r_c A'_c, \tag{2.70}$$

$$(u_c)^2 = \omega\left(\frac{1}{4} r_c A'_c + A_c\right). \tag{2.71}$$

Consequently, for the classification of fluid flow, the generalized expression (2.71) can be solved numerically by choosing the any value of ω. In rest of the work, we assume the four kinds of fluid such as, ultra-stiff fluid, ultra-relativistic fluid, radiation fluid and sub-relativistic fluid for the accretion onto a class of BHs.

2.9.3 Polytropic Test Fluids

A mathematical form of *polytropic equation of state* is (Ahmad, et al. (2016))

$$p = G(n) = \Gamma n^{\alpha}, \tag{2.72}$$

here α and Γ are constant parameters. One can consider the general constraint α is greater than 1 for any fluid. Specific enthalpy is given by (Jawad and Shahzad (2017))

$$h = m + \frac{\Gamma\alpha n^{\alpha-1}}{\alpha-1}. \tag{2.73}$$

Three dimensional sound speed is

$$a^2 = \frac{(\alpha-1)U}{m(\alpha-1)+U}, \tag{2.74}$$

where $U = \gamma \alpha n^{\alpha-1}$. Another useful result can be obtain with the help of speed of sound, which is given by

$$h = m\frac{\alpha - 1}{\alpha - 1 - a^2}, \tag{2.75}$$

and therefore

$$h = m\left(1 + X\left(\frac{1 - v^2}{r^4 A(r) v^2}\right)^{(\alpha-1)/2}\right), \tag{2.76}$$

where

$$X = \frac{\Gamma \alpha n_c^{\alpha-1}}{m(\alpha - 1)}\left(\frac{r_c^5 A'(r_c)}{4}\right)^{(\frac{\alpha-1}{2})} = constant > 0. \tag{2.77}$$

From the above result, it is clear that the constant X depends on the BH parameters and also on the test fluids. The final form of the Hamiltonian system can be obtained by using Eqs. (2.76) and (2.58), which is given by

$$H = \frac{A(r)}{1 - v^2}\left(1 + X\left(\frac{1 - v^2}{r^4 A(r) v^2}\right)^{(\alpha-1)/2}\right)^2. \tag{2.78}$$

2.10 Radial Velocity

The radial velocity of an object with respect to a given point is the rate of change of the distance between the object and the point. In other words the radial velocity is the component of the object's velocity that points in the direction of the radius connecting the point and the object.

In case of fluid flow, radial velocity depends on EoS of the fluid. Fluid has zero radial velocity for asymptotic limit, however, these acquire non-vanishing velocities as they approach to naked singularity. Due to strong gravitational attraction near the naked singularity, the fluids achieve critical velocities, we observe some symmetry in the profile of the velocity curves and the location of critical points. After passing through critical point, the fluid flow becomes supersonic or transsonic. From Eq. (2.34), we have

$$u(r) = \left(\frac{1}{k+1}\right)\sqrt{\frac{(N_4)^2}{A(r)} - (k+1)^2}. \tag{2.79}$$

2.11 Mass Accretion Rate

Mass accretion rate is the area times flux on the boundary of BH, it is denoted by $\dot{M}$. The general formula for accretion rate of fluid around the BH is given by (Biswas 2011),

$$\dot{M}_{acc} = 4\pi AM^2(\rho + p), \tag{2.80}$$

where dot represents the derivative with respect to time. We see that the mass of the BH will increase for any fluid such as $\rho + p > 0$, which accretes outside the BH. On the other hand, if the fluid is phantom dark energy $\rho + p < 0$, then the mass of the BH will decrease.

From the energy momentum tensor of perfect fluid, we have $T_t^r = (\varrho + p)u_t u^r$. Since, the dynamical system is conserved, so we have $\nabla_\mu J^\mu = 0$ and $\nabla_\nu T^{\mu\nu} = 0$. Thus due to this conserved system, Eqs. (2.33) and (2.34) give the following result (by consideration $A(r) = B(r)$ and $C(r) = r^2$,

$$r^2 u(\varrho + p)\sqrt{A(r) + (u)^2} = L_0, \tag{2.81}$$

where L_0 denotes an arbitrary constant. Now, using the continuity equation (relativistic energy flux) and the equation of state $p = p(\varrho)$, we get

$$\frac{d\varrho}{\varrho + p} + \frac{du}{u} + \frac{2}{r}dr = 0. \tag{2.82}$$

After integrating, we obtain

$$r^2 u \exp\left[\int_{\varrho\infty}^{\varrho} \frac{d\varrho'}{\varrho' + p(\varrho')}\right] = -L_1, \tag{2.83}$$

where L_1 is constant of integration and ϱ_∞ represents fluid density at infinity. In the R. H. S. of above equation, the minus is taken due to $u < 0$. Dividing Eq. (2.83) with (2.81), we get

$$L_3 = -\frac{L_0}{L_1} = (\varrho + p)\sqrt{A(r) + (u)^2}\exp\left[-\int_{\varrho\infty}^{\varrho} \frac{d\varrho'}{\varrho' + p(\varrho')}\right], \tag{2.84}$$

where L_3 is constant. At infinity, $L_3 = \varrho_\infty + p(\varrho_\infty) = -\frac{L_0}{L_1}$, with $L_0 = (\varrho + p)u^0 u r^2 = -L_1(\varrho_\infty + p(\varrho_\infty))$. The problem is spherically symmetrically static at equatorial plane. So, the mass flux equation $\nabla_\mu J^\mu = 0$ is given by

$$r^2 u n = L_2, \tag{2.85}$$

where L_2 represents the integration constant. Dividing the Eqs. (2.81) and (2.85), we get

$$\frac{\varrho + p}{n}\sqrt{A(r) + (u)^2} = \frac{L_0}{L_2} \equiv L_4, \tag{2.86}$$

where L_4 is any constant, which is $L_4 = \frac{(\varrho_\infty + p_\infty)}{n_\infty}$. Putting Eq. (2.81) in the expression.

$$\dot{M} = -4\pi r^2 u(\varrho + p)\sqrt{A(r) + (u)^2} = -4\pi L_0. \tag{2.87}$$

Then, it becomes

$$\dot{M} = 4\pi L_1(\varrho_\infty + p(\varrho_\infty)). \tag{2.88}$$

Thus the Eq. (2.88) gives the valid result for any nature of fluids. Thus, we have

$$\dot{M} = 4\pi L_1(\varrho + p)|_{r=r_h}, \tag{2.89}$$

assuming the isothermal EoS $p = \omega\varrho$, and $(\varrho + p) = \varrho(1 + \omega)$. Then, using the Eq. (2.83), it leads us to

$$\varrho = \left[-\frac{L_1}{r^2 u}\right]^{1+\omega}. \tag{2.90}$$

By the expression of ϱ, one can obtain the following general equation from (2.81), which is given by

$$(u)^2 - \frac{L_0^2 L_1^{-2(1+\omega)}}{(1+\omega)^2} r^{4\omega}(-u)^{2\omega} + A(r) = 0. \tag{2.91}$$

It can be solved for fluid velocity u with any value of ω. One can calculate the energy density ϱ by using u for any values of ω. By assuming $\omega = 1$ in Eq. (2.91), one can calculate the radial velocity and the energy-density of the ultra-stiff fluids, that is

$$u = \pm L_1^2 \sqrt{\frac{A(r)}{L_0^2 r^4 - 4L_1^4}}, \tag{2.92}$$

also the energy density is given by

$$\varrho=\frac{(L_0^2r^4-4L_1^4)}{4L_1^2r^4A(r)}. \tag{2.93}$$

Consequently, using Eq. (2.93) into Eq. (2.89), the mass accretion rate of BH takes the following form

$$\dot{M}=\frac{2\pi(L_0^2r^4-4L_1^4)}{L_1r^3A(r)}. \tag{2.94}$$

The above Eq. (2.94) is the general expression of mass accretion rate for any BH.

Chapter 3

Matter Accretion onto a Conformal Gravity Black Hole

The aim of this chapter is to investigate the accretion of test fluids flowing onto a BH. Particularly, by adopting a dynamical Hamiltonian approach, we are capable to find the critical points for various cases of BH in conformal gravity. In these cases, we have analyzed the general solutions of accretion employing the isothermal equations of state. Further, we have classified these flows in the context of equations of state and the cases of conformal gravity BH. The new behavior of polytropic fluid accretion is also discussed in all three cases of BH. Black hole mass accretion rate is the most important part of this research in which we have investigated that the Schwarzschild BH produce a typical signature than the conformal gravity BH and Schwarzschild de-Sitter BH. The critical fluid flow and the mass accretion rate have been presented graphically by the impact parameters β, γ, k and these parameters have great significance. Additionally, the maximum mass rate of accretion fall near the universal and Killing horizons and minimum rate of accretion occurs in between these regions. Finally, the results are compared with the different cases of BH available in the literature. The outcomes of this chapter have been published in the form of a research article (Abbas and Ditta 2020).

The detail of this chapter is as follows: The conformal gravity BH solution with different values of parameters has been presented in section **3.1**. In section **3.2**, we have formulated the horizon structure of conformal gravity BH. Section **3.3** is dedicated to spherical accretion onto conformal gravity BH. The sound speed at the critical points is formulated in section **3.4**. Further, in the subsequent sections, we have applied the Hamiltonian approach for the accretion with isothermal equation of state. In section **3.5**, we have analyzed the nature of flow around conformal gravity BH for various cases of fluids such as ultra-stiff fluid, ultra-relativistic fluid, radiation fluid and sub-relativistic fluid. The polytropic fluid accretion has been discussed explicitly in section **3.6**. The mass accretion rate for various BHs is formulated in section **3.7**.

3.1 Conformal Gravity Black Hole

From conformal gravity BH given in Eq. (2.8), the choice $\gamma = 0$ yields the Schwarzschild-de Sitter solution and $\gamma = k = 0$ recover the Schwarzschild solution. If all three parameters of BH γ, β and k are not equal to zero, the BH can be termed as case **1**, which is a general case. If we impose $\gamma = 0$, then $A(r) = 1-\frac{2\beta}{r}-kr^2$ (Schwarzschild-de Sitter solution), which is the case **2**. We can get the Schwarzschild solution $A(r) = 1 - \frac{2\beta}{r}$ for $\gamma = k = 0$, which is the case **3**. In all these cases β is considered as mass of BH and k behaves as cosmological constant (Mannheim and Kazanas (1989, 1991)).

3.2 Horizon Structure

In this section, we study the horizons of the conformal gravity BH. For the metric function $A(r)$ given in Eq. (2.8), the effect of the parameters β, γ and k is significent. It is well known that the conformal gravity BH appears to describe a massive body fixed in a conformally flat space. The conformally flatness of the spherically symmetric space is characterized by the absolute influence of the massive body.

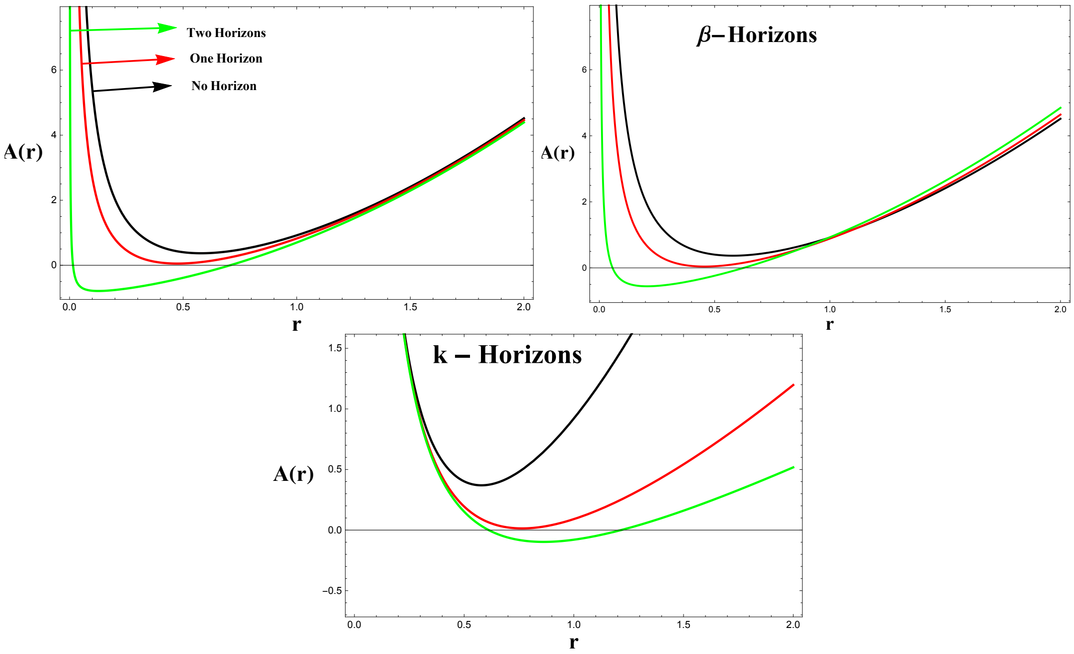

Figure 3.1: The horizon structure of conformal BH displays the behavior of $A(r)$ versus r. Left panel for various values of γ and others parameters are taken as fixed $k = -1$, $\beta = 0.96$. In the right panel, β horizons mean, we take various values of β. In the bottom panel, k horizons mean, we take various values of k.

As aforementioned by the analysis of Weyl tensor, the shattering of conformally flatness is evident at infinity.

For the radial distance $g_{rr} = 0$ or $A(r) = 0$, one would have an event horizon. Figure **3.1** (left panel) has the following key points:

- We have two horizons (green curve) for $\gamma = 0.70$.
- We have one horizon (red curve) for $\gamma = 0.84$.
- We have no horizons (black curve) for $\gamma = 0.95$.

Figure **1** (right panel) has the following key points:

- We have two horizons (green curve) for $\beta = 0.73$.

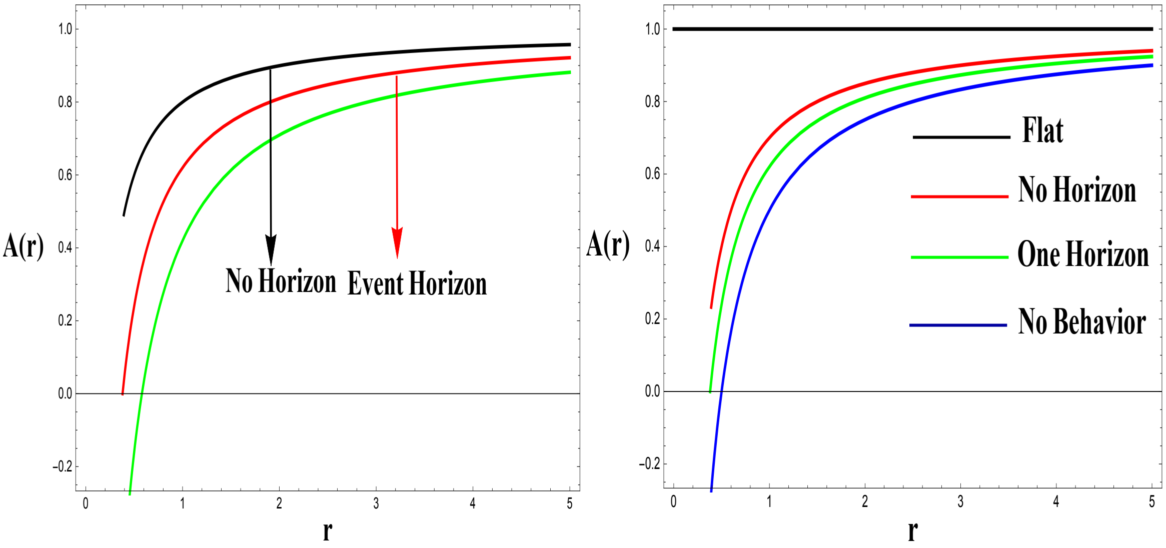

Figure 3.2: The horizon structure of Schwarzschild-de Sitter BH (left panel) and Schwarzschild BH (right panel) display the behavior of $A(r)$ versus r. The horizon curves of Schwarzschild-de Sitter BH are obtained for $\beta = 0.10, 0.19, 0.29$ and other parameters are taken as fixed $k = -0.0001$, $\gamma = 0$. The horizon curves of Schwarzschild BH are obtained for $\beta = 0, 0.15, 0.19, 0.25$ and others parameters are taken as fixed $k = 0$, $\gamma = 0$.

- We have one horizon (red curve) for $\beta = 0.86$.
- We have no horizons (black curve) for $\beta = 0.96$.

Figure **1** (bottom panel) has the following key points:

- We have two horizons (green curve) for $k = -0.0001$.
- We have one horizon (red curve) for $k = -0.17$.
- We have no horizons (black curve) for $k = -1$.

Figure **3.2** left panel presents the Schwarzschild-de Sitter BH horizon structure for $\gamma = 0$, there exists only one event horizon with the variations of β. In the right panel of Fig. **3.2**, one gets Schwarzschild solution for $\gamma = 0$ and $k = 0$, there is only one event horizon. When we take $\beta = 0$, the Schwarzschild solution is flat (see black curve). It is noted that when all parameters appearing from conformal gravity are set equal to zero then the solution is conformally flat as discussed by Mannheim and Kazanas (1989).

3.3 Spherically Symmetrically Accretion

The study of spherical accretion onto BHs describes the movement of fluid near the event horizon. Here, we assume two important laws that fully characterized the spherically accretion of isotropic perfect fluid. One is the law of conservation of mass and the other is the law of conservation of energy. We begin by the equation of continuity defined by Rezzolla and Zanotti (2013) as given in chapter 2.

3.4 Analysis of Various Cases of Black Holes

3.4.1 Case 1.

The first and general case of the line element is a conformal BH, which is given by Eq. (2.8). There are four subcases of case **1**:

3.4.1.1 Hamiltonian for ultra-stiff fluid ($\omega = 1$):

In this case, we have $p = \varrho$, from the equation of state and critical point and event horizon are equal, that is $r_h = r_c$, with the condition $A_c = 0$, which can be easily obtained by using Eqs. (2.70) and (2.71). The Hamiltonian (2.58) for this type of fluid takes the form

$$H = \frac{1}{v^2 {r_c}^4}. \tag{3.1}$$

3.4.1.2 Hamiltonian of ultra-relativistic fluid ($\omega = 1/2$):

In this case, the relation between energy density (ϱ) and pressure (p) is $p = \varrho/2$, with $\omega = 1/2$ in the equation of state, it means that the energy density is grater than the pressure. From Eqs. (2.70) and (2.71), we get $r_c A_c' - 4A_c = 0$, which gives

$$2k{r_c}^3 - 3\gamma {r_c}^2 + 4(3\beta\gamma - 1)r_c + 5\beta(2 - 3\beta\gamma) = 0. \tag{3.2}$$

The real solution of above equation is

$$r_c = \frac{\gamma}{2k} - \frac{24k - 72k\beta\gamma + 9\gamma^2}{3 \times 2^{2/3} kQ} + \frac{Q}{6 \times 2^{1/3} k}, \tag{3.3}$$

where

$$Q = \Big(- 1080k^2\beta + 216k\gamma + 1620k^2\beta^2\gamma - 648k\beta\gamma^2 + 54\gamma^3 \\ + \sqrt{4\left(-24k + 72k\beta\gamma - 9\gamma^2\right)^3 + \left(-1080k^2\beta + 216k\gamma + 1620k^2\beta^2\gamma - 648k\beta\gamma^2 + 54\gamma^3\right)^2}\Big)^{1/3}.$$

Using r_c from the above expression, we get v_c from Eq. (2.70) and have two critical points as $(r_c, \pm v_c)$. The Hamiltonian (2.58) reduces into the form:

$$H = \frac{\sqrt{A(r)}}{{r_c}^2 v \sqrt{1-v^2}}. \tag{3.4}$$

The graphical behavior can be seen between v and r_c with particular choice of $H = H_c$. From the above relation (3.4), we get

$$v^2 = \frac{1 \pm \sqrt{1-4X(r)}}{2}, \tag{3.5}$$

where $X(r) = \frac{A(r)}{H_c r^4}$.

3.4.1.3 Hamiltonian for radiation fluid ($\omega = 1/3$):

For radiation fluids, the equation of state takes the form $p = \varrho/3$. Using Eqs. (2.70) and (2.71), we have $r_c A'_c - 2A_c = 0$, which leads to

$$\gamma {r_c}^2 - (3\beta\gamma - 1) r_c - 3\beta(2 - 3\beta\gamma) = 0. \tag{3.6}$$

The critical solutions are

$$r_{c\pm} = \frac{2(3\beta\gamma - 1) \pm 2}{2\gamma}. \tag{3.7}$$

The Hamiltonian (2.58) in this case is given by

$$H = \frac{A(r)^{\frac{2}{3}}}{{r_c}^{\frac{4}{3}} v^{\frac{2}{3}} (1-v^2)^{\frac{2}{3}}}. \tag{3.8}$$

3.4.1.4 Hamiltonian for sub-relativistic fluid ($\omega = 1/4$):

For such fluids, the equation of state obeys the form $p = \varrho/4$. This form shows the energy density exceeds than the isotropic pressure. Using Eqs. (2.70) and (2.71), we get $4A_c - 3r_c A'_c = 0$, which reduces to

$$2k{r_c}^3 + \gamma {r_c}^2 - 4(3\beta\gamma - 1) r_c - 7\beta(2 - 3\beta\gamma) = 0. \tag{3.9}$$

$$r_c = \frac{\gamma}{3k} - \frac{2^{1/3}\left(-3k + 9k\beta\gamma - \gamma^2\right)}{3kS} + \frac{S}{3\ 2^{1/3} k} \tag{3.10}$$

$$S = \left(P + \sqrt{4\left(-3k + 9k\beta\gamma - \gamma^2\right)^3 + P^2}\right)^{1/3}$$
$$P = -54k^2\beta + 9k\gamma + 81k^2\beta^2\gamma - 27k\beta\gamma^2 + 2\gamma^3.$$

After determining the critical points, the Hamiltonian is given by

$$H = \frac{A(r)^{\frac{3}{4}}}{r_c v^{\frac{1}{2}}(1 - v^2)^{\frac{3}{4}}}. \tag{3.11}$$

3.4.2 Case 2

The second case of the line element is known as Schwarzschild-de Sitter BH, the Hamiltonian and critical points for such BH can be obtained by taking $\gamma = 0$ in **Case 1**.

3.4.3 Case 3

The third and final case of the line element is called Schwarzschild solution, the Hamiltonian and critical points for such BH can be obtained by taking $\gamma = k = 0$ in **Case 1**.

3.4.4 Visualization of results for all cases

This section elaborates the results of ultra-stiff fluids ($\omega = 1$), ultra-relativistic fluids ($\omega = \frac{1}{2}$), radiation fluids ($\omega = \frac{1}{3}$) and sub-relativistic fluids ($\omega = \frac{1}{4}$) for conformal gravity BH (Case 1), Schwarzschild de-Sitter BH (Case 2) and Schwarzschild BH (Case 3).

1. **Ultra-stiff fluids ($\omega = 1$):**

   Figure **3.3** signifies the velocity v of moving fluid versus the radius r corresponding to various cases of BH. The fluid motion occurs in the two regions, upper curves show the region $v > 0$ whereas the lower curves for the region $v < 0$ for the three cases of BH. It is noted here that the critical point is always

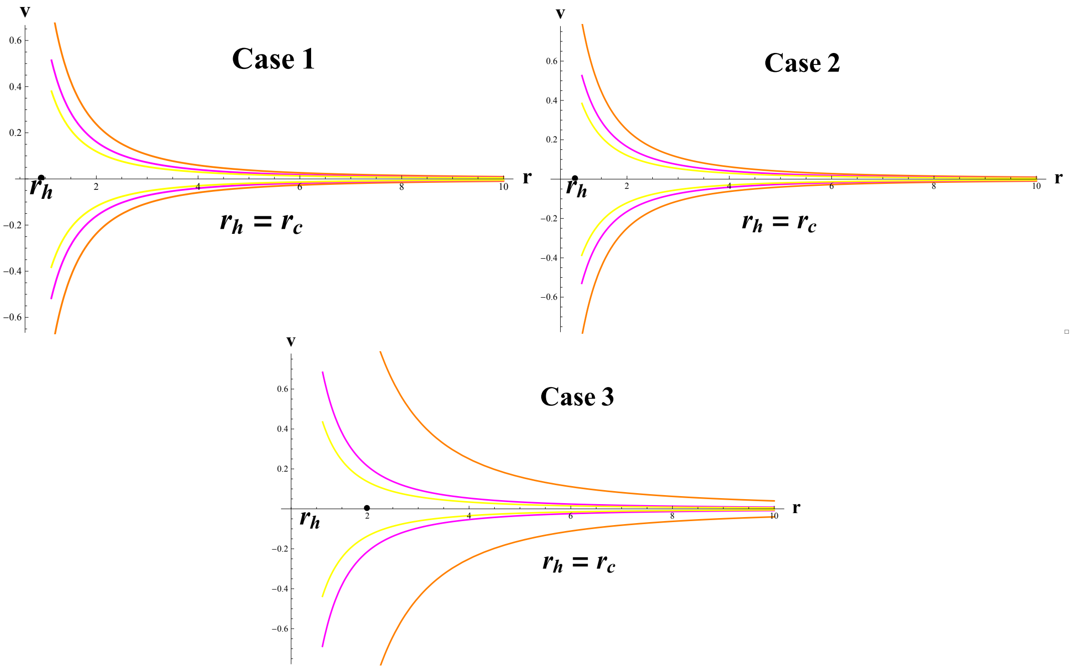

Figure 3.3: The left panel (conformal gravity BH) displays the behavior of Eq. (3.1) with conformal parameters $\gamma = 0.1$, $k = -1$, $\beta = 1$. The critical parameters are chosen as $r_c \approx 0.9738$, $v_c = 1$, $H_c \approx 1.112$. The right panel (Schwarzschild de-Sitter BH) displays the behavior of Eq. (3.1) with Schwarzschild de-Sitter BH parameters $\gamma = 0$, $k = -1$, $\beta = 1$. The critical parameters are chosen as $r_c \approx 1.001$, $v_c = 1$, $H_c \approx 1.001$. The bottom panel (Schwarzschild BH) displays the behavior of Eq. (3.1) with Schwarzschild BH parameters $\gamma = 0$, $k = 0$, $\beta = 1$. The critical parameters are chosen as $r_c = 2$, $v_c = 1$, $H_c \approx 0.0625$. The representation of colors for $H = H_c \rightarrow$ orange, $H > H_c \rightarrow$ magenta and yellow.

equal to the critical horizon for ultra-stiff fluid. Moreover, the critical points are closer in conformal gravity BH and Schwarzschild de-Sitter BH as compare to the Schwarzschild BH. It is observed that the critical points are close to the singularity in conformal gravity BH and Schwarzschild de-Sitter BH than the Schwarzschild BH.

2. **Ultra-relativistic fluids ($\omega = \frac{1}{2}$):**
   We see the velocity essence of moving fluid v versus the radius r for aforementioned all three cases of conformal gravity BH by putting the corresponding values of $A(r)$ in Fig. **3.5**. The critical values of horizon, radius and velocity (r_h, r_c, v_c) are nearly equal to (0.974, 1.297, 0.707107), (1.3333, 1.3282, 0.707107) and (2.0025, 2.524, 0.707107) for the cases 1, 2 and 3, respectively. For $H = H_c = 1.3030$ (Case 1), $H = H_c = 1.27174$ (Case 2) and $H = H_c = 0.1431$ (Case 3), the behavior of curves is seen through the critical points $(r_c, \pm v_c)$. It is shown that the fluid outflow starts from the horizon and induces by the high pressure. The curves behaviors shown in Fig. **3.4** are not all physical. For increasing radius r, the region must be $v > 0$ (positive), while for decreasing radius the region must be $v < 0$ (negative). The flow in the yellow, magenta, orange and purple curves is unphysical. The fluid flow increases as $v > 0$ and decreases the radius, so there is neither fluid outflow nor an accretion. It is also noted here that the fluid elements are closer in Case **1** and Case **2** as compared to Case **3**, respectively. Consequently, it is viewed that the critical points are closer in Case **1** and Case **2** as compared to Case **3**, respectively. Specially, in Case **3** (Schwarzschild case), only the orange curve represents the unphysical while the other four color curves show the physical behavior which is clear as compare to Case **1** and Case **2**. Further, Fig. **3.4** shows the following four key points.

   - We notice, the subsonic/supersonic accretion occurs in the ranges $-v_c <$

$v < 0$ and $-1 < v < -v_c$, whereas supersonic/subsonic fluid outflows for $v_c < v < 1$ and $0 < v < v_c$, respectively.

- The emission of particles for $v > v_c$ and thus purely supersonic accretion for $v < -v_c$.
- The subsonic outflow followed by the subsonic accretion with $v_c > v > -v_c$.
- The upper plot shows the supersonic outflow followed by subsonic motion, while the lower plot shows the subsonic accretion followed by supersonic accretion.

Consequently, we observe that the starting point of the fluid outflow is at horizon due to its very high pressure which influences to divergence and as a result, the fluid with its high pressure, flows back to infinity as analyzed by Chakrabarti (2011). We also observe from Fig. **3.4**, the supersonic accretion (fluid outflow) followed by subsonic accretion (fluid inflow) stops inside the horizon (Ahmed at el. 2016). It means that for conformal gravity BH, Schwarzschild de-Sitter BH and Schwarzschild BH the flow of the fluid is neither supersonic nor transonic near the horizon as found by Novikov and Thorne (1973) and Chakrabarti (1990). The analysis of stability can be done by using Lyapunov's theorem or linearization of dynamical system as studied by Nagle (2012) and their variations as defined by Azreg (2013).

3. **Radiation fluids ($\omega = \frac{1}{3}$):**

The rule played by the different parameters for the velocity profile v versus radius r is important in Fig. **3.5**. The settlement of curves corresponding to $H = H_c$ is colored orange. The Magenta and Yellow curves relate to $H < H_c$ and the Purple and Red plots to $H > H_c$. In Fig. **3.5**, we see the supersonic outflows of the fluid in the range $v_c < v < 1$. In this flow, we observe that the orange curve exactly passes through the critical point ($r_c = 3.0$) as compared

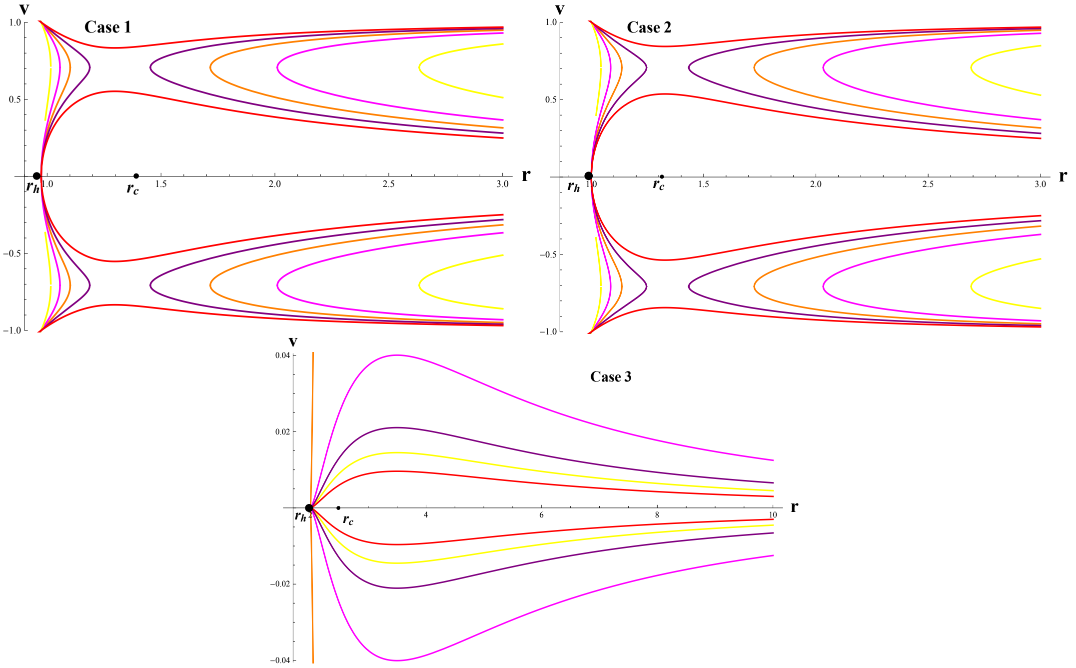

Figure 3.4: For the accretion flow, the left panel (conformal gravity BH) displays the behavior of Eq. (3.5) with conformal parameters $\gamma = 0.1$, $k = -1$, $\beta = 1$. The critical parameters involve $r_c \approx 1.29701$, $v_c = 0.70716$, $H_c \approx 1.30306$. Right panel (Schwarzschild de-Sitter BH) displays the behavior of Eq. (3.5) with Schwarzschild de-Sitter BH parameters $\gamma = 0$, $k = -1$, $\beta = 1$. The values of the critical parameters are $r_c \approx 1.32827$, $v_c = 0.70716$, $H_c \approx 1.27174$. Bottom panel (Schwarzschild BH) displays the behavior of Eq. (3.5) with Schwarzschild BH parameters $\gamma = 0$, $k = 0$, $\beta = 1$. The values of the critical parameters are $r_c = 2.5$, $v_c = 0.70716$, $H_c \approx 0.143108$. The representation of colors in $H = H_c \rightarrow$ orange, $H > H_c \rightarrow$ magenta and yellow, $H < H_c \rightarrow$ purple and red.

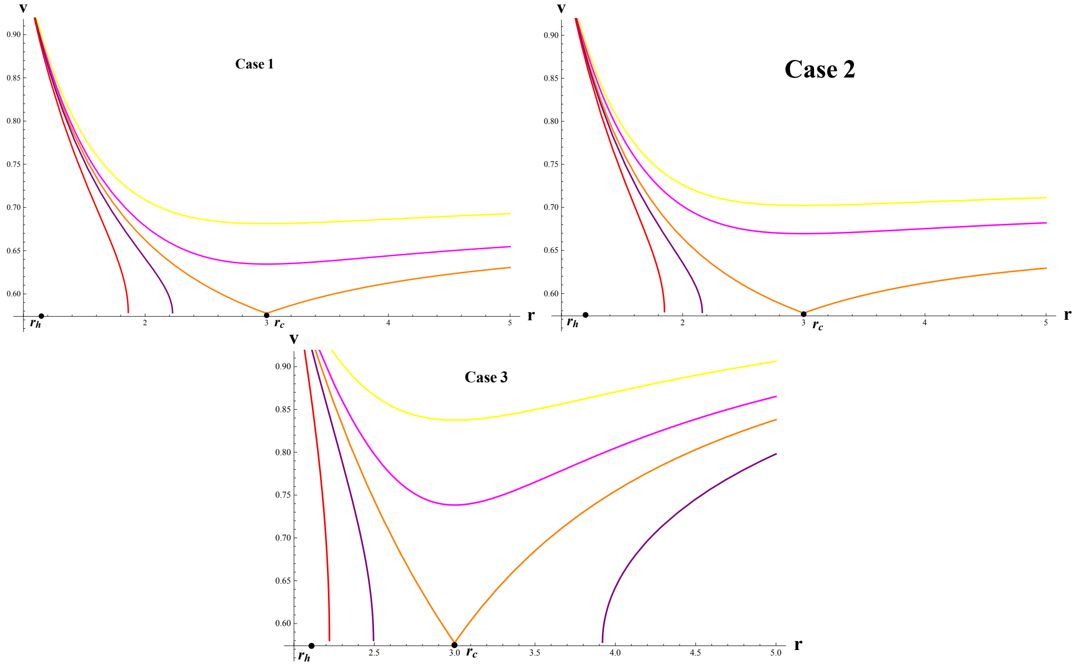

Figure 3.5: In the physical structure of accretion, left panel (conformal gravity BH) displays the behavior of Eq. (3.8) with conformal parameters $\gamma = 0.1$, $k = -1$, $\beta = 1$. The critical parameters involve $r_c \approx 3$, $v_c = 0.5773$, $H_c \approx 1.95007$. Right panel (Schwarzschild de-Sitter BH) displays the behavior of Eq. (3.8) with Schwarzschild de-Sitter BH parameters $\gamma = 0$, $k = -1$, $\beta = 1$. The critical parameters involve $r_c \approx 3$, $v_c = 0.5773$, $H_c \approx 1.93626$. Bottom panel (Schwarzschild BH) displays the behavior of Eq. (3.8) with Schwarzschild BH parameters $\gamma = 0$, $k = 0$, $\beta = 1$. The critical parameters involve $r_c = 3$, $v_c = 0.5773$, $H_c \approx 0.20998$. The representation of colors in $H = H_c \rightarrow$ orange, $H > H_c \rightarrow$ magenta and yellow, $H < H_c \rightarrow$ purple and red.

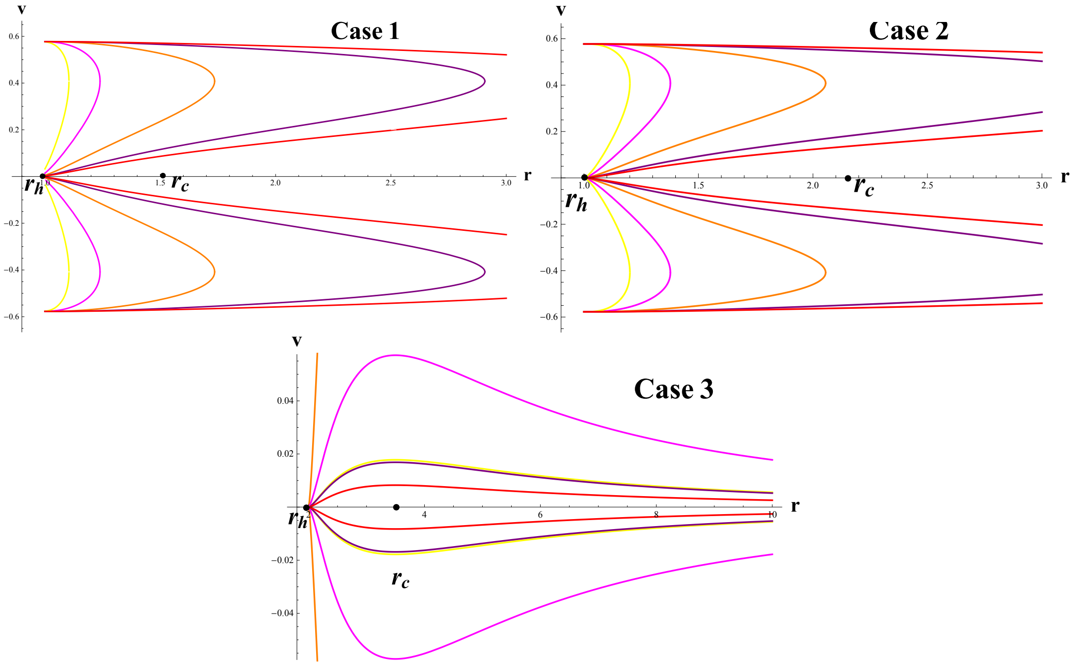

Figure 3.6: In the physical structure of accretion, left panel (conformal gravity BH) displays the behavior of Eq. (3.11) with conformal parameters $\gamma = 0.1$, $k = -1$, $\beta = 1$. The critical parameters involve $r_c \approx 1.54267$, $v_c = 0.5$, $H_c \approx 2.38717$. Right panel (Schwarzschild de-Sitter BH) displays the behavior of Eq. (3.11) with Schwarzschild de-Sitter BH parameters $\gamma = 0$, $k = -1$, $\beta = 1$. The critical parameters involve $r_c \approx 2.25826$, $v_c = 0.5$, $H_c \approx 2.6812$. Bottom panel (Schwarzschild BH) displays the behavior of Eq. (3.11) with Schwarzschild BH parameters $\gamma = 0$, $k = 0$, $\beta = 1$. The critical parameters are taken as $r_c = 3.5$, $v_c = 0.5$, $H_c \approx 0.26556$. The representation of colors in $H = H_c \rightarrow$ orange, $H > H_c \rightarrow$ magenta and yellow, $H < H_c \rightarrow$ purple and red.

to other curves. The critical points are very close in Case **1** and Case **2** than Case **3**. So, the orange, magenta and yellow curves are purely supersonic outflows for $(v > v_c)$ and these curves pass through the critical speed Fig. **3.6** in Schwarzschild BH. One can see the similar behavior for conformal gravity BH and Schwarzschild de-Sitter BH. The vertical lines which are closer to the horizon are unphysical for $H > H_c$.

4. **Sub-relativistic fluids ($\omega = \frac{1}{4}$):**
   We have analyzed the accretion of the sub-relativistic fluid $\omega = \frac{1}{4}$ for the conformal gravity BH. We have plotted the sub-relativistic fluid motion versus the radius in Fig. **3.6**. This figure shows that all the solution curves are not passing through the critical velocity, which confirms to the new solution in Schwarzschild BH. Since, the critical velocity is located at $v_c \approx 0.5$ but the maximum speed in case of Schwarzschild BH approaches to $v = 0.06$. So, there is no accretion flow around Schwarzschild BH for sub-relativistic fluid. We have observed the supersonic accretion at $v > v_c$ followed by subsonic accretion at $0 < v < v_c$ which stop at the horizon for conformal gravity BH and Schwarzschild de-Sitter BH. Furthermore, we have the supersonic accretion with $v < -v_c$ followed by the subsonic accretion at $0 < \nu < -\nu_c$.

3.5 Polytropic Fluids Accretion

The polytropic EoS was considered by Ahmad et al. (2016) and Jawad and Shahzad (2017), which is discussed in section **2.6.3.** Now by using Eq. (2.78), we find the Hamiltonian of polytropic fluids for different cases of conformal gravity BH.

1. Hamiltonian for conformal gravity BH

$$H = \frac{\left(1-\frac{\beta(2-3\beta\gamma)}{r}-3\beta\gamma+\gamma r-kr^2\right)}{1-v^2}\Big[1 \\ +X\Big(\frac{1-v^2}{r^4v^2\left(1-\frac{\beta(2-3\beta\gamma)}{r}-3\beta\gamma+\gamma r-kr^2\right)}\Big)^{(\alpha-1)/2}\Big]^2. \tag{3.12}$$

2. Hamiltonian for Schwarzschild de-Sitter BH

$$H = \frac{\left(1-\frac{2\beta}{r}-kr^2\right)}{1-v^2}\Big[1+X\Big(\frac{1-v^2}{r^4v^2(1-\frac{2\beta}{r}-kr^2)}\Big)^{(\alpha-1)/2}\Big]^2. \tag{3.13}$$

3. Hamiltonian for Schwarzschild BH

$$H = \frac{1-\frac{2\beta}{r}}{1-v^2}\Big[1+X\Big(\frac{1-v^2}{r^4v^2(1-\frac{2\beta}{r})}\Big)^{(\alpha-1)/2}\Big]^2. \tag{3.14}$$

It is analyzed from the Hamiltonian results that $\frac{dA(r)}{dr} > 0$ for all r.

Adopting the technique of Ahmad et al. (2016) and Jawad and Shahzad (2017), one can get the following relation

$$(\alpha-1-v_c^2)\left(\frac{1-v_c^2}{r_c^4A(r_c)v_c^2}\right)^{\frac{\alpha-1}{2}} = \frac{n_c}{2X}\left(r_c^5A'(r_c)\right)^{\frac{1}{2}v_c^2}, \tag{3.15}$$

$$v_c^2 = \frac{r_cA'_{rc}}{r_cA'_{r_c}+4A(r_c)}. \tag{3.16}$$

Figure **3.7** represents the contour plots for conformal BH (left panel), Schwarzschild de-Sitter BH (right panel) and Schwarzschild BH (bottom panel) with $n_c = 0.15$, $X = 5$, $\alpha = 5/3$. We have presented the behavior of matter by taking the sonic points $r_c \approx 1.9855$, $v_c \approx 0.56218$, $H = H_c \simeq 4.2876$ for conformal BH, $r_c \approx 3.7859$, $v_c \approx 0.44216$, $H = H_c \simeq 2.1377$ for Schwarzschild de-Sitter BH and $r_c \approx 5.2865$, $v_c \approx 0.24211$, $H = H_c \simeq 1.9374$ for Schwarzschild BH. It is analyzed that the critical flow for conformal BH, Schwarzschild de-Sitter BH and Schwarzschild BH begins from the region of Killing horizon and ends at the subsonic accretion as r approaches to infinity. It has been observed that the accretion behavior of various BHs is different at critical points of polytropic test fluids case. Also, it has been

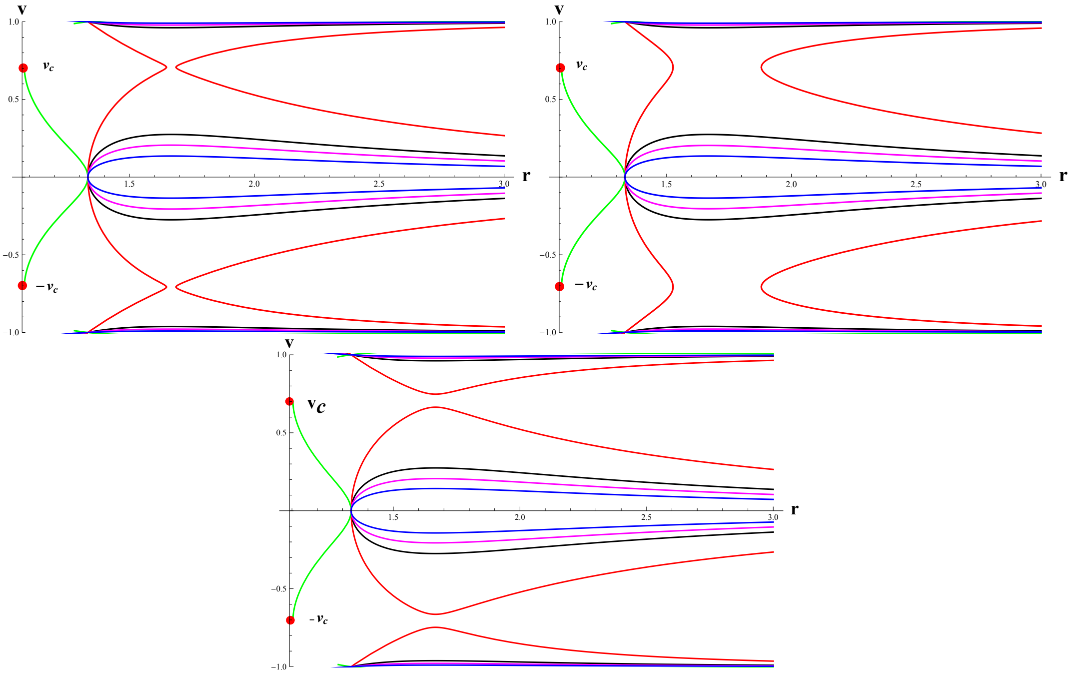

Figure 3.7: For the polytropic fluid accretion, left panel (conformal gravity BH) displays the behavior of (3.12). Right panel (Schwarzschild de-Sitter BH) displays the behavior of (3.13). Bottom panel (Schwarzschild BH) displays the behavior of (3.14). (Figure color online).

observed that at the trajectory of conformal BH, the critical points are closer (see red curve), for Schwarzschild de-Sitter BH, the critical points are also distant (see red curve) and for Schwarzschild BH, the critical points are also distant (see red curve). In all these cases, the trajectories do not pass through the saddle point (sonic point).

3.6 Black Hole's Mass Accretion Rate

Exact solution for ultra-stiff fluids $\omega = 1$:

By assuming $\omega = 1$ in Eqs. (2.92) and (2.93), one can calculate the radial velocity and energy-density of ultra-stiff fluids, that is

$$u = \pm L_1^2 \sqrt{\frac{A(r)}{L_0^2 r^4 - 4L_1^4}}, \tag{3.17}$$

also the energy density is given by

$$\varrho = \frac{(L_0^2 r^4 - 4L_1^4)}{4L_1^2 r^4 A(r)}. \tag{3.18}$$

From Eqs. (2.92) and (3.18), the mass accretion rate of conformal gravity BH can obtained in the following form

$$\dot{M} = \frac{2\pi(L_0^2 r^4 - 4L_1^4)}{L_1 r^3 \left[3\beta^2\gamma - 2\beta + (1 - 3\beta\gamma)r + \gamma r^2 - kr^3\right]} \qquad (\text{Case} \quad \mathbf{1}). \tag{3.19}$$

Similarly, following the same method, we can find the mass accretion rate for Schwarzschild de-Sitter and Schwarzschild BHs

$$\begin{aligned} \dot{M} &= \frac{2\pi(L_0^2 r^4 - 4L_1^4)}{L_1 r^3 \left[-2\beta + r - kr^3\right]}. && (\text{Case} \quad \mathbf{2}) && (3.20) \\ \dot{M} &= \frac{2\pi(L_0^2 r^4 - 4L_1^4)}{L_1 r^3 \left[-2\beta + r\right]}. && (\text{Case} \quad \mathbf{3}) && (3.21) \end{aligned}$$

In Fig. **3.8**, we plot the mass accretion-rate $\dot{M}$ versus the radius r for aforemention BHs in ultra-stiff fluid, other parameters γ, k and β are taken as fixed. In

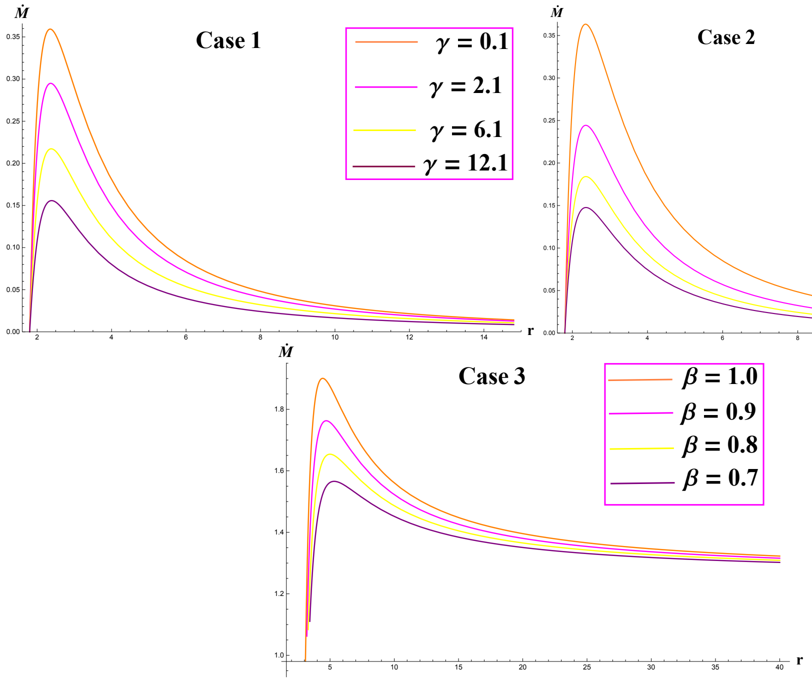

Figure 3.8: In this figure, left panel (conformal gravity BH) displays the behavior of Eq. (3.19) with conformal parameters $\gamma = 0.1$, $k = -1$, $\beta = 1$. Right panel (Schwarzschild de-Sitter BH) displays the behavior of Eq. (3.20) for Schwarzschild de-Sitter BH parameters $\gamma = 0$, $k = -1$, $\beta = 1$. Bottom panel (Schwarzschild BH) displays the behavior of Eq. (3.21) for Schwarzschild BH parameters $\gamma = 0$, $k = 0$, $\beta = 1$. Other constants are taken as $L_0 = 0.90$, $L_1 = 0.5$.

the left panel (conformal gravity BH) the accretion rate is increased by decreasing the parameter γ. It has been noted that the maximum accretion rate occurs for overlapping the critical radius in the presence of different values of γ. For the left panel the values of mass accretion rate are: $\dot{M} = 0.15, 0.235, 0.29, 0.36$ for $\gamma = 12.1, 6.1, 2.1, 0.1$, we have the overlapping radius $r \approx 1.931$, respectively. The same critical points are seen in the right panel (Schwarzschild de-Sitter BH) in the presence of parameter k. The critical values are: $\dot{M} = 0.15, 0.235, 0.29, 0.36$ for $k = -2.5, -2.0, -1.5, -1.0$, we have the overlapping radius $r \approx 1.931$, respectively. The right panel increases the mass of Schwarzschild de-Sitter BH by increasing the cosmological constant parameter k. Now, the maximum mass accretion rate of Schwarzschild BH occurs in bottom panel, such as $\dot{M} = 15.5, 16.5, 17.5, 18.5$ occur for different values of parameters

- $\beta = 0.7$, corresponding to $r \approx 2.536$
- $\beta = 0.8$, corresponding to $r \approx 2.936$
- $\beta = 0.9$, corresponding to $r \approx 3.156$
- $\beta = 1.0$, corresponding to $r \approx 3.956$

The mass accretion rate of Schwarzschild BH is increased by increasing the mass, β). Hence, we conclude that the mass of Schwarzschild BH is larger as compare to conformal gravity BH and Schwarzschild de-Sitter BH.

Exact solution for ultra-relativistic fluids $\omega = 1/2$:

By assuming $\omega = 1/2$ in Eqs. (2.92) and (2.93), one can calculate the radial velocity and energy-density of ultra-relativistic fluids, that is

$$u = \frac{2r^2L_0^2+\sqrt{4r^2L_0^4-81A(r)L_1^6}}{9L_1^3}. \tag{3.22}$$

$$\varrho = 27\left(\frac{L_1^4}{r^2(2r^2L_0^2+\sqrt{4r^2L_0^4-81A(r)L_1^6})}\right)^{3/2}. \tag{3.23}$$

$$\dot{M} = 216\pi L_1\left(\frac{L_1^4}{r^2(2r^2L_0^2+\sqrt{4r^2L_0^4-81A(r)L_1^6})}\right)^{3/2}. \tag{3.24}$$

1. The mass accretion rate of conformal gravity BH is

$$\begin{aligned}\dot{M} = {} & 216\pi L_1 \\ & \times\left(\frac{L_1^4}{r^2(2r^2L_0^2+\sqrt{4r^2L_0^4-81(1-\frac{\beta(2-3\beta\gamma)}{r}-3\beta\gamma+\gamma r-kr^2)L_1^6})}\right)^{3/2}.\end{aligned} \tag{3.25}$$

2. The mass accretion rate of Schwarzschild de-Sitter BH is

$$\begin{aligned}\dot{M} = {} & 216\pi L_1 \\ & \times\left(\frac{L_1^4}{r^2(2r^2L_0^2+\sqrt{4r^2L_0^4-81(1-\frac{2\beta}{r}-kr^2)L_1^6})}\right)^{3/2}.\end{aligned} \tag{3.26}$$

3. The mass accretion rate of Schwarzschild BH is

$$\begin{aligned}\dot{M} = {} & 216\pi L_1 \\ & \times\left(\frac{L_1^4}{r^2(2r^2L_0^2+\sqrt{4r^2L_0^4-81(1-\frac{2\beta}{r})L_1^6})}\right)^{3/2}.\end{aligned} \tag{3.27}$$

In Fig. **3.9**, we plot the mass accretion-rate ($\dot{M}$) versus the radius (r) for aforemention BHs in ultra-relativistic fluid. The left panel (conformal gravity BH) represents that the mass accretion rate is decreasing for larger value of r, that is $\dot{M} =$

7000 for $r = 0.8$ and Killing horizon is at $r_{KH} \approx 0.8$ whereas the universal horizon is at $r_{UH} \approx 0.1$. The accretion rate is increasing for smaller values of the radius, that is $\dot{M} > 8000$ for $r \simeq 0.65$ and the Killing horizon is at $r_{KH} \approx 0.65$ whereas the universal horizon is at $r_{UH} \approx 0.2$. We can say that the mass of the conformal gravity BH decreases whereas the radius increases, on the other hand the accretion rate is an increasing function of radius. In this case, the critical points are overlapping at the universal horizon. This implies that the mass of Schwarzschild de-Sitter BH decreases whereas the radius increases, on the other hand the accretion rate is an increasing function of radius in the presence of cosmological constant k.

Now, the maximum mass accretion rate of Schwarzschild BH occurs in bottom panel for smaller radius. The critical points are overlapping at the universal horizon but these points are away from the killing horizon in the presence of mass function β. Four key points are observed for the Schwarzschild BH:

- $\beta = 0.7$, corresponding to $r_{UH} \approx 0.135$, $r_{KH} \approx 0.65$.
- $\beta = 0.8$, corresponding to $r_{UH} \approx 0.133$, $r_{KH} \approx 0.70$.
- $\beta = 0.9$, corresponding to $r_{UH} \approx 0.131$, $r_{KH} \approx 0.75$.
- $\beta = 1.0$, corresponding to $r_{UH} \approx 0.129$, $r_{KH} \approx 0.80$.

The accretion rate of Schwarzschild BH is increasing with the decreasing values of radius. Hence, we conclude that mass of the Schwarzschild BH is larger as compare to conformal gravity BH and Schwarzschild de-Sitter BH.

Exact solution for radiation fluid $\omega = 1/3$:

By assuming $\omega = 1/2$ in Eqs. (2.92) and (2.93), one can calculate the radial velocity and energy-density of radiation fluids, that is

$$u = \Big[\frac{\Big(-32A(r)L_1^4 + \sqrt{1024A(r)^2L_1^8 - 27r^4L_0^6}\Big)^{1/3}}{4L_1^2} + \frac{3r^{4/3}L_0^2}{4L_1^{2/3}\Big(-32A(r)L_1^4 + \sqrt{1024A(r)^2L_1^8 - 27r^4L_0^6}\Big)^{1/3}}\Big]^{2/3}. \tag{3.28}$$

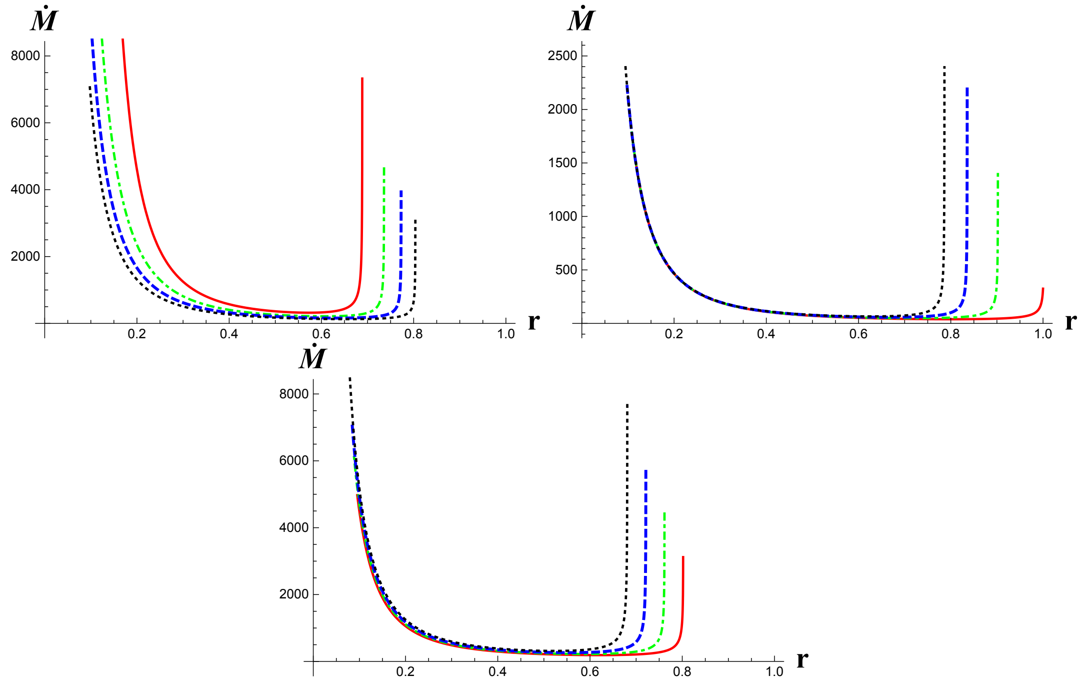

Figure 3.9: In the mass accretion rate, left panel (conformal gravity BH) displays the behavior of Eq. (3.25) with conformal parameters $\gamma = 0.1$, $k = -1$, $\beta = 1$. Right panel (Schwarzschild de-Sitter BH) displays the behavior of Eq. (3.26) with Schwarzschild de-Sitter BH parameters $\gamma = 0$, $k = -1$, $\beta = 1$. Bottom panel (Schwarzschild BH) displays the behavior of Eq. (3.27) with Schwarzschild BH parameters $\gamma = 0$, $k = 0$, $\beta = 1$. Other constants are taken as $L_0 = 0.90$, $L_1 = 0.5$.

The energy density of the fluid is given by

$$\begin{aligned} \varrho = \quad & \Big[\frac{L_1}{r^2}\Big]^{\frac{4}{3}}\Big[\frac{\Big(-32A(r)L_1^4+\sqrt{1024A(r)^2L_1^8-27r^4L_0^6}\Big)^{1/3}}{4L_1^2} \\ & +\frac{3r^{4/3}L_0^2}{4L_1^{2/3}\Big(-32A(r)L_1^4+\sqrt{1024A(r)^2L_1^8-27r^4L_0^6}\Big)^{1/3}}\Big]^{\frac{-8}{9}}. \end{aligned} \tag{3.29}$$

The general form of the mass of BH is given by

$$\begin{aligned} \dot{M} = \quad & \Big[\frac{8\pi L_1^{\frac{7}{3}}}{r^{\frac{8}{3}}}\Big]\Big[\Big(-32A(r)L_1^4+\sqrt{1024A(r)^2L_1^8-27r^4L_0^6}\Big)^{1/3}\Big(4L_1^2\Big)^{-1} \\ & +\frac{3r^{4/3}L_0^2}{4L_1^{2/3}}\times\Big(-32A(r)L_1^4+\sqrt{1024A(r)^2L_1^8-27r^4L_0^6}\Big)^{-1/3}\Big]^{\frac{-8}{9}}. \end{aligned} \tag{3.30}$$

1. The mass accretion rate of conformal gravity BH is

$$\begin{aligned} \dot{M} = \quad & \Big[\frac{8\pi L_1^{\frac{7}{3}}}{r^{\frac{8}{3}}}\Big]\Big[\Big(-32(1-\frac{\beta(2-3\beta\gamma)}{r}-3\beta\gamma+\gamma r-kr^2)L_1^4 \\ & +\sqrt{1024\Big(1-\frac{\beta(2-3\beta\gamma)}{r}-3\beta\gamma+\gamma r-kr^2\Big)^2L_1^8-27r^4L_0^6}\Big)^{1/3}\Big(4L_1^2\Big)^{-1} \\ & +\frac{3r^{4/3}L_0^2}{4L_1^{2/3}}\times\Big(-32(1-\frac{\beta(2-3\beta\gamma)}{r}-3\beta\gamma+\gamma r-kr^2)L_1^4 \\ & +\sqrt{1024\Big(1-\frac{\beta(2-3\beta\gamma)}{r}-3\beta\gamma+\gamma r-kr^2\Big)^2L_1^8-27r^4L_0^6}\Big)^{-1/3}\Big]^{\frac{-8}{9}}. \end{aligned} \tag{3.31}$$

2. The mass accretion rate of Schwarzschild de-Sitter BH is

$$\begin{aligned} \dot{M} \quad & =\Big[\frac{8\pi L_1^{\frac{7}{3}}}{r^{\frac{8}{3}}}\Big]\Big[\Big(-32(1-\frac{2\beta}{r}-kr^2)L_1^4 \\ & +\sqrt{1024\Big(1-\frac{2\beta}{r}-kr^2\Big)^2L_1^8-27r^4L_0^6}\Big)^{1/3}\Big(4L_1^2\Big)^{-1} \\ & +\frac{3r^{4/3}L_0^2}{4L_1^{2/3}}\times\Big(-32(1-\frac{2\beta}{r}-kr^2))L_1^4 \\ & +\sqrt{1024\Big(1-\frac{2\beta}{r}-kr^2\Big)^2L_1^8-27r^4L_0^6}\Big)^{-1/3}\Big]^{\frac{-8}{9}}. \end{aligned} \tag{3.32}$$

3. The mass accretion rate of Schwarzschild BH is

$$
\begin{aligned}
\dot{M} \quad &= \Big[\frac{8\pi L_1^{\frac{7}{3}}}{r^{\frac{8}{3}}}\Big]\Big[\Big(-32(1-\frac{2\beta}{r})L_1^4 \\
&+\sqrt{1024\Big(1-\frac{2\beta}{r}\Big)^2 L_1^8 - 27r^4 L_0^6}\Big)^{1/3}\Big(4L_1^2\Big)^{-1} \\
&+\frac{3r^{4/3}L_0^2}{4L_1^{2/3}} \times \Big(-32(1-\frac{2\beta}{r})L_1^4 \\
&+\sqrt{1024\Big(1-\frac{2\beta}{r}\Big)^2 L_1^8 - 27r^4 L_0^6}\Big)^{-1/3}\Big]^{\frac{-8}{9}}.
\end{aligned}
\tag{3.33}
$$

In Fig. **3.10**, we plot mass accretion-rate $\dot{M}$ versus the radius r for aforemention BHs for radiation fluid with the parameters γ, k and β. The left panel (conformal gravity BH) represents the decreasing mass accretion rate for smaller value of r. The maximum mass accretion rate is noted at the universal, but far from the Killing horizon. It is the increasing function of the radius in the presence of γ. The red curve in the right panel depicts the minimum accretion rate at the universal and the Killing horizon for Schwarzschild de-Sitter BH due to the parameter k. However, the accretion rate increases for smaller values of k and we can see the maximum accretion rate near $r \approx 1.08, 0.82, 0.75, 0.69$ for $k = -1.0, -1.5, -2.0, -2.5$, respectively. It is the decreasing function of radius that is mass increases when radius decreases.

We note that for Schwarzschild BH, the range of the maximum accretion rate is between the radius 0.5 to 0.6, for larger value of $\beta = 4$. It is also the decreasing function of the radius that is accretion rate increases whereas the radius decreases. So, four key points are observed for the Schwarzschild BH:

- $\beta = 1.0$, *corresponding to* $r_{UH} \approx 0.4$, $r_{KH} \approx 1.0$.
- $\beta = 2.0$, *corresponding to* $r_{UH} \approx 0.4$, $r_{KH} \approx 0.90$.
- $\beta = 3.0$, *corresponding to* $r_{UH} \approx 0.4$, $r_{KH} \approx 0.70$.

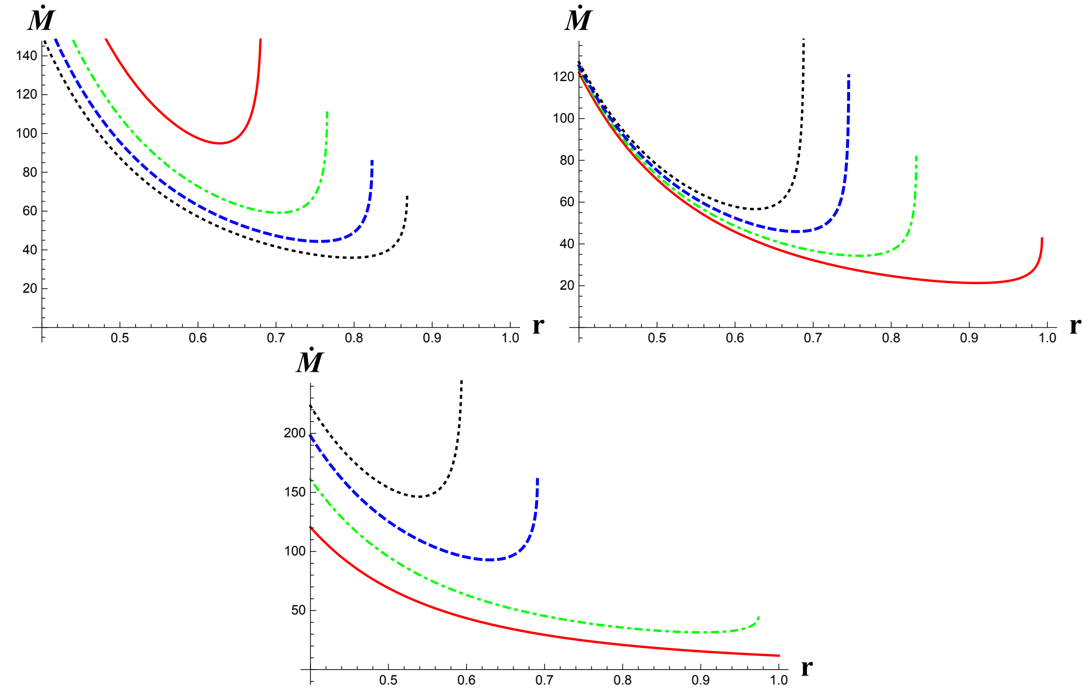

Figure 3.10: For the mass accretion rate, left panel (conformal gravity BH) displays the behavior of Eq. (3.31) with conformal parameters $\gamma = 0.1$, $k = -1$, $\beta = 1$. Right panel (Schwarzschild de-Sitter BH) displays the behavior of Eq. (3.32) with parameters $\gamma = 0$, $k = -1$, $\beta = 1$. Bottom panel (Schwarzschild BH) displays the behavior of (3.33) with the parameters $\gamma = 0$, $k = 0$, $\beta = 1$. Other constants are taken as $L_0 = 0.90$, $L_1 = 0.5$.

- $\beta = 4.0$, *corresponding to* $r_{UH} \approx 0.4$, $r_{KH} \approx 0.60$.

The mass accretion rate of Schwarzschild BH is increasing and the radius decreases for increasing values of the mass function. Hence, we conclude that the mass of Schwarzschild BH is larger as compared to conformal gravity BH and Schwarzschild de-Sitter BH.

We plot mass accretion-rate ($\dot{M}$) versus the radius (r) for aforemention BHs in the case of sub-relativistic fluid with particular values of conformal parameters γ, k and β, as shown in Fig. **3.11**. The left panel (conformal gravity BH) denotes

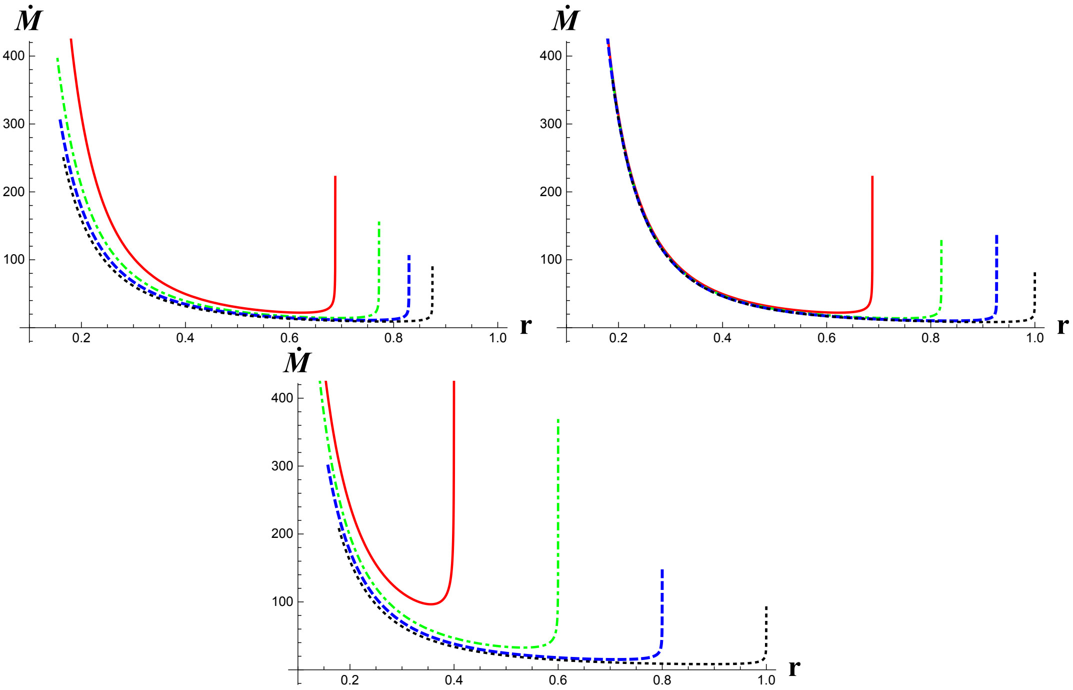

Figure 3.11: For the mass accretion rate, left panel displays the behavior of conformal gravity BH with conformal parameters $\gamma = 0.1$, $k = -1$, $\beta = 1$. Right panel displays the behavior of Schwarzschild de-Sitter BH with parameters $\gamma = 0$, $k = -1$, $\beta = 1$. Bottom panel displays the behavior of Schwarzschild BH with parameters $\gamma = 0$, $k = 0$, $\beta = 1$. Other constants are taken as $L_0 = 0.90$, $L_1 = 0.5$.

the decreasing mass accretion rate for larger value of γ. One can see the maximum accretion rate at $r \approx 0.87$ for $\gamma = 0.4$, $r \approx 0.82$ for $\gamma = 0.3$, $r \approx 0.76$ for $\gamma = 0.2$, $r \approx 0.69$ for $\gamma = 0.1$. While, the mass decreases but the radius increases in this case between the universal and Killing horizon. The red curve in a right graph depicts the maximum mass accretion rate between the universal and Killing horizon for Schwarzschild de-Sitter BH. It is noted here that the accretion rate decreases for smaller values of k and we can see the maximum accretion rate near $r \approx 0.69, 0.82, 0.92, 1.0$ for $k = -1.0, -1.5, -2.0, -2.5$, respectively. Now, the maximum mass accretion rate of Schwarzschild BH occurs in bottom panel for smaller radius between the universal and Killing horizons (see red curve). The maximum accretion rate occurs between $r \approx 0.2$ to $r \approx 0.4$. While, the minimum accretion rate occurs at the killing horizon in a bottom panel. Therefore, the minimum mass rate is between $r \approx 0.2$ to $r \approx 1.0$ for the larger value of $\beta = 4.0$. Four key points are observed for the Schwarzschild BH:

- $\beta = 1.0$, corresponding to $r_{UH} \approx 0.22$, $r_{KH} \approx 0.40$.
- $\beta = 2.0$, corresponding to $r_{UH} \approx 0.21$, $r_{KH} \approx 0.60$.
- $\beta = 3.0$, corresponding to $r_{UH} \approx 0.19$, $r_{KH} \approx 0.80$.
- $\beta = 4.0$, corresponding to $r_{UH} \approx 0.18$, $r_{KH} \approx 1.0$.

The mass accretion rate of Schwarzschild BH decreases with the increases of radius for the various values of the mass function.

Chapter 4

Circular Orbits and Accretion Process Near a Regular Phantom Black Hole

The relativistic accretion onto astrophysical compact objects such as BHs and neutron stars is the natural phenomena for releasing energy, with up to 40% of the rest-mass energy of the matter accreting on the BH able to be liberated. High luminosities due to accretion are observed in X-ray binaries, and in active galactic nuclei (AGN). An accretion disks are framed due to development of gases and dust materials that travel in confined orbits by the gravitational force of central massive objects such as main sequence stars, neutron stars, super massive BHs and young stellar objects (YSO). Usually, as the orbits of the particles become unstable an accretion would occur but when the materials orbits are stable there would be no accretion in such systems. The accelerated particles should pass from a critical point and this is the point where the velocity of the fluid exceeds the local speed of sound. In such situation matter falling onto the BH attains a supersonic velocities.

In this chapter, we investigate the geodesics motion and accretion process near a regular phantom BH by taking an isothermal fluid with spherically symmetric BH spacetime. The geodesic motion around BH during accretion provide the disc like structure. Here, we give some reasons for the development of circular orbits and accretion process for the considered BH. Firstly, we discuss the motion of test particles with stabilities near the equatorial plane which make the circular orbit-

s. Then we analyze perturbations via restoring force and oscillations of particles around the central object. Finally, we discuss the critical speed of the fluid flow and maximum accretion rate. The physical validity of our results shows that the phantom parameter b plays an important role for the circular orbits and the maximum accretion rate. The outcomes of this chapter have been published in the form of a research article (Ditta and Abbas 2020).

This chapter is organized as follows: In section **4.1**, we discuss the horizons structure of phantom BH. Section **4.2** is devoted the general formulism for geodesic structure. The circular motion, radiation energy flux and oscillations are inspected in the subsequent sections **4.2.1, 4.2.2** and **4.2.3**, respectively. In section **4.4** and subsection **4.4.1**, we have obtained the dynamical equations and mass expansion. We have investigated the critical accretion, circular equatorial geodesics and epicyclic frequencies in sections **4.5, 4.5.1** and **4.5.2**, respectively.

4.1 Horizons Structure of Phantom Black Hole

From Eq. (2.10), if mass of the BH is negative ($M < 0$), we get a wormhole with the radius condition $r \to -\infty$ which is asymptotic region (anti-de Sitter) and $r \to \infty$ which is also an asymptotic region. When $M = 0$, we obtain an Ellis wormhole, the connection of two symmetric asymptotically flat regions (Zhang and Jing (2018)). In this thesis, we take $M > 0$ and we have a Killing horizon r_H parallel to the single root of $A(r) = 0$. The occurrence of phantom hair in spacetime gets the richer properties. For $0 < b < \frac{3\pi M}{2}$ the range of event horizon r_H is $0 < r_H < 2M$. When $b = \frac{3\pi M}{2}$, we have $r_H = 0$ (event horizon does not exist). When $b > \frac{3\pi M}{2}$, there exist $r_H < 0$ and wormhole appears.

In this respect, the regular phantom solution has the properties of both BHs and wormholes (Bronnikov and Fabris (2006), Eiroa and Sendra (2013)). Likewise, it is manifested that as $0 < b < \frac{3\pi M}{2}$, instead of a singularity, an expanding and asymp-

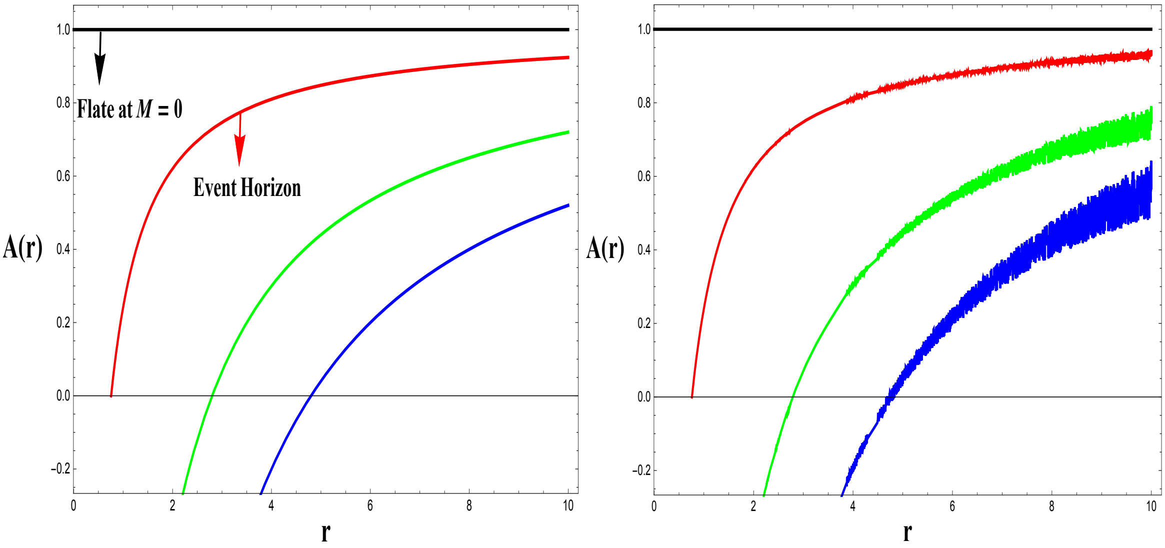

Figure 4.1: Horizon structure of phantom BH, It is a flat for $M = 0$ and has an event horizon for $M = 0.38$. One can see that curves diverge in the right plot when b tends to zero.

totically flat de Sitter- Kantowski-Sachs cosmological appears in its internal region $r_H > r$ (Bronnikov and Fabris (2006), Bolokhov et al. (2012)). This especial kind of the BHs can also be termed as *black Universes*, which have fascinating cosmological behavior in their internal locality (Bronnikov et al. (2007)). When b tends to zero, the phantom scalar ϕ is obtained and it becomes a constant $\frac{\sqrt{2}}{2}\pi$ and the parallel potential $V \to 0$, the action turns to the usual action of GR without any material field and the corresponding BH metric reduces that of the usual Schwarzschild BH Huang et al. (2016).

However, if the parameter b does not involve into the metric function $A(r)$ then the one may study the accretion process without phantom field. Let the reader know how the results of accretion with a phantom field can be compared with accretion without the parameter b. Now, we study the horizon singularity of mentioned phantom BH spacetime, for this, we consider the lapse function

$$A(r) = 0. \tag{4.1}$$

Since, for the radial distance $g_{rr} = 0$ or $A(r) = 0$, one would has an event horizon. The locality of an event horizon in the geometry is a radial distance from the center of the core where the metric is singular, excepting the intrinsic singularity which cannot be detached through coordinate transformation. Figure **4.1** (left plot) has the following key points:

- We have a flat curve (black) when $M = 0$ and $b = 0.10$.
- We have an event horizon curve (red) when $M = 0.38$ and $b = 0.10$.
- While the green and blue curves have no behavior for $M = 1.4, 2.4$ and $b = 0.10$.

Figure **4.1** (right plot) shows that the curves of metric function $A(r)$ diverges when the parameter b tends to zero.

Now using the relation $A(r) = 0$, we have $r_{sing} = \frac{3\pi Mb-2b^2}{12M}$. It is important to note that for evaluations, the suppositions $\arctan\frac{r}{b} = \frac{r}{b}$ and $\frac{r^2}{b^2} \simeq 0$, for larger value of b are considered. Therefore, we have done all calculations using these assumptions also with $M = 1$ and our main focus is to explore the effects of phantom parameter b on the accretion of matter.

4.2 Geodesic Structure: General Formulism

This section provides the study of timelike geodesics near a spacetime by two killing vectors that are $\xi_t = \partial_t$ and $\xi_\phi = \partial_\phi$ corresponding two constants of motion E and L. The constants of motion E and L can be defined by

$$\begin{aligned} E &= -g_{\mu\nu}\xi^{\mu}_{t}u^{\nu} \equiv -u_t, \\ L &= g_{\mu\nu}\xi^{\mu}_{\phi}u^{\nu} \equiv u_\phi, \end{aligned} \tag{4.2}$$

where E and L represent preserved energy and angular momentum, respectively. Also $u^\mu = \frac{dx^\mu}{d\tau} = (u^t, u^r, u^\theta, u^\phi)$ is the four velocity of the fluid and the fluid follows the normalization condition $u^\mu u_\mu = -1$, hence, we get

$$[g_{rr}(u^r)^2 + g_{\theta\theta}(u^\theta)^2] = [-1 - g^{tt}(u_t)^2 - g^{\phi\phi}(u_\phi)^2]. \tag{4.3}$$

In equatorial plane, we put ($\theta = \pi/2$), in Eqs. (4.2) and (4.3), and get

$$\begin{aligned} u^t &= \frac{E}{A(r)}, \qquad (4.4) \\ u^\theta &= 0, \\ u^\phi &= \frac{L}{r^2+b^2}, \\ u^r &= \left[A(r)\left(-1 + \frac{E^2}{A(r)} - \frac{L^2}{r^2+b^2}\right)\right]^{\frac{1}{2}}. \end{aligned}$$

Also the conserved energy equation can be written as

$$(u^r)^2 + V_{eff} = E^2, \tag{4.5}$$

where V_{eff} is an effective potential for the motion of test particle which is given by

$$V_{eff} = A(r)\left[1 + \frac{L^2}{r^2+b^2}\right]. \tag{4.6}$$

We note that effective potential depends on specific angular momentum of particle, the metric parameter $A(r)$ and the radial distribution. For the geodesic motion, the study of effective potential is very helpful such as the local extrema of effective potential can be used to find out the location of circular orbits.

The physical behavior of the left panel of Fig. **4.2** signify the effective potential against the radius r for various values of angular momentum L with the fixed value of phantom parameter $b = 4.80$. We see the first extremum at $L = 5$. The red dot shows the location of innermost stable circular orbits at $r = 3.5$. It is to be noted that V_{eff} has two extremum for large values of L, where the maximum location shows the unstable circular orbits and the minimum shows the stable circular orbits. The V_{eff} increases by increasing L and hence maximum points turn to smaller radii whereas the minimum points go to the larger radii, respectively. The similar behavior can be seen from the right panel of Fig. **4.2**, the effective potential goes to the larger values as phantom parameter b increases.

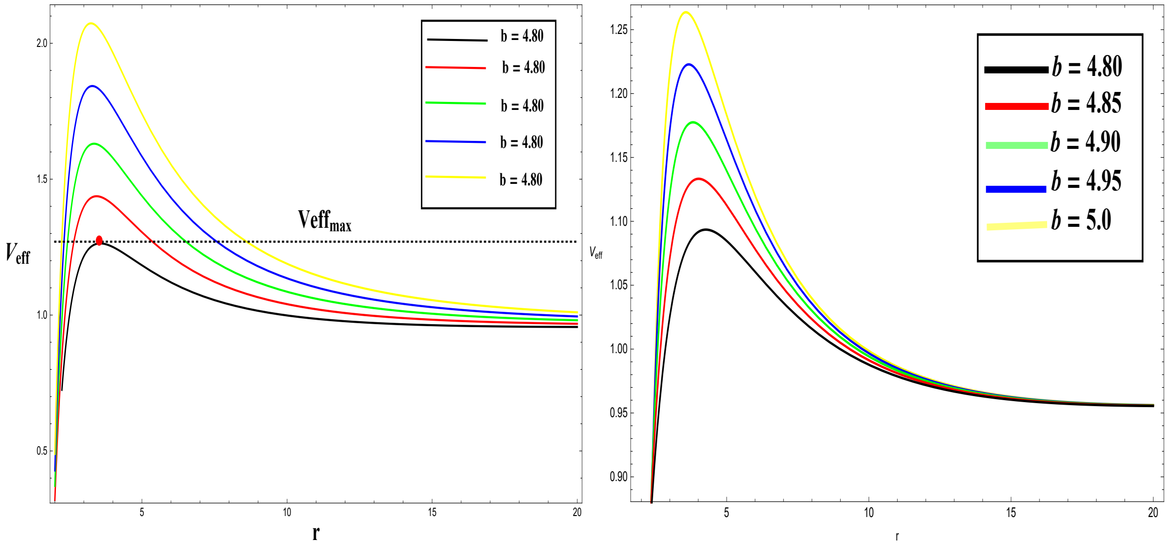

Figure 4.2: Equation (4.35) which is governing from Eq. (4.6), shows the effective potential behavior (left and right panels) near radial coordinate of BH. The left panel is for $b = 4.80$ and with different values of angular momentum. The right panel represents the effect of the phantom parameter b on effective potential with $L = 5$. Note: It is interesting that the results are well matched to Salahshoor and Nozari (2018), thus the stable circular orbits are at the minimum of V_eff.

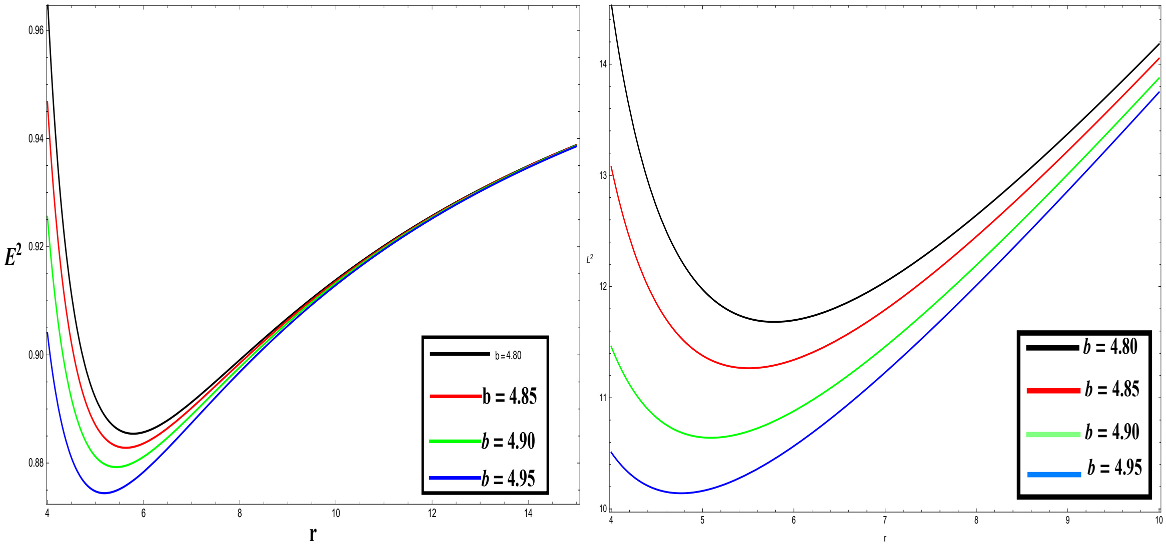

Figure 4.3: Equations (4.40) and (4.41) plot the system of figures (left and right panels) for energy and angular momentum with radial coordinate from the central mass for different values of the phantom parameter b.

4.2.1 Circular Motions

In the equatorial plane, we have radial component of velocity as constant, so $\dot{u}^r = 0$ must hold. Using this in Eq. (4.5), we get $V_{eff} = E^2$ and so $\frac{d(V_{eff})}{dr} = 0$. With these relations, we can determine E, L, Ω_ϕ, l, the specific energy, specific angular momentum, angular velocity and angular momentum, respectively as follows

$$E^2 = \frac{2rA^2(r)}{2rA(r) - (r^2+b^2)A'(r)}, \tag{4.7}$$

$$L^2 = \frac{(r^2+b^2)^2 A'(r)}{2rA(r) - (r^2+b^2)A'(r)}, \tag{4.8}$$

$$\Omega_\phi = \frac{d\phi}{dt} \equiv \frac{u^\phi}{u^t} \Rightarrow \Omega_\phi^2 = \frac{1}{2r}A'(r), \tag{4.9}$$

$$l^2 = \frac{L^2}{E^2} = \frac{(r^2+b^2)^2}{2rA^2(r)}A'(r). \tag{4.10}$$

We have plotted the physical behavior of the angular momentum and specific energy against the dimensionless radius r and the phantom parameter b in Fig.

4.3. In the left panel, the solution curves show the variation of specific energy against radius with different colors. The solid circles in the right panel show the position of this radius with innermost stable circular orbits. The energy raises by increasing b. The reverse behavior is shown for angular momentum, the solution curves decreases by increasing b in left panel. In right panel, the circles represent the behavior of the loci of these variables in the innermost stable circular orbits.

For the real values of specific energy and angular momentum, the following relation must hold

$$2rA(r) - (r^2 + b^2)A'(r) > 0. \tag{4.11}$$

Also the restricted area of the circular orbits can be calculated by solving the above inequality. The condition $E^2 < 1$ is valid only for bound orbits but for marginally bound orbits the condition $E^2 = 1$ must be satisfied. From Eq. (4.7), we have

$$(r^2 + b^2)A'(r) + 2rA(r)[A(r) - 1] = 0. \tag{4.12}$$

By solving the above equation, we obtain the marginally bound orbits. Now, from Eqs. (4.7) and (4.8), we get the following condition

$$2rA(r) - (r^2 + b^2)A'(r) = 0. \tag{4.13}$$

One can obtained the radius of photon sphere by solving the Eq. (4.13).

4.2.2 Radiation Energy Flux

The stable circular orbits exist, when the local minima of the effective potential $\frac{d^2}{dr^2}V_{eff} > 0$, whereas for marginally stable circular orbits r_{isco} the relation $\frac{d^2}{dr^2}V_{eff} = 0$, must be hold. Now, from Eq. (4.6), we have

$$\begin{aligned}\frac{d^2V_{eff}}{dr^2} = \quad & A''(r)\left(1 + \frac{L^2}{r^2+b^2}\right) - 4rA'(r)\frac{L^2}{(r^2+b^2)^2} \\ & -2(-3r^2+b^2)A(r)\frac{L^2}{(r^2+b^2)^3}.\end{aligned} \tag{4.14}$$

An accretion process is imaginable if $r < r_{isco}$. If the particles accrete onto the BH from rest to infinity, then they released the gravitational energy after that this energy can be converted into the radiations and these radiations are the foundation of the most energetic astrophysical phenomena. The radiant energy flux above the disk expressed by Kato et al. (2008) under the specific energy E, angular momentum L and the angular velocity Ω_{ϕ}. We have

$$K = -\frac{\dot{M}\Omega_{\phi,r}}{4\pi\sqrt{-g}(E - L\Omega_{\phi})^2}\int (E - L\Omega_{\phi})L_{,r}dr, \tag{4.15}$$

where K is radiation flux, $\Omega_{\phi,r} = \frac{d\Omega_{\phi}}{dr}$, $\dot{M}$ is accretion rate and g is determinant of the metric, which is given by

$$g = det(g_{\mu\nu}) = -(r^2 + b^2)^2 \sin^2\theta. \tag{4.16}$$

As we restrict we our study in equatorial plane, so we use $\sin\theta = 1$. Thus, from Eqs. (4.7)-(4.9), we get

$$\begin{aligned} K(r) = \quad & -\frac{\dot{M}}{4\pi}\frac{rA''(r) - A'(r)}{\sqrt{2}r^2(r^2 + b^2)\sqrt{\frac{A'(r)}{r}}} \\ & \times\left(-2\sqrt{\frac{rA^2(r)}{2rA(r) - (r^2 + b^2)A'(r)} + \sqrt{\frac{A'(r)}{r}}\sqrt{\frac{(r^2 + b^2)A'(r)}{2rA(r) - (r^2 + b^2)A'(r)}}}\right)^{-2} \\ & \times\int_{mb}^{r} F(r)dr, \end{aligned} \tag{4.17}$$

where

$$\begin{aligned} F(r) = \quad & \sqrt{\frac{A(r)}{2r(r^2 + b^2)}} \\ & \times\frac{\left[4rA'(r) + (r^2 + b^2)A''(r) - (r^2 + b^2)A'(r)(2A(r) - A''(r))\right]}{2rA(r) - (r^2 + b^2)A'(r)}. \end{aligned} \tag{4.18}$$

Now, we consider the important relation between the radiation flux and the temperature, which is given by $K(r) = \sigma T^4(r)$.

4.2.3 Oscillations

Now, we explain radial motion with $\frac{1}{2}\left(\frac{dr}{dt}\right)^2 = V^{(r)}_{eff}$ and vertical motion with $\frac{1}{2}\left(\frac{d\theta}{dt}\right)^2 = V^{(\theta)}_{eff}$. From Eq. (4.3), we set $u^\theta = 0$ and for vertical motion $u^r = 0$. By taking $u^r = \frac{dr}{d\tau} = \frac{dr}{dt}u^t$ and $u^\theta = \frac{d\theta}{d\tau} = \frac{d\theta}{dt}u^t$, we obtain

$$\begin{aligned}\frac{1}{2}\left(\frac{dr}{dt}\right)^2 &= -\frac{1}{2}\frac{A^3(r)}{E^2}\left[1+\frac{E^2}{A(r)}+\frac{L^2}{(r^2+b^2)\sin^2\theta}\right] = V^{(r)}_{eff}. \quad (4.19)\\ \frac{1}{2}\left(\frac{d\theta}{dt}\right)^2 &= -\frac{1}{2}\frac{A^2}{(r^2+b^2)E^2}\left[1+\frac{E^2}{A(r)}+\frac{L^2}{(r^2+b^2)\sin^2\theta}\right] = V^{(\theta)}_{eff}.\end{aligned}$$

The perturbations δr and $\delta\theta$ are required for the radial and vertical epicyclic frequencies near the circular orbit in equatorial plane. We take the time derivative of radial Eq. (4.19), and get

$$\frac{d^2r}{dt^2} = \frac{dV^{(r)}_{eff}}{dr}. \quad (4.20)$$

For small deviation $\delta r = r - r_0$, the equation of motion is written as

$$\frac{d^2(\delta r)}{dt^2} = \frac{dV^{(r)}_{eff}}{dr}(\delta r) \Rightarrow (\delta\ddot{r}) + \Omega_r^2(\delta r) = 0, \quad (4.21)$$

where a double dots denote the derivative with respect to time coordinate t and $\Omega^2(r) = -\frac{d^2}{d\theta^2}V^{(r)}_{eff}$. Also, by the same procedure for vertical direction with deviation $\delta\theta = \theta - \theta_0$, we get

$$\frac{d^2(\delta\theta)}{dt^2} = \frac{dV^{(\theta)}_{eff}}{dr}(\delta\theta) \Rightarrow (\delta\ddot{\theta}) + \Omega_\theta^2(\delta\theta) = 0, \quad (4.22)$$

where $\Omega^2(\theta) = -\frac{d^2}{d\theta^2}V^{(\theta)}_{eff}$. From Eq. (4.19) in an equatorial plane, we get the following components

$$\Omega_\theta^2 = \frac{h^2(r)L^2}{(r^2+b^2)^2E^2}, \quad (4.23)$$

and

$$\begin{aligned}\Omega_r^2 = \quad & \frac{1}{2(r^2+b^2)^3E^2}\Big[(r^2+b^2)^2(2(r^2+b^2)E^2+3(r^2+b^2+L^2)A^2(r))\Big]A''(r) \\ & +2(r^2+b^2)\Big[(r^2+b^2)^2E^2A'(r)+3(r^2+b^2)(r^2+b^2+L^2)A(r)-6L^2rA^2(r)\Big]A'(r) \\ & -2L^2(b^2-3r^2)A^3(r).\end{aligned} \tag{4.24}$$

Now, we consider some basic dynamical properties in a regular phantom BH, so that we can proceed further.

4.3 Dynamical Parameters

From Eq. (2.34), we get the radial velocity $u(r)$ by the help of EoS $p = k\rho$, which is given by

$$u(r) = \left(\frac{1}{k+1}\right)\sqrt{\frac{(N_4)^2}{A(r)} - (k+1)^2}, \tag{4.25}$$

which gives

$$u(r) = \left(\frac{1}{k+1}\right)\sqrt{\frac{(N_4)^2}{1-\frac{3M}{b}\left[\left(\frac{\pi}{2}-\arctan\frac{r}{b}\right)\left(1+\frac{r^2}{b^2}\right)-\frac{r}{b}\right]} - (k+1)^2}. \tag{4.26}$$

From Eq. (2.33), we get the energy density $\rho(r)$ with the help of radial velocity, which is given by

$$\rho(r) = \frac{N_3}{(r^2+b^2)}\frac{(k+1)}{\sqrt{\frac{(N_4)^2}{A(r)} - (k+1)^2}}, \tag{4.27}$$

which gives

$$\rho(r) = \frac{N_3}{(r^2+b^2)}\frac{(k+1)}{\sqrt{\frac{(N_4)^2}{1-\frac{3M}{b}\left[\left(\frac{\pi}{2}-\arctan\frac{r}{b}\right)\left(1+\frac{r^2}{b^2}\right)-\frac{r}{b}\right]} - (k+1)^2}}. \tag{4.28}$$

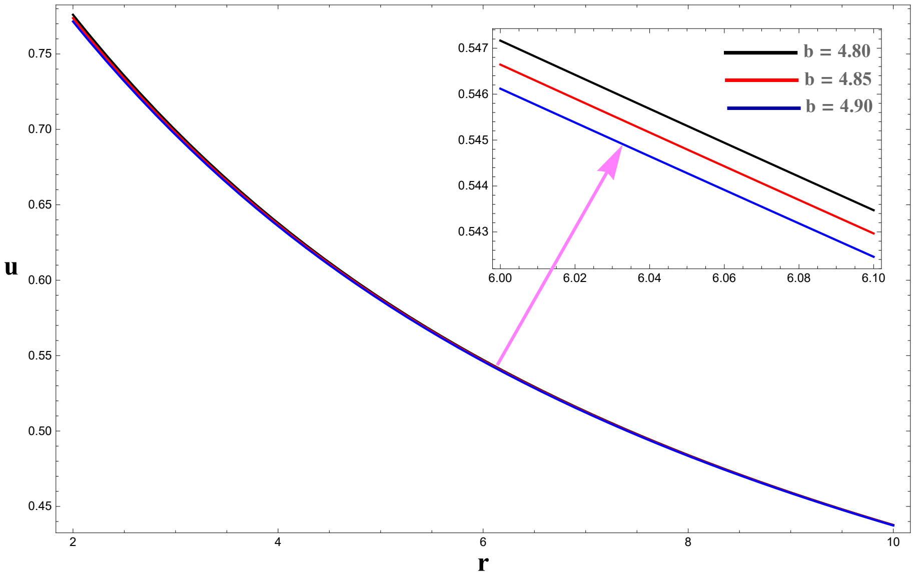

Figure 4.4: The profile of the radial velocity Eq. (4.26) shows that the solution curves are very close to each other and we draw their structure which can be seen explicitly, it is the function of r with EoS parameter $k = 1/2$ and constant of integration $N_4 = 1.5$.

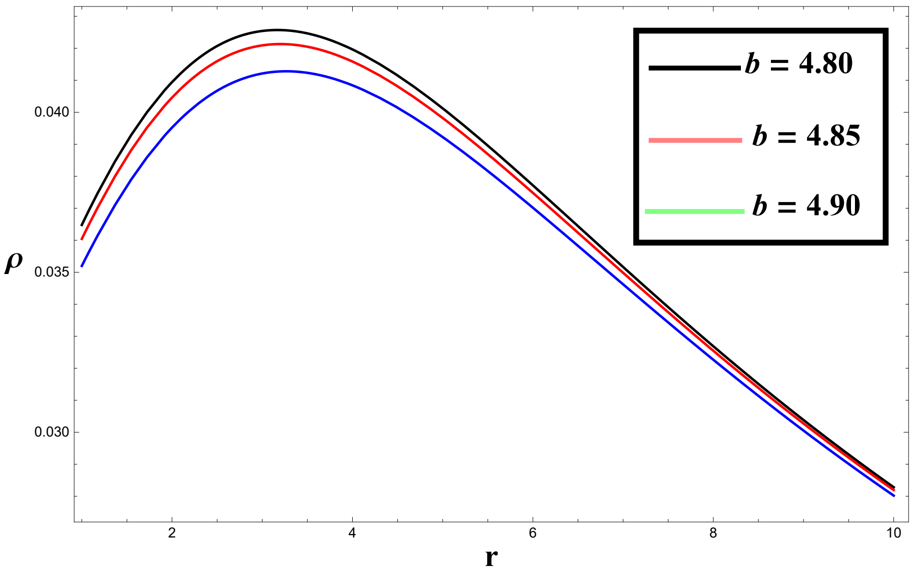

Figure 4.5: The profile of the density Eq. (4.28) shows that the solution curves are gradually increases by increasing b, it is the function of r with EoS parameter $k = 1/2$ and constant of integrations $N_3 = 1$, $N_4 = 1.5$.

4.3.1 Mass Evolution

By accretion of mass onto the BH and due to Hawking radiation, its mass is changed step by step. The accretion of mass can be attained by integrating the flux of the fluid over the surface of BH and generally it is denoted by $\dot{M}$. The expression for $\dot{M}$ is given by

$$\dot{M} = -4\pi(r^2 + b^2)u^r(\rho + p)\sqrt{A(r) + (u^r)^2} \equiv -4\pi N_0, \tag{4.29}$$

where $N_0 = -N_1 N_2$ and $N_2 = (p_\infty + \rho\infty)\sqrt{A(r_\infty)}$ yields

$$\dot{M} = 4\pi N_1(\rho_\infty + p_\infty)\sqrt{A(r_\infty)}M^2. \tag{4.30}$$

Now, we find the time evolution of mass of BH, for this we write Eq. (4.30), as

$$\frac{dM}{M^2} = \mathcal{F}dt, \tag{4.31}$$

where $\mathcal{F} = 4\pi N_1(\rho_\infty + p_\infty)\sqrt{A(r_\infty)}$, the integration of above equation leads to

$$M_t = \frac{M_i}{1 - FtM_i} \equiv \frac{M_i}{1 - \frac{t}{t_{cr}}}, \tag{4.32}$$

where $t_{cr} = \left[4\pi N_1(\rho_\infty + p_\infty)\sqrt{A(r_\infty)M_i}\right]^{-1}$ is the critical accretion time evolution. The accretion is a perturbative process in this analysis since the back reaction on the metric is not included. In the case $t = t_{cr}$, the denominator of Eq. (4.32) vanishes and the BH mass grows up to infinity in a finite time. Consequently, Eq. (4.32) for the time rate of change of mass $\dot{M}$ can not be viewed as exact, but indicative of the non-perturbative solution.

The shapes of velocity, density and accretion rate have been plotted in Figs.**4.4-4.6** against the r, with various values of phantom parameter b, the equation of state parameter $k = 1/2$ and fixed values of constants of integration $N_4 = 1.5$ and $N_3 = 1$. Since far from the BH, the fluid flow is subsonic and it has a zero radial velocity before passing through the critical points. When fluid passes through the

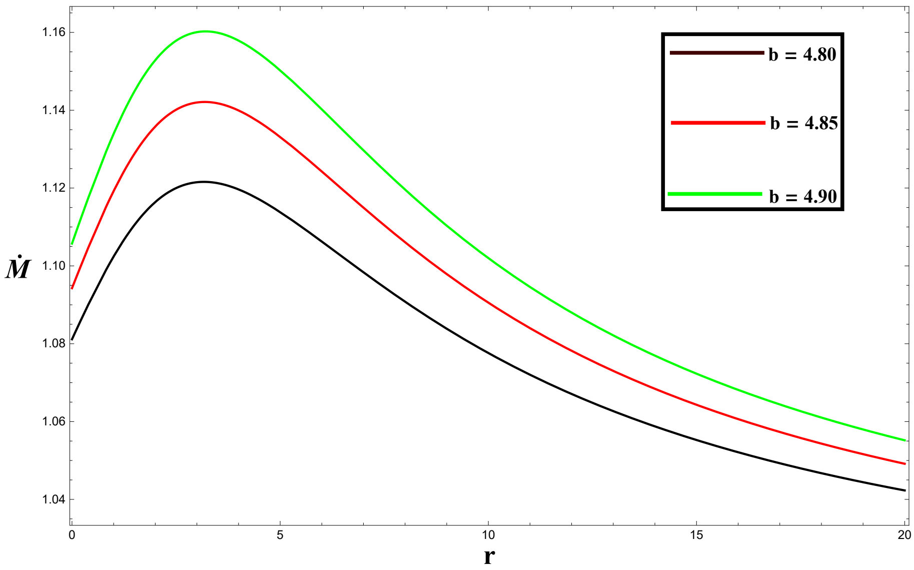

Figure 4.6: Accretion rate of phantom BH for EoS parameter $k = 1/2$ shows with three solution curves black, red and green. The mass accretion rate gradually increases from black to green versus the radial parameter. The other constants are taken as $N_3 = 1$ and $N_4 = 1.5$.

critical point in the locality of BH, then speed of flow increases and goes up to the supersonic flow due to strong gravity. In Fig. **4.4** the velocity is reduces by increasing b. Therefore, near the BH the speed of dropping particles become equal to the sound speed.

The energy density of the matter over the BH for several values of b is displayed in Fig.**4.5**. The plot shows that by growing the values of b, the density grows. The mass of BH deviates with time for the isothermal fluids. It has been observed that the accretion rate is higher in the locality of BH due to the gravitational effect in Fig.**4.6**. On increasing the values of phantom parameter b, we get the higher mass accretion rate.

4.4 Critical Accretion

It has been observed that the fluid is at rest far from the BH, but it accelerates inward due to the gravitational field of BH. As fluid accretes then it must passed from the critical point and this is the point where the velocity of the fluid becomes equal to the sound speed. Therefore, the maximum accretion rate occurs at critical point. When $h = h(\rho)$ is constant enthalpy, then the fluid becomes barotropic.

Now, we find the critical velocities at the critical points, from Eqs. (2.39) and (2.40), we get

$$(u_c)^2 = \frac{1}{4r}(r^2 + b^2)_c A'_{rc}. \tag{4.33}$$

and

$$V_c^2 = \frac{(r^2 + b^2)_c A'_{rc}}{(r^2 + b^2)_c A'_{r_c} + 4rA(r_c)}. \tag{4.34}$$

where V_c, r_c, u_c represent the values for local speed of sound, the distance of fluid from the central mass and the velocity of fluid at critical point, respectively.

4.4.1 Circular Equatorial Geodesic

In the structure of circular geodesics, we take the explicit form of the effective potential given by Eq. (4.6) as follows

$$V_{eff} = \left(1 - \frac{3M}{b}\left[\left(\frac{\pi}{2} - \arctan\frac{r}{b}\right)\left(1 + \frac{r^2}{b^2}\right) - \frac{r}{b}\right]\right)\left(1 + \frac{L^2}{r^2 + b^2}\right), \tag{4.35}$$

where from the condition $\frac{d^2}{dr^2}V_{eff} > 0$, we can see the presence of the innermost stable circular orbits and also Eq. (4.14) locate the innermost stable circular orbits at

$$r_{isco} = \frac{3\pi Mb - 2b^2}{4M}, \tag{4.36}$$

which denotes the required innermost stable circular orbits radius in equatorial plane.

Using Eq. (4.13), we get photon sphere, circular orbit and marginally bound orbit radii r_{ph}, r_{circ} and r_{mb}, respectively as follows

$$r_{ph} = \frac{3\pi Mb - 2b^2}{6M}, \tag{4.37}$$

$$r_{circ} > \frac{3\pi Mb - 2b^2}{6M}, \tag{4.38}$$

$$r_{mb} = \frac{-3b^2 + 6bM\pi \pm \sqrt{3}\sqrt{3b^4 - 4b^3M\pi}}{24M}. \tag{4.39}$$

Figure **4.7** shows the radius of circular orbits versus the phantom parameter b. The location of these orbits depend on the parameter b in the locality of the BH. The location of these orbits r_{sing}, r_{ph}, r_{mb} and r_{isco} increases step by step and will be close to BH for larger of b. The circular orbits representing the disk will be stretched close to the BH, by increasing b.

Now, we are going to derive the specific-energy, angular velocity, angular momentum and specific angular momentum in equatorial plane. These results are

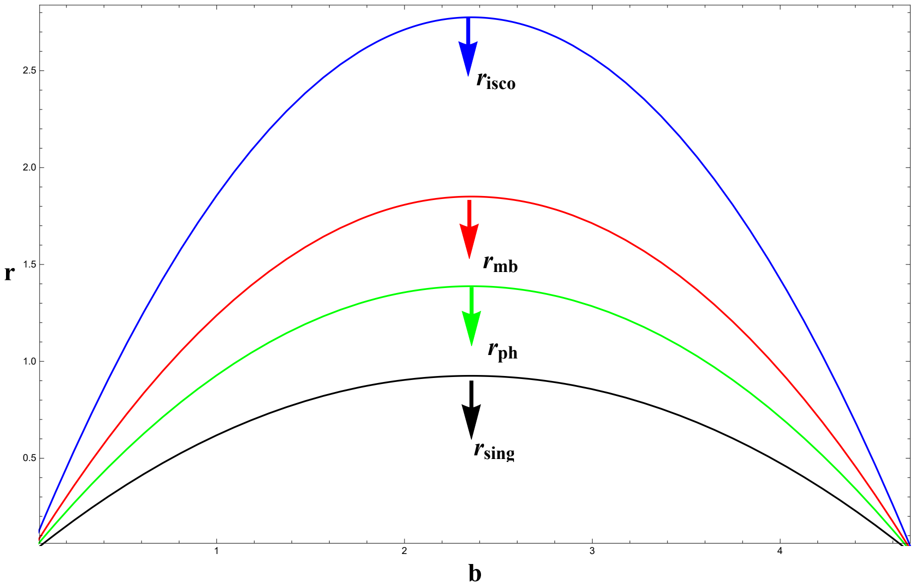

Figure 4.7: The system of Eqs. (4.36)-(4.39) represent the effective behavior of the phantom parameter b on the radius r and the relationship between the characteristic radii. Four solution curves with different colors indicate that $r_{sing} < r_{ph} < r_{mb} < r_{isco}$.

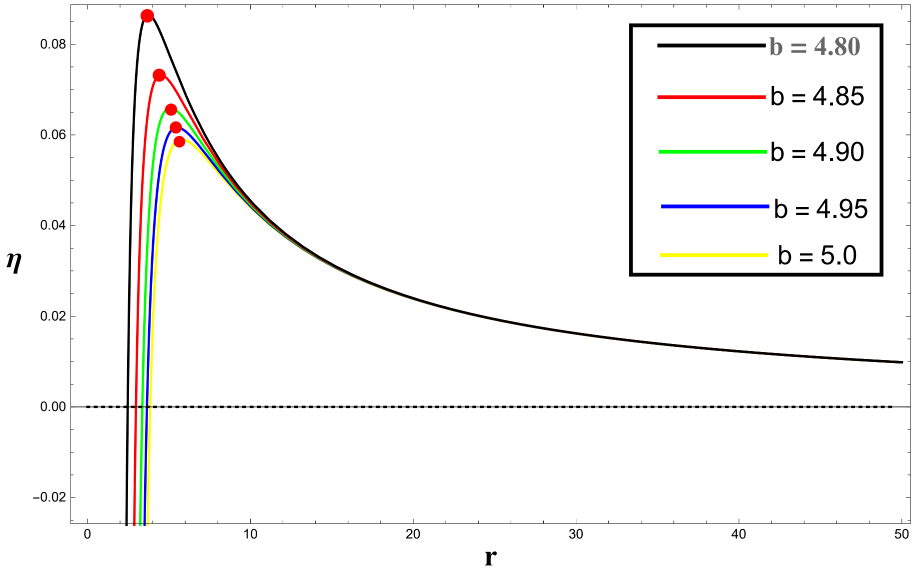

Figure 4.8: Depicts the energy efficiency behavior of the massive particles which are falling from infinity into the BH against the radial distance r for suitable variation of the phantom parameter b. Red dots show the maximum efficiency.

obtained for a moving particle in circular orbits. Here,

$$E^2 = \frac{2r\left(1 - \frac{3M}{b}\left[\left(\frac{\pi}{2} - \arctan\frac{r}{b}\right)\left(1 + \frac{r^2}{b^2}\right) - \frac{r}{b}\right]\right)^2}{2(r-3M)}. \tag{4.40}$$

$$L^2 = \frac{(r^2+b^2)^2\left(3M(2b - \pi r + 2r\arctan\frac{r}{b})\right)}{2b^3(r-3M)}. \tag{4.41}$$

$$\Omega_\phi^2 = \frac{3M(2b - \pi r + 2r\arctan\frac{r}{b})}{2r}. \tag{4.42}$$

$$l^2 = \frac{(r^2+b^2)^2\left(3M(2b - \pi r + 2r\arctan\frac{r}{b})\right)}{2r\left(1 - \frac{3M}{b}\left[\left(\frac{\pi}{2} - \arctan\frac{r}{b}\right)\left(1 + \frac{r^2}{b^2}\right) - \frac{r}{b}\right]\right)^2}. \tag{4.43}$$

The energy efficiency of accretion is defined as $\eta = 1 - E$, whereas the maximum efficiency of an accretion is $\eta^* = 1 - E_{isco}$. In Fig. **4.8**, the plotted curves represent the energy efficiency versus radius for different values of b. This graph shows that the energy efficiency decreases by increasing b and red solid dots show the maximum efficiency. For larger value of b the last yellow curve gives the value of efficiency at 0.057.

After evaluating E, L and Ω_ϕ, we are able to discuss the radiation flux on the surface of accretion disk. From Eqs. (4.17) and (4.18), we obtain the radiation flux as follows

$$\begin{aligned} K(r) = \quad & \frac{-2\sqrt{6}}{r^2(r^2+b^2)^2\sqrt{\frac{M(2b-\pi r+2r\Delta)}{b^3 r}}} \\ & \times\Big(\sqrt{\frac{r(2b^3+6bMr-3b^2M(\pi-2\Delta)-3Mr^2(\pi-2\Delta))^2}{b^6-3Mr}} \\ & -3\sqrt{\frac{M(2b-\pi r+2r\Delta)}{b^3 r}}\sqrt{\frac{M(r^2+b^2)^2(2b-\pi r+2r\Delta)}{b^3(-3M+r)}}\Big)^{-2}\int_{mb}^{r} F(r)dr, \end{aligned} \tag{4.44}$$

where

$$\begin{aligned} F(r) = \quad & \Big(\sqrt{\frac{3}{2}}M(r^2+b^2)(2b^3+2b(15M-4r)r-3b^3M(\pi-2\Delta)-(15M-4r)r^2) \\ & -\sqrt{\frac{r(2b^3+6bMr-3b^2M(\pi-2\Delta)-3Mr^2(\pi-2\Delta))^2}{b^6(3M-r)}}\sqrt{\frac{(M(r^2+b^2)(2b-\pi r+2r\Delta)}{b^3(3M-r)}}\Big) \\ & \times\Big(\frac{M(r^2+b^2)(2b-\pi r+2r\Delta)}{b^3(3M-r)}\Big)^{-1/2}. \end{aligned} \tag{4.45}$$

The temperature profile can be explained by using the formula $K = \sigma T^4$. The comparison between radiation flux and temperature T is shown in Fig. **4.9**. The solution curves show the radiation flux goes to the maximum in the locality of BH and it goes down for increasing the phantom parameter b at the smaller radii.

4.4.2 Epicyclic Frequencies

Now, we see the effect of perturbation on a moving fluid , the fluid attains a small oscillations in the direction of radial and vertical frequencies. We can derive these frequencies as

$$\Omega_\theta^2 = \frac{r^3\Big(3M(2b-\pi r+2r\Delta)\Big)}{2b^3(r^2+b^2)^2}, \tag{4.46}$$

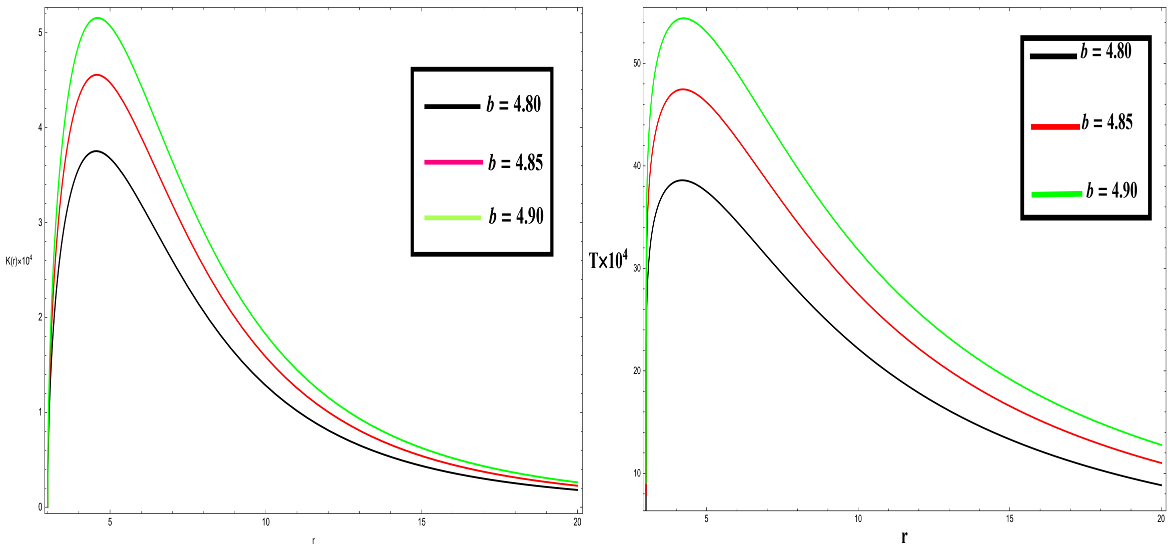

Figure 4.9: The physical behavior (left and right panels) show the emission rate and temperature T for different values of phantom parameter b. The green curve depicts the maximum emission rate as well as temperature.

whereas the result of radial epicyclic frequency is so lengthy, therefore we can see its physical behavior from Fig. **4.10**.

Both the left and right panels of Fig.**4.10** characterize the epicyclic frequencies with the radius r for different values of the phantom parameter b. We can see explicitly the green, red and blue curves coincide and these increase by increasing b and shifts to the smaller radii.

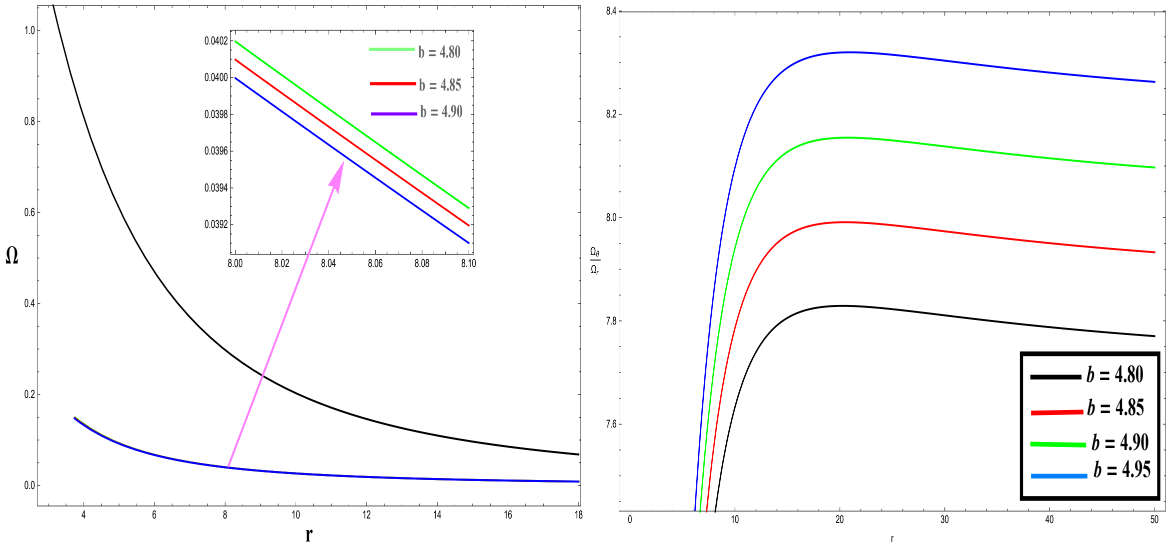

Figure 4.10: The system of figures (left and right panels) showing the relationship between epicyclic frequencies. Black solution curve signify vertical frequency whereas the blue, red and green solution curves indicate the radial frequency for several values of phantom parameter b in the left panel. The right panel of the system denotes the ratio of these two frequencies.

Chapter 5

Relativistic Accretion Mechanism for Some Black Holes

In this chapter, we have adopted the Michel's approach to discuss the accretion onto regular phantom and $4D$ Einstein-power-Maxwell BHs. For these BHs, we have formulated the expressions for the radial velocity u, energy density ρ, speed of sound ${c^2}_s$ and mass accretion rate $\dot{M}$. We have discussed the physical behavior of the radial velocity and energy density and mass accretion rate graphically. It has been found that mass accretion rate increases for the cases of dust, stiff fluid and quintessence, while it decreases for the phantom fluid. The results of this chapter have been published in the form of a research article (Ditta and Abbas 2020).

The arrangement of this chapter is as follows: The equations for the relativistic accretion, density, speed of sound and the critical accretion rate for phantom and $4D$ Einstein-power-Maxwell BHs are given in sections **5.1** and **5.2**, respectively.

5.1 Critical Accretion onto Phantom Black Hole

In this section, our focus is to study the the critical velocity, energy density, sound speed and the rate of change of mass of the accreting body.

The action and the metric of phantom BH have already been discussed in Eqs.

(2.3) and (2.9), again we consider

$$\begin{aligned} A(r) &= B(r) = 1 - \frac{3M}{b}\left[\left(\frac{\pi}{2} - \arctan\frac{r}{b}\right)\left(1 + \frac{r^2}{b^2}\right) - \frac{r}{b}\right], \\ C(r) &= r^2 + b^2, \end{aligned} \tag{5.1}$$

Now, from Eq. (2.34), we get the radial velocity $u(r)$ with the help of EoS $p = k\varrho$, as follows

$$u(r) = \left(\frac{1}{k+1}\right)\sqrt{\frac{(N_4)^2}{1 - \frac{3M}{b}\left[\left(\frac{\pi}{2} - \arctan\frac{r}{b}\right)\left(1 + \frac{r^2}{b^2}\right) - \frac{r}{b}\right]} - (k+1)^2}. \tag{5.2}$$

From Eq. (2.33), we get the energy density $\varrho(r)$ with the help of radial velocity, which is given by

$$\varrho(r) = \frac{N_3}{(r^2 + b^2)} \frac{(k+1)}{\sqrt{\frac{(N_4)^2}{1 - \frac{3M}{b}\left[\left(\frac{\pi}{2} - \arctan\frac{r}{b}\right)\left(1 + \frac{r^2}{b^2}\right) - \frac{r}{b}\right]} - (k+1)^2}}. \tag{5.3}$$

We have plotted the graphs of above relations (6.8) and (6.10) for the accretion process with different kinds of fluids. Figure **5.1** signifies the velocity contour for different values of k and we see that the behavior of this plot is different from previous study by Bahamonde and Jamil (2015). For a phantom black hole, we have taken the positive values of the state parameter k. These values are 1, $1/2$, $1/3$ and $1/4$ for stiff, relativistic, radiation and sub-relativistic fluids, respectively. The black, red, green and blue curves depict the negative velocity, whereas the upper half of the solution curves represent the positive velocity of the fluid for the same values of k. The energy density contour of the fluid around the phantom BH is plotted in Fig. **5.1**. It can be seen that the energy density increases for all cases except for $k = -1.5$ and $k = -2$. For these cases the energy density decreases as it approaches the event horizon.

Due to the accretion process, the rate of change of mass of the regular phantom BH is obtained from Eq. (2.94), which is given by

$$\dot{M} = \frac{4\pi L_0^2 M^2 (k+1)}{(r^2 + b^2)\sqrt{-A(r)(k+1)^2 + L_1^2}}, \tag{5.4}$$

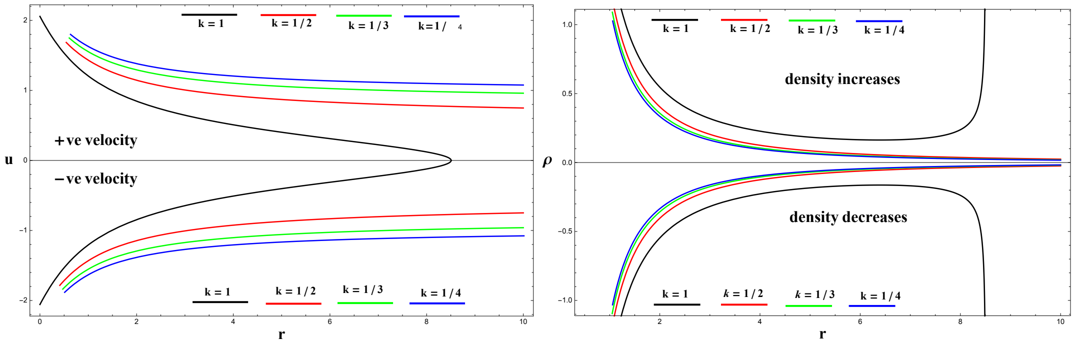

Figure 5.1: Velocity and energy graphs versus the radius r for $b = 1.055$ and $M = 2$, with different values of the state parameter k.

which further simplifies to

$$\dot{M} = \frac{4\pi L_0^2 M^2 (k+1)}{(r^2+b^2)\sqrt{-\left(1-\frac{3M}{b}\left[\left(\frac{\pi}{2}-\arctan\frac{r}{b}\right)\left(1+\frac{r^2}{b^2}\right)-\frac{r}{b}\right]\right)(k+1)^2+L_1^2}}. \tag{5.5}$$

Figure **5.2** explains the rate of change of mass of phantom BH for different values of k. We have noted that the mass of the regular phantom BH increases in case of quintessence, dust and stiff fluid and it decreases for phantom case with $k < -1$. If phantom dark energy falls on phantom BH, the mass accretion rate is decreased.

5.2 Einstein Power-Maxwell 4D Black Hole

In this section, we have discussed the accretion process onto $4D$ EPM BH for isotropic fluid. From (2.14), one can find the horizons of EPM $4D$ BH, by putting $A(r) = 0$, and it can be factorized as $A(r) = 1 - \frac{\mu}{r} + \frac{q}{r^3} = \frac{(r-r_i)(r-r_h)(r-r_0)}{r^3}$, where r_h and r_i represent the event and inner horizons, respectively and obey the condition $r_i < r_h$. The parametrization of charge as well as mass of the BH near the horizons is as follows $\mu = r_i + \frac{r_h^2}{r_i+r_h}$, and $q = \frac{r_i^2 r_h^2}{r_i+r_h}$.

For $4D$ EPM BH, Grigoris (2019) has considered $\mu = 2$ and $q_{max} = 1.185$. But, in our case, we have chosen $\mu = 2$ and $q_{max} = 1.055$, for the physical analysis of the

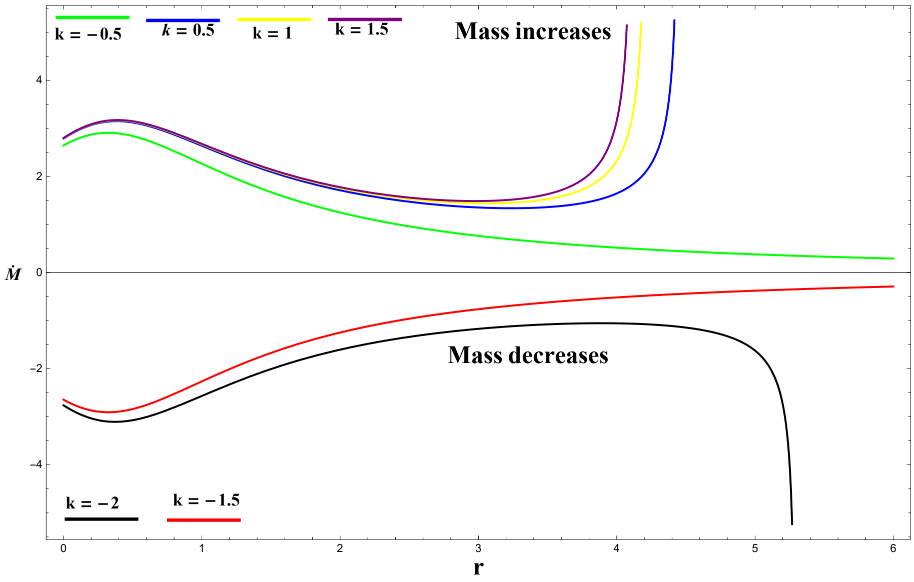

Figure 5.2: Rate of change of BH mass versus the radius r for $b = 1.055$ and $M = 2$, with different values of k. Upper half of the graph represents the mass increases while the lower half shows decrease in mass.

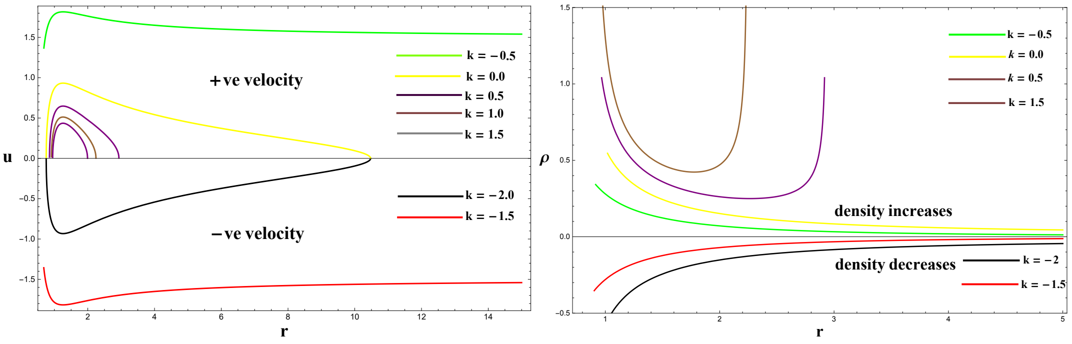

Figure 5.3: Velocity and energy graphs versus radius r for $q = 1.055$ and $M = 2$, with different values of the state parameter k.

result.

From Eq. (2.34) and equation of state $p = k\varrho$, we get the radial velocity $u(r)$, which is given by

$$u(r) = \left(\frac{1}{k+1}\right)\sqrt{\frac{(N_4)^2}{A(r)} - (k+1)^2}, \tag{5.6}$$

which further simplifies to

$$u(r) = \left(\frac{1}{k+1}\right)\sqrt{\frac{(N_4)^2}{1 - \frac{\mu}{r} + \frac{q}{r^3}} - (k+1)^2}. \tag{5.7}$$

From Eq. (2.33), we get the energy density $\varrho(r)$, which is given by

$$\varrho(r) = \frac{N_3}{(r^2+b^2)} \frac{(k+1)}{\sqrt{\frac{(N_4)^2}{A(r)} - (k+1)^2}}, \tag{5.8}$$

which further simplifies to

$$\varrho(r) = \frac{N_3}{(r^2+b^2)} \frac{(k+1)}{\sqrt{\frac{(N_4)^2}{1-\frac{\mu}{r}+\frac{q}{r^3}} - (k+1)^2}}. \tag{5.9}$$

We have plotted the graphs of above expressions (6.8) and (6.10) for the accretion of different kinds of fluids. Figure **5.3** signifies the velocity contour for different values of k and it has been noted that the velocity behavior is same as given in

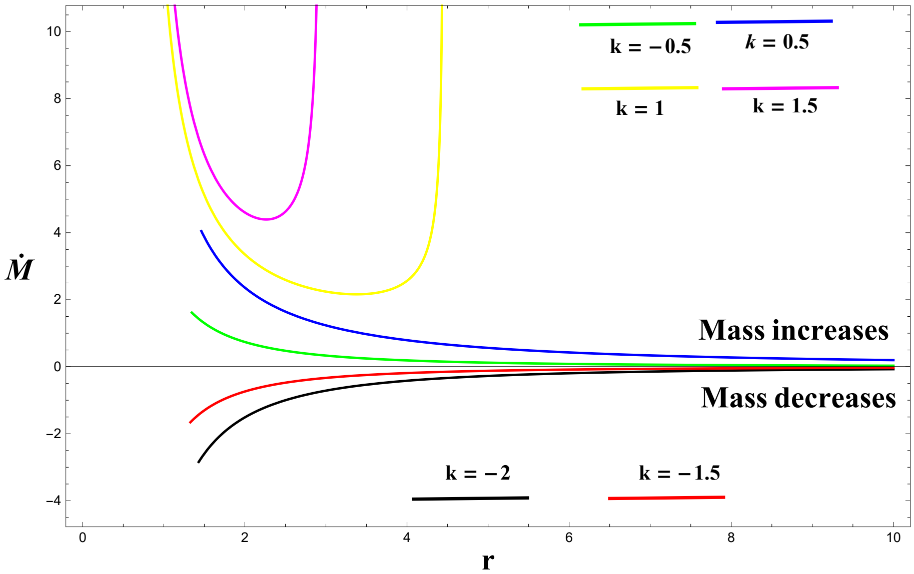

Figure 5.4: Rate of change of mass of BH as a consequences of accretion versus the radius r for $q = 1.055$ and $M = 2$, with different values of k. Upper half of the graph represents the mass increases while the lower half of the graph is for decrease in mass.

Bahamonde and Jamil (2015). The black and red curves suggest the negative velocity for phantom case with $k < -1$, whereas the upper half of the solution curves represent the positive velocity of quintessence, dust and stiff fluids. The energy density contour of the fluid in the locality of $4D$ EPM BH is plotted in Fig. **5.3**. The black and red curves show the energy density decreases for $k = -2$ and $k = -1.5$. The above portion of the graph indicates the energy density increases with different curves for $k = -0.5, 0, 0.5$ and 1. We have noted that if the fluid moves towards the BH, the energy density decreases in the phantom case while it increases in the other cases.

The rate of change of mass of EPM $4D$ BH is obtained from Eq. (2.94), which is given by

$$\dot{M} = \frac{4\pi L_0^2 M^2 (k+1)}{r^2 \sqrt{-\left(1 - \frac{\mu}{r} + \frac{q}{r^3}\right)(k+1)^2 + L_1^2}}. \tag{5.10}$$

In Fig. **5.4**, we have drawn the graph of the rate of change of mass of the BH ($\dot{M}$) versus radius r and it has been seen that the mass of the BH increases during the accretion process. Here, $k = -1$ is the case of cosmological constant, so equation of state $p = -\varrho$ can not be considered because accretion does not occur in this case.

Chapter 6

Michel Accretion onto a Non-Commutative and Hayward Black Holes

In this chapter, the matter accretion onto NC inspired Schwarzschild and regular Hayward BHs is addressed for a polytropic fluid and results are compared with Schwarzschild BH. The flow parameters - critical velocity $u(r)$, sonic speed c_s^2 and accretion rate $\dot{M}$ are derived from the considered BHs and are related to the outcomes acquired from the standard Schwarzschild BH. Due to the effect of noncommutative parameter θ, the mass accretion rate decreases with the increase of the strength of θ and vice versa. The same effect is seen for the sound speed and fluid velocity. The fluid velocity is positive as well as negative for the NC BH corresponding to Schwarzschild BH. The role performed by θ is significant in order to acquire the lager accretion rate for NC BH than the Schwarzschild BH.

It has been found that the accretion rate of regular Hayward BH differ from Schwarzschild BH. The graphical results depend on fluid radial velocity $u(r)$, speed of sound c_s^2 and the mass accretion rate $\dot{M}$. We have seen that the fluid radial velocity stay positive as well as negative. The speed of sound is decreased as we increase the value of parameter l of regular Hayward BH and also it is an increasing function of the radius r. The similar behavior is seen for the mass accretion rate. The results of this chapter have been published in the form of two research papers (Abbas and Ditta 2021; Ditta and Abbas 2020).

The layout of this chapter is as follows: In section **6.1**, we discuss the horizons structure of non-commutative BH. We have formulated the general results for the spherical accretion in section **6.1.1**. We have compared the accretion process regarding the Schwarzschild BH and NC BH in section **6.1.2**. Section **6.1.3** is devoted to the evaluation of critical points and graphical analysis of the results. Further, the horizons structure of regular Hayward BH has been presented in section **6.2**. The the evaluation of critical points and graphical analysis of the results in section **6.2.1**.

6.1 Review of Non-Commutative Black Hole

In this section, we have considered the static spherically symmetric and asymptotically flat Schwarzschild solution of the Einstein field equations with the matter energy density (2.17). We consider from (2.3), the analytical Schwarzschild solution can be retrieved in the limit $\frac{r}{\sqrt{\theta}} \to \infty$, further the limit $r \to \infty$, we can recover the Minkowski spacetime. The density function (2.17) contributes to the mass distribution $m(r) = \frac{2M}{\sqrt{\pi}}\gamma(3/2, r_H^2/4\theta)$, where M denotes the total mass of the system. The fluid density ϱ_θ depicts the following properties:

- Nearby the region i.e., $r << \sqrt{\theta}, \frac{d\varrho_\theta}{dr} \simeq 0 \to \varrho_\theta \simeq \text{constant} << \varrho_\theta(0)$.
- Some deviations from the origin that is $r >> 4\sqrt{\theta}, \frac{d\varrho_\theta}{dr} \simeq 0 \to \varrho_\theta \simeq constant << \varrho_\theta(0)$.
- Asymptotically far away that is $r >> 2M$, we have $\varrho_\theta = 0$.

For the event horizon, the lapse function must satisfy $A(r_H) = 0$, which simplifies to

$$r_H = \frac{2M}{\sqrt{\pi}}\gamma(3/2, r_H^2/4\theta). \tag{6.1}$$

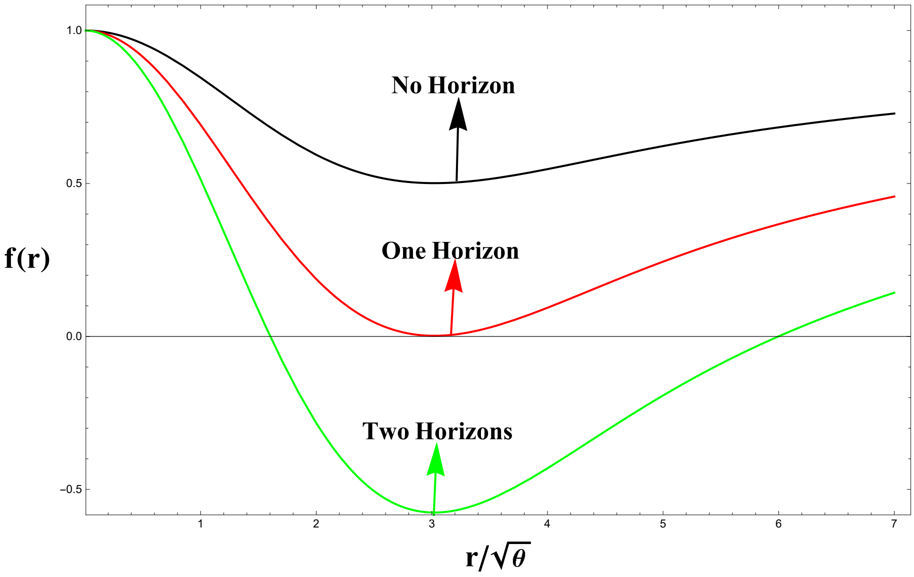

Figure 6.1: Plot shows the roots of $-g_{tt} = g_{rr}^{-1} = A(r)$ as a function of $r/\sqrt{\theta}$ for different values of $M/\sqrt{\theta}$. There are three solution curves such as black curve has no horizon for $M = 2.0\sqrt{\theta}$, red curve has one degenerate horizon for $M = 3.2\sqrt{\theta}$ at $r = 3\sqrt{\theta}$ and green curve has two horizons for $M = 6.0\sqrt{\theta}$.

In the presence of non-commutative parameter θ, Fig. **6.1** introduces the new behavior around the standard Schwarzschild BH. There are multiple horizons instead of single one. Figure **6.1**, has following properties

- It is found that the horizons can be degenerated by a critical mass M_0. The single horizon comes for $M = M_0 = 2\sqrt{\theta}$ with $r_H = 3\sqrt{\theta}$.
- Two horizons occur when $M > M_0$.
- There is no horizon for $M < M_0$.

It is noted that the effects of non-commutativity drop off exponentially and have comparable significances. The condition $r_H \leq 2M$ hold for non-zero value of non-commutative parameter θ, it means that the NC inspired BH horizon radius r_H is less than or equal to the conventional BH horizon radius $2M$. In view of these effects, there may be no BH when the original mass is smaller as compared to the minimal mass M_0. Incompatible to the regular case, there may be two horizons for extensive masses. The inner horizon drop off to zero whereas the outer horizon approaches to Schwarzschild value $r_H = 2M$ for $M >> M_0$.

6.2 Spherical Accretion

In this section, we have extend the relativistic accretion procedure of Michel (1972) to a NC inspired Schwarzschild BH. Now, we formulate the accretion equations for the NC BH and study how the non-commutative parameter θ affects the mass accretion rate $\dot{M}$. Here, we follow the Michel approach (1972), which we have already discussed in chapter **2**. From Eqs. (2.30) and (2.34), we obtain the expression of mass accretion rate of a BH, which is given by

$$\dot{M} = 4\pi N(\varrho_\infty + p_\infty). \tag{6.2}$$

However, the mass of BH decreases in phantom case. This is fairly interesting inference of Babichev et al (2004) that the mass of BH decreases as well as increases for $p+\varrho<0$ and $p+\varrho>0$, respectively.

The constants appearing in this section are significant in order to find the mass accretion rate and the fluid velocity with the help of equation of state. In section **6.4**, we will take one more EoS rather than $p=\omega\varrho$, which exclude non-physical sound speed and hydrodynamic instabilities in the presence of negative values of ω and ϱ.

6.3 Comparison Between the Schwarzschild Black Hole and Noncommutative Black Hole

Here, we have compared the radial velocity of the Schwarzschild metric and the the NC BH originated by the mass function inspired by the Gauss density function. In other words, we have to compare the fluid velocity in case of NC BH with the fluid velocity for the Schwarzschild BH. We get the mass function from Eq. (2.17), which is given by

$$m(r)=\frac{2M}{\sqrt{\pi}}\gamma(3/2,r_H^2/4\theta). \tag{6.3}$$

Assuming the EoS $k=\frac{p}{\varrho}=0$, the radial velocity of NC BH by using Eq. (6.3), which is given by

$$u_l=\sqrt{\frac{2M}{r\sqrt{\pi}}\gamma(3/2,r_H^2/4\theta)}. \tag{6.4}$$

In Schwarzschild BH, we obtain $u_{Sch}=\sqrt{\frac{2M}{r\sqrt{\pi}}}$, in the limit $r/\sqrt{\theta}\to\infty$. This indicates that fluid velocity of the NC BH is smaller than the Schwarzschild accretion velocity.

Considering the linear EoS $p=k\varrho$, and Eqs. (2.33) and (2.34), we get the following differential equation for fluid velocity

$$\frac{du}{dr} = -\frac{A'(r)}{2u}. \tag{6.5}$$

From $u_{Sch} = \sqrt{\frac{2M}{r\sqrt{\pi}}}$, we obtain $du_{Sch}/dr = M/r^2 u_{Sch}$ for the Schwarzschild BH. Now, for the NC BH, by using Eq. (6.3), we have the following result

$$\frac{du_l}{dr} = \frac{M}{u_l r^2} - \frac{1}{u_l 4\sqrt{\theta}} e^{-r^2/4\theta}. \tag{6.6}$$

Accordingly, the necessary conditions for the accretion process are $u < 0$ and $dr < 0$, du is positive for deceleration and is negative for acceleration. For the Schwarzschild BH, one has only a positive term of Eq. (6.5) through the accretion process. Consequently, for the NC BH, the second term in Eq. (6.6) yields a deceleration, it means that the second term is negative. Therefore, the anti-gravitational feature of the NC BH appears in this case.

6.4 Critical Points and Graphical Analysis

Here, we consider the following form of linear EOS

$$p = \omega(\varrho - \varrho_0), \tag{6.7}$$

where ϱ_0 is a constant. Babichev et al. (2004, 2011), have pointed out that above EoS removes the hydrodynamic instabilities due to $-\varrho$.

The useful relation between thermodynamics and dynamics variables is obtained from (2.30) and (6.7), in the following form

$$\left(\frac{p+\varrho}{p_\infty + \varrho_\infty}\right) = \left(-\frac{N}{ur^2}\right)^{1+\omega}. \tag{6.8}$$

Now for the radial velocity, we get the following simple expression from Eqs. (2.31) and (6.8),

$$A(r) + u^2 = \left(\frac{p+\varrho}{p_\infty + \varrho_\infty}\right)^{\frac{2\omega}{1+\omega}} = \left(-\frac{ur^2}{N}\right)^{2\omega}. \tag{6.9}$$

Figure **6.2** shows the radial velocity depends on ω. The larger ω, the critical point is very close to the event horizon. It means that the fluid sonic radial velocity is stretched nearby r_H. At that time, the fluid coming from infinity takes extra time to exceed c_s by larger values of ω. Using the EoS (6.7) and Eq. (2.30), the accretion rate constant N at the critical point is given by

$$N = r_c^2 \left(\frac{\omega^\omega}{\omega + A(r_c)} \right)^{\frac{1}{2\omega}} . \tag{6.10}$$

One can get the following general expression for accretion process by assuming the positivity of the accretion rate constant N for any value of state parameter ω,

$$N \simeq r_c^2 \left(\frac{\omega^\omega}{\omega + 1 - \frac{2M}{r_c\sqrt{\pi}}\gamma(3/2, r_c^2/4\theta)} \right)^{\frac{1}{2\omega}} . \tag{6.11}$$

The above Eq. (6.11) yield a larger accretion rate for NC BH than the Schwarzschild BH as we see in Fig **6.2**. For $\theta > 0$, the denominator of Eq. (6.11) may be smaller and then according to Eq. (6.2), mass rate of NC BH is larger than the Schwarzschild BH mass accretion rate. Similarly, the critical value of r_c for NC BH is larger than Schwarzschild BH case. Another interesting point is that the mass rate is larger for smaller θ.

Equation (6.9) yields an equation with critical points at $r = r_c$, so, one can obtain the critical points from Eqs. (6.9) and (6.10) by using the metric function $A(r)$. The value of ω at $r = r_c$ is given by

$$\omega = \frac{M}{2\sqrt{\pi} r_c} \left(\int_\theta^{\frac{r_c^2}{4\theta}} p^{\frac{1}{2}} e^{-p} dp - \frac{r_c^2}{2\sqrt{\theta}} e^{-\frac{r_c^2}{4\theta}} \right) . \tag{6.12}$$

Figure **6.2** shows the radial velocity of NC BH and Schwarzschild BH over the values of the parameter θ. The radial velocity of the Schwarzschild BH comes up at very small value of ($\theta = 0.0001$). Velocity graphic has two portions, the upper portion is for the positive velocity while the lower portion represents negative velocity. In the velocity graphic, the black curves represent the fluid velocity for the

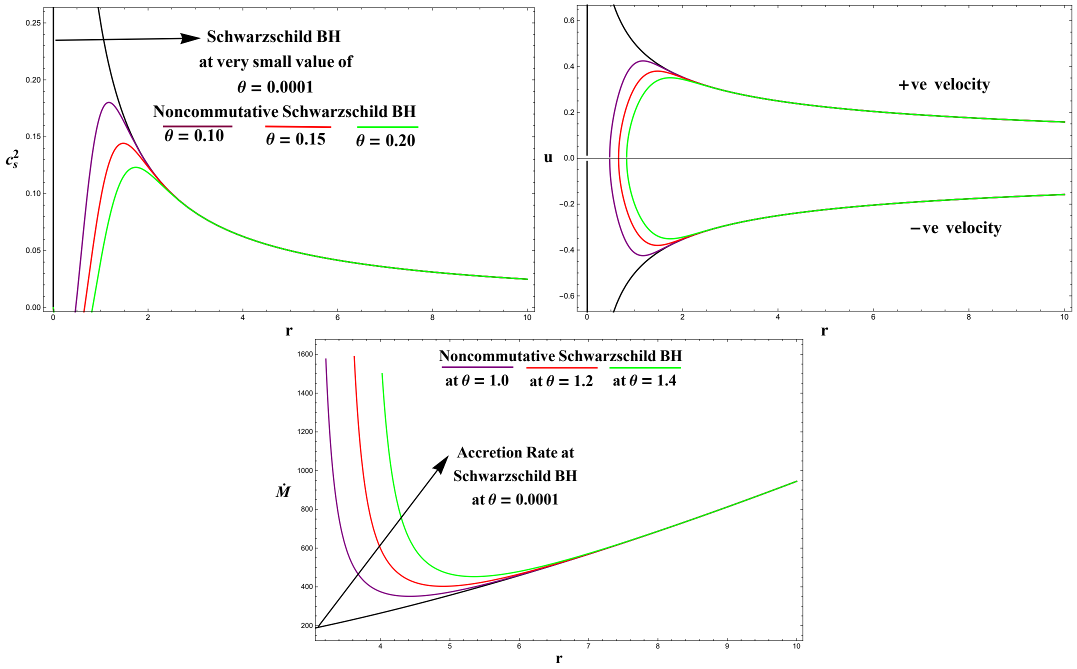

Figure 6.2: These plots show the accretion properties onto Hayward BH with parameters θ and ω in Eq. (6.12).

Schwarzschild case while purple, red and green curves depict the fluid velocity for the NC BH which is smaller than the Schwarzschild BH. It is stimulating to note that the behavior of fluid opposing the value of parameter θ, the larger the θ, the smaller the sound speed and hence the sonic point is larger.

The right graphic shows the radial velocity of NC BH and Schwarzschild BH over the values of the parameter θ. The radial velocity of the Schwarzschild BH comes up at very small value of $(\theta = 0.0001)$. Velocity graphic has two portions, the upper portion is for the positive velocity while the lower portion represents negative velocity. In the velocity graphic, the black curves represent the fluid velocity for the Schwarzschild case while purple, red and green curves depict the fluid velocity for the NC BH which is smaller than the Schwarzschild BH. It is stimulating to note that the behavior of fluid opposing the value of parameter θ, the larger the θ, the smaller the sound speed and hence the sonic point is larger.

In Figure **6.2**, we have observed that the speed of sound in NC BH increases and the critical radius decreases towards the singularity for the decreasing values of the non-commutative parameter θ (see left graph). We note that the speed of sound for NC BH is smaller as compare to the Schwarzschild BH. So, following three critical values are observed for the NC BH

- $c_s^2 \approx 0.12$, $r_c \approx 0.932$ corresponding to $\theta = 0.20$.
- $c_s^2 \approx 0.14$, $r_c \approx 0.732$ corresponding to $\theta = 0.15$.
- $c_s^2 \approx 0.175$, $r_c \approx 0.532$ corresponding to $\theta = 0.10$.

We have observed that the fluid velocity in NC BH increases and the critical radius decreases towards the singularity for the decreasing values of the non-commutative parameter θ (see right graph). We note that the fluid velocity for NC BH is smaller than the Schwarzschild BH.

It is noted that the mass accretion rate of NC BH increases and the critical radius decreases towards the singularity for the decreasing values of the noncommutative parameter θ in Fig. **6.2** (see bottom graph). Further, the mass accretion rate for NC BH is larger as compare to the Schwarzschild BH. So, there are following three critical values for the NC BH:

- $\dot{M} \approx 15000$, $r_c \approx 4.5$ corresponding to $\theta = 1.40$.
- $\dot{M} \approx 15900$, $r_c \approx 3.5$ corresponding to $\theta = 1.20$.
- $\dot{M} \approx 16000$, $r_c \approx 2.5$ corresponding to $\theta = 1.00$.

From the above discussion, difference in accretion rate constant N is due to the variation in θ. For the NC geometry, the critical points are larger distance as compared to standard Schwarzschild BH. However, the accretion rate is larger in NC geometry than the standard Schwarzschild BH but the radial velocity and speed of sound are smaller as compared to standard Schwarzschild BH. On physical background Michel approach (1972) contributes to non-physical and physical solutions but we have studied the physical solutions that is the real accretion process in which the perfect fluid go away from infinity to rest while its velocity monotonically increases in the extremal horizon. For such solutions, fluid exerts the subsonic accretion far from the event horizon and then passes through the sonic point. At point $r = r_c$, fluid radial velocity becomes equal to the sound speed. On the other hand, after that point, the fluid radial velocity increased to the supersonic accretion during the inflow motion of particles. So, we have a sonic sphere centered at sonic point surrounded by spherically symmetric spacetime. The fluid radial velocity always equal to the speed of sound at the sonic sphere.

6.5 Horizons of Hayward Regular Black Hole

In the aforementioned Michel procedure, we analyze the accretion process near a Hayward regular BH. The Hayward BH is given by the following metric coefficient

$$A(r) = 1 - \frac{2mr^2}{r^3 + 2l^2m}, \tag{6.13}$$

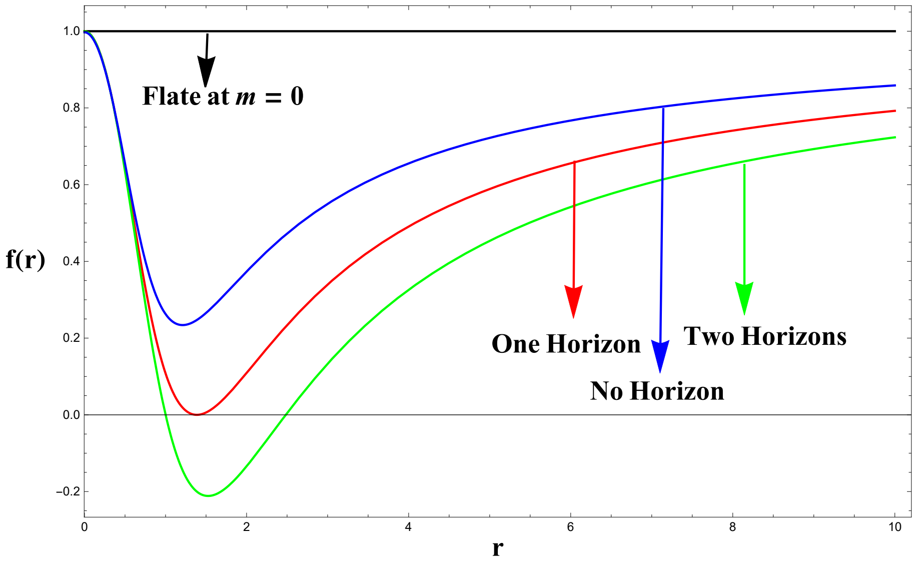

Figure 6.3: Horizons behavior of Hayward BH with different values of m and fixed value of l.

in this BH, m denotes mass and l represents a convenient encoding positive energy density. For asymptotic behavior of the lapse function $A(r)$ i.e. $\lim r \to \infty$ moderates to $1 - \frac{2m}{r} + 0(\frac{1}{r^4})$ while at $\lim r \to \infty$ moderates to $1 - \frac{r^2}{l^2} + 0(r^4)$. We can see clearly that at large value of r the Hayward BH develops the Schwarzschild BH while at small value of r, it becomes de-Sitter BH. Now it is important to see that the lapse function $A(r)$ develops Schwarzschild BH at $l = 0$ and it is flat for $m = 0$. The graphical behavior of Hayward BH is given in Fig. **6.3**.

It is noted that the metric parameters l and m of the lapse function $A(r)$ play the significant role, as it reduces to the Schwarzschild BH at $l = 0$ and is flat for $m = 0$, it is shown in black solution curve in Fig. **6.3**. Also, lapse function $1 - \frac{2mr^2}{r^3+2l^2m}$, provides different horizons for the variations of m and fixed value of $l = 0.80$, which can be seen in blue, red and green solution curves respectively in the Fig. **6.3**. The horizons structure can be explained as follows

- No horizon for $m = (\frac{3\sqrt{3}}{4})l$ at $r > 0$.

- One horizon for $m < (\frac{3\sqrt{3}}{4})l$ at critical radius $r = r_c$.

- Two horizons for $m > (\frac{3\sqrt{3}}{4})l$ at $r = r_{\pm}$.

6.5.1 Critical Points and Graphical Analysis

The general results for this section have been formulated in the previous section, therefore the value of ω at $r = r_c$ for Hayward BH is given by

$$\omega = \frac{mr_c^2}{2}\left(\frac{-4l^2m + r_c^3}{(2l^2m + r_c^3)^2}\right). \tag{6.14}$$

Alternatively, critical points of Eq. (6.14) can be determined by using Eqs. (2.39) and (2.40). There exist two critical points, namely the inner r_{c-} and outer r_{c+}, these are shown in Fig. **6.4**. The physically critical points must satisfy the following relation

$$r_{c+} > r_+ > r_{c-} > r_- > 0. \tag{6.15}$$

Also, these points have following significance

- Out of two critical solutions only one corresponds to the Schwarzschild BH that is $r_{c+} = m/2\omega$.

- In Fig. **2**, the BHs present the maximum ω at $1/3$.

- The impact of parameter l is significant for the critical solution.

The plots in Fig. **6.4** provide the following comments:

1. On the top graphic, Eq. (6.14) in order to equality $c_s^2 = \omega$ gives the speed of sound versus the values of critical point r_c. As we can see the red dot on the top solution curve at $l = 0.10$ shows the maximum speed of sound outside the event horizon.

2. On the middle, plot shows the radial velocity over some values of the parameter l and for the Schwarzschild BH ($l = 0$). The important point is that the graphic

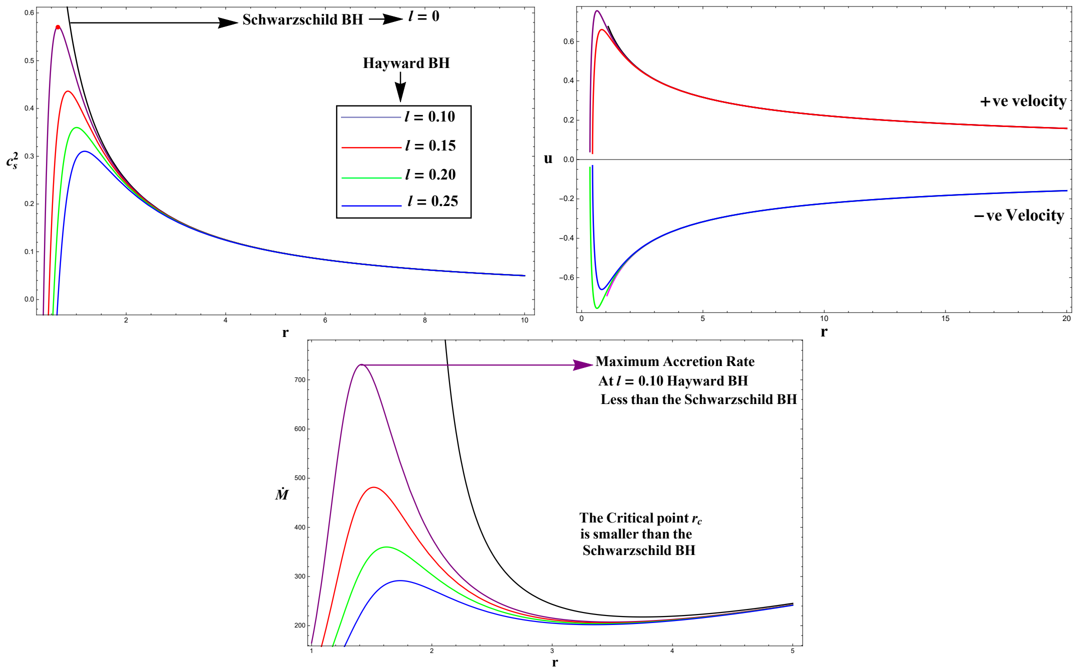

Figure 6.4: These plots show the accretion properties onto Hayward BH with parameters l and ω in Eq. (6.14).

shows two portions, the upper portion represents the positive velocity while the lower portion is for negative velocity. The larger l, the smaller speed of sound and consequently the critical point is larger. It means that in the accretion process, for small value of l fluid's required the long distance in order to reach the speed of sound c_s.

3. The bottom graphic depicts the accretion rate behavior with the help of Eq. (6.14). The black solution curve indicates the Schwarzschild BH accretion rate which is larger than the Hayward BH solution curves (magenta, red, green and blue). Throughout the graphics, we consider $m = 1$ and different values of l.

Chapter 7

Summary and Discussion

This chapter provides the summary and discussion of the results found in the thesis. The main theme of the thesis is to investigate the relativistic accretion onto a conformal gravity BH, regular phantom BH, NC BH and Hayward BH. For these BHs, we have analyzed how the mass of BHs gradually changes for different kind of fluid.

In chapter **THREE**, we have investigated the spherically symmetric accretion around the conformal gravity BH, with four kinds of fluid such as ultra-stiff fluid, ultra-relativistic fluid, radiation-fluid and sub-relativistic fluid by using the Hamiltonian approach. It is demonstrated that the energy density is always equal to pressure in ultra-stiff fluids. In this case, it has been observed that supersonic as well as subsonic accretion flow would exist for the particular values of the parameters. The critical radius in Schwarzschild BH is larger than the conformal gravity BH and Schwarzschild de-Sitter BH. The energy density is double of the pressure for ultra-relativistic fluid and there exists a supersonic flow, which is followed by subsonic flow. The fluid flow around Schwarzschild BH for ultra-relativistic fluid is entirely different as compared to conformal gravity BH and Schwarzschild de-Sitter BH. The $3D$-speed v is very small but the radial distance is larger for Schwarzschild BH than the conformal gravity BH and Schwarzschild de-Sitter BH. It is also noted that the critical radius is very close to the horizon of Schwarzschild BH than the conformal gravity BH and Schwarzschild de-Sitter BH in ultra relativistic fluid. The nature of radiation-fluid and sub-relativistic fluid (in which the energy density is greater than the pressure) is similar for $v > v_c$. A very simple behavior has been observed for the radiation-fluid that is only supersonic flow exists for Schwarzschild BH while subsonic accretion exists for conformal gravity BH and Schwarzschild de-Sitter BH. Further, for sub-relativistic fluid, the flow around Schwarzschild BH is absolutely closer to ultra-relativistic fluid that is the critical radius is closer to the horizon as compared to conformal gravity BH and Schwarzschild de-Sitter BH. The $3D$ speed for radial motion is very small in Schwarzschild BH than the conformal gravity BH and Schwarzschild de-Sitter BH.

Chapter **FOUR** provides the accretion process of a test particle in a geodesic motion onto a regular phantom BH in an equatorial plane. For this, we have investigated the circular geodesics and their stabilities and oscillations near the stroke of small perturbations. We have also presented the characteristic radii, effective potential, energy flux, angular momentum, epicyclic frequencies, dynamical parameters, emission rate and the mass evolution of the BH in details. Then we have done some discussions for the general solutions of the regular phantom BH by adopting an isothermal fluid with EoS $p = k\rho$.

The results of our analysis shows that the phantom parameter b affects each case of the considerations such as, the effective potential for the unstable and stable circular orbits. The behavior of V_{eff} shows that the curves black to blue gradually increases for larger values of the parameter b and this behavior shows that the unstable orbits at smaller radii but a stable circular orbits at some distance from central mass. For this BH the circular orbits such as r_{sing}, r_{ph}, r_{mb} and r_{isco} are decreasing functions of phantom parameter b. The circular orbits shifts from r_{sing} to r_{isco} for more values of b and finally particles would fall onto BH.

Energy diagram shows that the phantom parameter b increases, the energy increases while decreases the angular momentum, and for large deviations the range of orbits will be smaller. The efficiency of an accretion decreases as b increases. The radiation energy flux is maximum in the locality of BH and decreases in the smaller radii. As the phantom parameter b increases the flux gradually increases and its maximum position turns to the smaller radii. One can see the same behaviors for temperature. Further, the physical behavior of epicyclic frequencies shows that the vertical epicyclic frequency has no extrema and it is a monotonically decreasing function of r but the radial frequency has a maxima always and the effect of phantom parameter b on it is considerable. We have investigated the behavior of epicyclic frequencies, it is clear that $\Omega_r < \Omega_\theta$ and the ratio $\frac{\Omega_\theta}{\Omega_r}$ is decreasing function of r.

Chapter **FIVE** deals with the accretion onto a regular phantom BH and Einstein-power-Maxwell $4D$ BH by adopting the Michel approach (1972). The critical velocities and the speed of sound are obtained for the fluid flow around the considered BHs. We have the EoS to see the behavior of the fluid velocity $u(r)$, energy density $\rho(r)$ and mass accretion rate $\dot{M}$. These quantities have been explored for the fixed values of parameters as $M = 2, \mu = 2, b = 1.055, q = 1.055$ and with various values of state parameter k for regular phantom and Einstein-power-Maxwell $4D$ BHs. If we assume $\mu = 1$ and distinct values of the charge parameter q for Einstein-power-Maxwell $4D$ BH, then there is non-physical behavior of matter variables with some values of k. In this analysis, the phantom parameter b and charge parameter q are fixed for the radial velocity and the density profile for $k > -1, k < -1, k = 0$ and $k = 1$. The radial velocity and the density profile are positive and negative depending on the metric and equation of state parameter. If the energy density becomes negative, it violates the energy conditions. However, in absolute value, the fluid energy density increases for all these cases.

In chapter **SIX**, we have investigated the accretion of fluids onto NC and Hayward regular BHs. We have adopted Michel approach (1972) for steady-state accretion onto NC and Hayward regular BHs and compared the results of both BHs to the Schwarzschild BH. The sound speed at the critical radius increases by decreasing the noncommutative parameter θ. The fluid velocity increases vertically by decreasing the value of noncommutative parameter θ. The mass accretion rate near the NC Schwarzschild BH is modified due to noncommutative parameter θ. Further, it is found that the mass accretion rate increases with decreasing the values of θ. The radial velocity and speed of sound are smaller for NC BH as compared to Schwarzschild BH. The accretion rate of NC BH is larger than the rate of Schwarzschild BH. For the regular Hayward BH, it has been observed that a parameter l plays a central role for modifying the speed of sound, radial velocity and accretion rate of BHs. For $l = 0.10, 0.15, 0.20, 0.25$, the sound speed, radial velocity and accretion rate gradually decrease. Also one can see the converse of this, that is to say decrease in the values of l results in the increase of the sound speed, radial velocity and mass accretion rate. The radial velocity is positive as well as negative for the regular Hayward BH and accretion flow is slower as compared to the Schwarzschild BH. It has been found that the critical points for the regular Hayward BH are closer to central singularity than the Schwarzschild BH.

Bibliography

Abbas, G. and Ditta, A. (2021) Michel accretion onto a non-commutative black hole. *New Astonomy* 84:101508.

Abbas, G., Azam, M. and Ditta, A. (2021) Accretion onto a Born-Infeld black hole. *Chinese Journal of Physics* 69:143-152.

Abbas, G. and Ditta, A. (2020) Matter Accretion onto a Conformal Gravity black hole. *Eur. Phys. J. C* 80:1212.

Abbas, G., Ditta, A., Jawad, A. and Umair, S. (2019) Matter accretion onto a brane-world black hole via Hamiltonian approach. *Gen. Relat. Gravit.* 51:136-155.

Abbas, G. and Ditta, A. (2019) Matter accretion onto Einstein-power-Maxwell black hole. *Gen. Relat. Gravit.* 51:43.

Abbas, G. and Ditta, A. (2018) Accretion onto a charged Kiselev black hole. *Mod. Phys. Lett. A* 33:1850070-9.

Abbas, G. and Sabiullah, U. (2014) Geodesic study of regular Hayward black hole. *Astrophys Space Sci.* 352(2):769-774.

Ahmad, A. K. Azreg-Ainou, M. Bahamonde, S. Capozziello, S and Jamil, M. (2016) Astrophysical flows near f (T) gravity black holes. *Eur. Phys. J. C* 76:269.

Ahmad, A. K., Azreg-Ainou, M., Bahamonde, S., Capozziello, S. and Jamil, M. (2016) Cyclic and heteroclinic flows near general static spherically symmetric black holes. *Eur. Phys. J. C* 76:280.

Ainou, A. M. et al. (2011) Phantom black holes and sigma models. *Phys. Rev.*

D 83:124001.

Akiyama, K. et al. (2019) The Event Horizon Telescope Collaboration. *Astrophys J. Lett.* 875:L1.

Anastasiou, G. and Olea, R. (2016) From conformal to Einstein gravity. *Phys. Rev. D* 94:086008.

Ayn-Beato, E. and Garca, A. (2000) The Bardeen model as a nonlinear magnetic monopole. *Phys. Lett. B* 493:149152.

Azreg-Anou, M.(2013) Light paths of normal and phantom Einstein-Maxwell-dilaton black holes. *Phys. Rev. D* 87:024012.

Babichev E, Dokuchaev V, Eroshenko Y. (2004) Black Hole Mass Decreasing due to Phantom Energy Accretion. *Phys. Rev. Lett.* 93:021102-4.

Babichev, E. Charmousis, C. and Lehbel, A. (2016) Black holes and stars in Horndeski theory. *Class. Quant. Gravity* 33:154002.

Babichev, E., Dokuchaev, V. and Eroshenko, Y. (2005) The accretion of dark energy onto a black hole. *Exp. Theor. Phys.* 100:528-538.

Begelman, M. C. (1978) Accretiopn of $v > 5/3$ gas by a Schwarzschild black hole. *Astron. Astrophys.* 70:583-584.

Bahamonde, S. and Jamil, M. (2015) Accretion processes for general spherically symmetric compact objects, *Eur. Phys. J. C* 75:508.

Bambi, C., Modesto, L., Porey, S. and Rachwal, L. (2018) *Eur. Phys. J. C* 78:116.

Banerjee, R., Majhi, B. R., and Modak, S. K. (2009) Noncommutative Schwarzschild black hole and area law *Class. Quant. Gravity* 26:085010.

Bardeen, J. (1968) Proceedings of GR5. *Tiis, U.S.S.R.*.

Biswas, R., Chakraborty, S., Saini, T. D. and Mukhopadhyay, B. (2011) Accretion of Chaplygin gas upon black holes formation of faster outflowing winds. *Class. Quant. Gravity* 28:035005.

Blakeslee, J. P. et al. (2003) Discovery of two distant type Ia supernovae in the hubble deep fieldnorth with the advanced camera for surveys. *Astrophys. J.*

589:693-703.

Bolokhov, S. V., Bronnikov, K. A. and Skvortsova, M. V. (2012) *Class. Quant. Gravity* 29:245006.

Bondi, H. and Hoyle, F. (1944) On the mechanism of accretion by stars. *Mon. Not. R. Astron. Soc.* 104:273-282.

Bondi, H. (1952) On Spherically Symmetrical Accretion. *Mon. Not. R. Astron. Soc.* 112:195-204

Bronnikov, K. A. and Fabris, J. C. (2006) Regular Phantom Black Holes. *Phys. Rev. Lett.* 96:251101.

Bronnikov, K. A. Dehnen, H. and Melnikov, V. N. (2007) Regular black holes and black universes. *Gen. Relat. Gravit.* 39:973.

Carroll, S. M., Hoffman, M. and Trodden, M. (2003) Can the dark energy equation-of-state parameter w be less than -1? *Phy. Rev. D* 68:023509.

Chakrabarty, H., Benavides-Gallego, C. A., Bambi, C. and Modesto, L. (2018) Unattainable extended spacetime regions in conformal gravity *JHEP.* 1803:013.

Chakrabarty, S. K. (2011) Fundamental concepts in transonic flow paradigm of black hole astrophysics. *Int. J. Mod. Phys. D* 20:1723.

Chakrabarty, S. K. (1990) Theory of transonic astrophysical flows. *World Scientific.*

Chaverra, E. and Sarbach, O. (2015) Radial accretion flows on static spherically symmetric black holes. *Class. Quantum Gravity* 32:155006.

Clement, G., Fabris, J. C. and Rodrigues, M. E.(2009) Phantom black holes in Einstein-Maxwell-dilaton theory. *Phy. Rev. D* 79:064021.

Connes A. (1994) Non-commutative Geometry. *Academic Press New York.*

Ditta, A. and Abbas, G. (2020) Circular orbits and accretion process near a regular phantom black holes. *Gen. Relat. Gravit.* 52:77.

Ditta, A. and Abbas, G. (2020) Relativistic accretion mechanism for some black holes. *Chinese Journal of Physics* 65:325-333.

Ditta, A. and Abbas, G. (2020) Astrophysical accretion near Hayward regular black holes. *New Astronomy* 81:101437.

Debnath, U. (2015) Accretion and evaporation of modified Hayward black hole. *Eur. Phys. J. C* 75:129.

Dunkley, J. et al.(2009) Five-Year Wilkinson microwave anisotropy probe observations: likelihoods and parameters from the WMAP Data. *Astrophys. J. Suppl.* 180:306-329.

Einstein, A. (1915) Fundamental Ideas of the General Theory of Relativity and the Application of this Theory in Astronomy. *Preussische Akademie der Wissenschaften, Sitzungsberichte* 1915:315.

Eisenstein, D. J. et al. (2002) Detection of the Baryon Acoustic Peak in the Large-Scale Correlation Function of SDSS Luminous Red Galaxies. *Astrophys. J.* 633:560.

Eiroa, E. F. and Sendra, C. M. (2013) Regular phantom black hole gravitational lensing. *Phy. Rev. D* 88:103007.

Fan, Z. Y. and Wang, X. (2016) Construction of regular black holes in General Relativity. *Phy. Rev. D* 94:124027.

Ficek, F. (2015) Bondi-type accretion in the ReissnerNordstrm(anti-)de Sitter spacetime. *Class. Quant. Gravity* 32:235008.

Flachi, A. and Lemos, J. P. S. (2013) Quasinormal modes of regular black holes. *Phy. Rev. D* 87:024034.

Ganguly, A., Ghosh, S. G. and Maharaj, S. D. (2014) Accretion onto a black hole in a string cloud background. *Phy. Rev. D* 90:064037-9.

Gao, C. J. and Zhang, S. N. (2006) Phantom black holes. *INSPIRE.* hep-th/0604114.

Gibbons, G. W. and Rasheed, D. A. (1996) Dyson pairs and zero mass black holes. *Nucl. Phys. B* 476:515-547.

Grigoris, P. (2019) Charged scalar fields around Einstein-power-Maxwell black holes. *Gen. Relativ. Gravit.* 51:76.

Gurtug, O., Mazharimousavi, S.H., Halilsoy, M. (2012) $2+1$ dimensional electrically charged black holes in Einstein-power-Maxwell theory. *Phy. Rev. D* 85:104004.

Halilsoy, M., Ovgun, A. and Mazharimousavi, S. H. (2014) Thin-shell wormholes from the regular Hayward black hole. *Eur. Phys. J. C* 74:2796.

Hawking, S. W. (1972) Black holes in general relativity. *Communications in Mathematical Physics* 25:152-166.

Haydarov, K., Abdujabbarov, A., Rayimbaev, J. and Ahmedov, B. (2020) Magnetized particle motion around black holes in conformal gravity: can magnetic interaction mimic spin of black holes? Universe 6:10.3390/universe 6030044.

Hannestad, S.(2006) Dark energy and dark matter from cosmology observations. *Int. J. Mod. Phys. A* 21:1938-1949.

Harko, T. and Mak, K. M. (2005) Conformally symmetric vacuum solutions of the gravitational field equations in the brane-world models *Annals of Physics* 319:471-492.

Harko, T. and Mak, K. M. (2004) Vacuum solutions of the gravitational field equations in the brane world model. *Phys. Rev.* 636:8.

Hassaine, M., Martinez, C. (2008) Higher-dimensional charged black hole solutions with a nonlinear electrodynamics source. *Class. Quantum Gravity* 25:195023.

Hayward, S. A. (2006) Formation and evaporation of nonsingular black holes. *Phys. Rev. Lett.* 96:031103.

Horava, P. (2009) Quantum gravity at a Lifshitz point. *Phy. Rev. D* 79:084008.

Hoyle, F. and Lyttelton, R. A. (1939) The effect of interstellar matter on climatic variation. *Proc. Camb. Philos. Soc.* 35:405-415.

Huang, Y., Chen, S. and Jing, J. (2016) Double shadow of a regular phantom black hole as photons couple to the Weyl tensor. *Eur. Phys. J. C* 76:594.

Johri, V. B. (2004) Phantom cosmologies. *Phys. Rev. D* 70:041303.

Jamil, M., Rashid, M. A. and Qadir, A. (2008) Charged black holes in phantom cosmology. *Eur. Phys. J. C* 58:325.

Jamil, M. (2009) Themodynamics Of a Schwarzschild black hole in phantom cosmology with entropy corrections. *Eur. Phys. J. C* 62:609.

Jawad, A. and Umair, S. (2017) Accreting fluids onto regular black holes via Hamiltonian approach. *Eur. Phys. J. C* 77:515.

John, A. J., Ghosh, S. G. and Maharaj, S. D. (2013) Accretion onto a higher dimensional black hole. *Phys. Rev. D* 88:104005-7.

Jiao, L. and Yang, R. (2017) Accretion onto a Kiselev black hole. *Eur. Phys. J. C* 77:356.

Komatsu, E. et al. (2011) Seven-year Wilkinson microwave anisotropy probe (WMAP) observations: cosmological interpretation. *Astrophys. J. Suppl.* 192:18.

Karkowski, J. et al. (2006) Universality and backreaction in a general-relativistic accretion of steady fluids. *Phys. Rev. D* 73:021503.

Karkowski, J. et al. (2013) Bondi accretion onto cosmological black holes. *Phys. Rev. D* 87:044007.

Kiselev, V. V. (2003) Quintessence and black holes. *Class. Quant. Gravity* 20:1187-1198.

Kato, et. al. (2008) Black Hole Accretion Disks. *Towards a New Paradigm Kyoto University Press, Kyoto* 550.

Lobo, F. S. N. (2005) Phantom energy traversable wormholes. *Phys. Rev. D* 71:084011.

Lu, H., Pang, Y., Pope, C. N. and Vazquez-Poritz, J. F. (2012) AdS and Lifshitz black holes in conformal and Einstein-Weyl gravities. *Phys. Rev. D* 86:044011.

Mannheim, P. D. (2012) Making the case for conformal gravity. *Foundations of Physics* 42:388-420.

Mannheim, P. D. (2011) Comprehensive solution to the cosmological constant, zero-point energy, and quantum gravity problems. *Gen. Relativ. Gravit.* 43:703.

Mannheim, P. D. and Kazanas, D. (1989) Exact vacuum solution to conformal Weyl gravity and galactic rotation curves. *Astrophys. J.* 342:635.

Mannheim, P. D. and Kazanas, D. (1991) Solutions to the Reissner-Nordstrm, Kerr, and Kerr-Newman problems in fourth-order conformal Weyl gravity. *Phys. Rev. D* 44:417.

Martnez-Pas, I. G., Shahbaz, T., and Velzquez, J. C. (2014) Accretion Processes in Astrophysics. *Cambridge University Press Cambridge* 18.

Mach, P., Malec, E. and Karkowski, J. (2013) Spherical steady accretion flows: Dependence on the cosmological constant, exact isothermal solutions, and applications to cosmology. *Phy. Rev. D* 88:084056.

Michel, C. F. (1972) Accretion of matter by condensed objects. *Astrophys. Space Sci.* 15:153-160.

Nagle, R. K., Saff, E. B. and Snider, A. D. (2012) Fundamentals of differential equations and boundary value problems. *Pearson, International Edition 6th edn. UK.* 888.

Nicoloni, P., Smailagic, A. and Spallucci, E. (2006) Noncommutative geometry inspired Schwarzschild black hole. *Phys. Lett. B* 632:547-551.

Nojiri, S. and Odintsov, S. (2011) Unified cosmic history in modified gravity from F(R) theory to Lorentz non-invariant models. *Phys. Rep.* 505:59-144.

Novikov, I. and Thorne, K. S. (1973) In Black Holes. *Gordon and Breach, New York* 343.

Pandey, S. U. (1987) Accretion of charged matter by collapsing objects. *Astrophys. Space Sci.* 136:195-199.

Perlmutter, S. et al. (1999) Measurements of Omega and Lambda from 42

High-Redshift Supernovae. *Astrophys. J.* 517:565.

Perlmutter, S. et al. (1999) Supernova Cosmology Project Collaboration. *Astrophys. J.* 517:565.

Rezzolla, L., Zanotti, O. (2013) Relativistic Hydrodynamics. *Oxford University Press, London* 735.

Riess, A. G. et al. (1998) Observational Evidence from Supernovae for an Accelerating Universe and a Cosmological Constant. *Astron. J.* 116:1009.

Rodrigues, M. E. and Oporto, Z. A. A.(2012) Thermodynamics of phantom black holes in Einstein-Maxwell-dilaton theory. *Phy. Rev. D* 85:104022.

Salahshoor, K. and Nozari, K. (2018) Circular orbits and an accretion disks in a class of Horndeski/Galileon black holes. *Eur. Phys. J. C* 78:486.

Snyder, H. S. (1947) Quantized Space-Time. *Phys. Rev.* 71:38.

Sharif, M. and Iftikhar, S. (2016) Accretion onto a charged higher-dimensional black hole. *Eur. Phys. J. C* 76:147.

Sharif, M. and Iftikhar, S. (2016) Dynamics of particles near black hole with higher dimensions. *Eur. Phys. J. C* 76:404.

Sharif, M. and Iftikhar, S. (2016) Shadow of a charged rotating non-commutative black hole. *Eur. Phys. J. C* 76:630.

Sharif, M. and Abbas, G. (2011) Phantom accretion by five-dimensional charged black hole. *Mod. Phys. Lett. A* 26:1731.

Sharif, M. and Abbas, G. (2012) Phantom energy accretion by a string charged black hole. *Chin. Phys. Lett.* 29:010401.

Sharif, M. and Shahzadi, M. (2017) Particle dynamics near Kerr-MOG black hole. *Eur. Phys. J. C* 77:363.

Sharif, M. and Mumtaz, S. (2017) Stability analysis of an oscillating cylinder. *Not. R. Astro. Soc.* 471:1215.

Singh, P., Sami, M. and Dadhich, N. (2003) Cosmological dynamics of a phantom field. *Phys. Rev. D* 68:023522.

Smailagic A, Spallucci J. (2003) Feynman Path Integral on the Noncommutative Plane. *J. Phys. A* 43:467-471.

Smailagic A, Spallucci J. (2003) UV divergence-free QFT on noncommutative plane. *J. Phys. A* 43:517-521.

Spergel, et al. (2007) Three-Year Wilkinson microwave anisotropy probe (WMAP) observations: implications for cosmology WMAP collaboration. *Astrophys. J. Suppl.* 170:337.

Stelle, K. S. (1977) Renormalization of higher-derivative quantum gravity. *Phys. Rev. D* 16:953.

Thorne, K. S., Flammang, R. A. and Zytkow, A. N. (1981) Stationary spherical accretion into black holes-1. Equation of structure. *Mon. Not. R. Acad. Sci.*194:475-484.

Toshmatov, B., Ahmedov, B., Abdujabbarov, A. and Stuchilk, Z. (2014) Rotating regular black hole solution. *Phys. Rev. D* 89:104017.

Toshmatov, B., Bambi, C. Ahmedov, B., Abdujabbarov, A. and Stuchilk, Z. (2017) Energy conditions of non-singular black hole spacetimes in conformal gravity. *Eur. Phys. J. C* 77:542.

Turimov, B., Ahmedov, B., Abdujabbarov, A. and Bambi, C. (2018) Electromagnetic fields of slowly rotating magnetized compact stars in conformal gravity. *Phys. Rev. D* 97:124005.

Will, C. M. (2014) The confrontation between General Relativity and experiment. *Living Rev. Rel.* 17:4.

Xu, W. and Zhao, L. (2014) Maxwells equal area law for Lovelock Thermodynamics. *Phys. Lett. B* 736:214.

Xu, H., Sun, Y. and Zhao, L. (2017) Black hole thermodynamics and heat engines in conformal gravity. *Int. J. Mod. Phys. D* 13:1750151.

Xu, H. and Yung, M. H. (2018) Black hole evaporation in conformal (Weyl) gravity. *Phys. Lett. B* 783:36.

Zhou, M. et al. (2018) Testing conformal gravity with the supermassive black hole in 1H0707-495. *Phys. Rev. D* 98:024007.

Zhang, R. and Jing, J. (2018) Strong gravitational lensing for photons coupled to Weyl tensor in a regular phantom black hole. *Eur. Phys. J. C* 78:796.

Zhang, Q., Modesto, L. and Bambi, C. (2018) A general study of regular and singular black hole solutions in Einsteins conformal gravity. *Eur. Phys. J. C* 78:506.